MASTER'S THESIS

Study of Gas Mixture for Glass RPC at BELLE Experiment

Makoto Ueki

Department of Physics, Tohoku University

February 1999

Abstract

The BELLE experiment will start its first physics program aiming at detailed studies on CP violation in April 1999. The BELLE detector together with the accelerator KEKB is now on commissioning and getting ready for the first physics program.

The KLM detector which is a subdetector of the BELLE detector is designed to detect K_L^0 mesons and muons. RPCs with glass electrodes are employed for the KLM. The RPC is a gaseous detector and it is better to use nonflammable gas mixture for safety. It is also better to use environmentally safe gas mixture. From this point of view, the use of Freon(HFC134a) which we have been using is not desirable for having a high global warming potential. Then we have performed a study of nonflammable and freonless gas mixture for the glass RPCs.

To make the gas nonflammable means to reduce the fraction of butane which is expected to prevent the secondary discharges by absorbing ultraviolet photons. We have tested RPCs with nonflammable gas mixtures and compared their performance with that with flammable ones. We verified that the effect of the secondary discharges due to decreasing the butane ratio was not so serious and a nonflammable gas mixture was useful enough.

For freonless gas studies, by using SF_6, we could operate RPCs at much lower high voltage (HV) with comparable performance to the HFC134a gas mixture. However, the RPC performance with the SF_6 gas mixture was characterized by its narrow plateau range showing operation instability. The feasibility to use the SF_6 gas mixture as the gas for the BELLE KLM detector is discussed.

Acknowledgments

First, I would like to thank Prof. A.Yamaguchi for introducing me to the BELLE experiment and for his guidance as my thesis advisor.

I would like to thank Prof. K.Abe for his useful suggestions about the analyses. I would like to thank Dr. T.Nagamine for his valuable advice. I would like to thank Dr. S.Narita for the helpful discussions. I would like to thank the technicians, T.Takayama, H.Hanada, T.Nakajima, M.Nakajima and K.Tamae for their reliable technical support and for their kindness.

I also would like to thank the BELLE endcap KLM group, Prof. K.Abe of KEK, Prof. H.Yuta and Prof. N.Kawamura of Aomori University, Prof. Y.Hoshi, Dr. K.Neichi and F.Haitani of Tohoku-Gakuin University, Prof. Y.Teramoto, Dr. E.Nakano and H.Sakai of Osaka City University, M.Yamaga, S.Azuchi, Y.Igarashi, F.Handa, N.Murono and K.Watanabe of Tohoku University.

I particularly wish to thank the people in the Research Center for Neutrino Science. Thanks to them, I could spend fruitful two years.

And last, but not the least, I would like to thank my family for their continuous support and encouragement.

Makoto Ueki

February 17, 1999.

Contents

List of Figures

List of Tables

Chapter 1

Introduction

Symmetry plays an important role in the physics laws. It is not always conserved and violated in some parts. One of them is CP symmetry. The violation of CP symmetry means the violation of symmetry between matter and antimatter. Therefore it could provide an important key to understanding the major question of why we live in a matter-dominated Universe, which is evolved from the matter-antimatter symmetric Big Bang.

CP violation was first discovered in the decays of neutral K mesons, and its origin is still one of the outstanding mysteries of elementary particle physics. In 1973, Kobayashi and Maskawa(KM) showed that CP violation could be explained by the quark mixing within the framework of Standard Model if there were three generations, six quarks. In 1980, Sanda and Carter pointed out that KM model contained the possibility of rather sizable CP violating asymmetries in B meson system. This means, by studying the decays of B mesons, it would be possible to measure the CP violating parameter which has not been determined yet in the K meson decays due to their small CP asymmetry, and to perform decisive tests of the KM model.

Since B mesons have many decay modes and the branching ratio of each mode is small, we need a facility to produce many B mesons, a B-factory, in order to measure the CP asymmetry in the B meson system. Several B-factory experiments are scheduled or have been carried out around the world. Among them, the BELLE experiment is projected at KEK in Japan. Both the accelerator, KEKB which is an asymmetric e^+e^- collider producing moving B mesons and the BELLE detector which consists of several detectors to detect the various final state particles are in their final construction stage and getting

ready for starting the first physics program in April 1999.

The BELLE collaboration consists of about fifty institutes from eleven countries. Tohoku University participates in BELLE experiment and is in charge of the KLM detector together with Aomori University, KEK, Osaka city University, Tohoku Gakuin University, Princeton University and Virginia Polytechnic Institute and State University. The KLM detector which is designed to detect both K_L^0 mesons and muons is located outside the superconducting solenoid. K_L^0 detection is indispensable for detecting the expected CP violating mode $B^0 \rightarrow J/\psi K_L^0$. Muon identification is also essential for the flavor tagging of the B meson and for the studies of rare B decays in addition to detecting muons from the $J/\psi \rightarrow \mu^+\mu^-$. The KLM detector is composed of a sandwich of 47 mm iron absorber plates and detectors in 44 mm gaps. RPC(Resistive Plate Counter) was chosen as the detector for its simplicity, robustness and low cost. RPCs have been used in cosmic ray or accelerator experiments so far. As their resistive electrodes, Bakelite(phenolic polymer) has been mainly used. The characteristic of the BELLE RPC is that the glass is used as the electrodes.

RPC is a gaseous detector and a selection of nonflammable gas mixture is an important issue for safety or for avoiding complicated procedures that are required for flammable gases. It is also better to use an environmentally safe gas mixture. From this point of view, the use of Freon which we have been using is not desirable since it has a high global warming potential even if it is not an ozone-depleting substance.

In this paper, study of nonflammable gas mixture and freonless gas mixture for the glass RPC are described. The organization of this thesis is as follows.

- Chapter 2: BELLE Experiment
- Chapter 3: K_L^0/μ Detector (KLM)
- Chapter 4: Resistive Plate Counter (RPC)
- Chapter 5: Study of Nonflammable Gas Mixture
- Chapter 6: Study of Freonless Gas Mixture
- Chapter 7: Summary

Chapter 2

BELLE Experiment

2.1 Physics with BELLE

2.1.1 Discovery of CP Violation

CP transformation is the product of parity transformation(P) and charge conjugation(C). Parity transformation means a space inversion under which $\vec{x} \rightarrow -\vec{x}$. It changes the sign of momenta, $\vec{p} \rightarrow -\vec{p}$, leaving spins unchanged. Charge conjugation is a transformation which relates particles and anti-particles, leaving momenta and spins unchanged. The electro-magnetic and the strong interactions are invariant under these transformations.

In 1956, Lee and Yang confidently argued that Parity invariance is not conserved in the weak interaction after examining all the data of experiments on the weak interaction [1]. The first experiment to verify their argument was performed by Wu, *et al.*[2]. They studied the β-decays of polarized cobalt nuclei,

$$^{60}Co \rightarrow ^{60} Ni^* + e^- + \overline{\nu}_e. \tag{2.1}$$

The nuclear spins in a sample of ^{60}Co were aligned by an external magnetic field, and an asymmetry in the direction of emitted electrons was observed. The electron was emitted preferentially opposite to the direction of the spin of the ^{60}Co nucleus. This is explained if only a right-handed anti-neutrino,$\overline{\nu}_R$, and a left-handed electron, e_L, is emitted. The subsequent many experiments concluded that indeed only $\overline{\nu}_R$(and ν_L) was involved in weak interactions.

Also the weak interaction is not invariant under charge conjugation. A simple example

is the decay of charged pion,

$$\pi^+ \rightarrow \mu^+ + \nu_{\mu L}. \tag{2.2}$$

For charge conjugated decay,

$$\pi^- \rightarrow \mu^- + \overline{\nu}_{\mu L}. \tag{2.3}$$

Since ν_L is not able to be transformed into $\overline{\nu}_L$, C invariance is violated. However, if we combine C and P as one CP transformation,

$$\pi^- \rightarrow \mu^- + \overline{\nu}_{\mu R}. \tag{2.4}$$

CP transforms ν_L into $\overline{\nu}_R$, thus CP is conserved. Another suggestion that supports CP invariance comes from CPT theorem. CPT theorem which is an important property of local field theories insures CPT invariance, where T means the time reversal transformation changing $t \rightarrow -t$. Because the evidence of T violation had not been discovered[1], CP was believed to be invariant until CP violation was observed in the neutral K meson system in 1964 [3].

K^0 which consists of d and $\overline{s}$ quarks, and its anti-particle, $\overline{K}^0(\overline{d}s)$ are generated by the strong interaction and are eigenstates of the strong interaction. They differ in their strangeness, S. K^0 has $S = +1$, while $\overline{K}^0$ has $S = -1$. Since the strangeness is conserved in the strong interactions, they are generated uniquely, thus, $\pi^- p \rightarrow \Lambda^0 K^0$ can occur, but $\pi^- p \rightarrow \Lambda^0 \overline{K}^0$ can not. However, the strangeness is not conserved in the weak interaction through which they decay. For example, both K^0 and $\overline{K}^0$ can decay into $\pi^+\pi^-$ and $\pi^+\pi^-\pi^0$, whose strangeness are zero. The well defined masses and lifetimes of the particles are the physical states, which are the eigenstates of the total Hamiltonian including both strong and weak interactions. These states are given by linear combination of K^0 and $\overline{K}^0$.

Since the CP transformation of K^0 produces $\overline{K}^0$,

$$CP|K^0\rangle = |\overline{K}^0\rangle. \tag{2.5}$$

If CP is conserved, the physical eigenstates are the eigenstates of CP. We define

$$|K_1^0\rangle = \frac{1}{\sqrt{2}}(|K^0\rangle + |\overline{K}^0\rangle), \quad |K_2^0\rangle = \frac{1}{\sqrt{2}}(|K^0\rangle - |\overline{K}^0\rangle), \tag{2.6}$$

[1]We do not have any evidence for T violation yet.

then,

$$CP|K_1^0\rangle = +|K_1^0\rangle, \quad CP|K_2^0\rangle = -|K_2^0\rangle. \tag{2.7}$$

Thus $|K_1^0\rangle$ and $|K_2^0\rangle$ are the eigenstates of CP having $CP = +1$ and $CP = -1$ respectively.

The neutral K mesons decay into $\pi^+\pi^-$ and $\pi^+\pi^-\pi^0$. The $\pi^+\pi^-$ state has $CP = +1$ if its angular momentum is zero, a grand state, because both C and P interchange the two pions. On the other hand, the $\pi^+\pi^-\pi^0$ state has $CP = -1$ for another π^0 has $CP = -1$. Hence, if CP is conserved, K_1^0 is to decay into $\pi^+\pi^-$ (or $\pi^0\pi^0$) and K_2^0 is to decay into $\pi^+\pi^-\pi^0$ (or $\pi^0\pi^0\pi^0$). Since the phase space for 2π decays is larger than that for 3π decays, the kaon decaying into 2π's has shorter lifetime than that into 3π's. Therefore the former is called K_S(Short) and the latter is K_L(Long). If CP is conserved, we can write

$$K_S = K_1^0, \quad K_L = K_2^0. \tag{2.8}$$

However, $K_L \to 2\pi$ was observed. There are three interpretations for this CP violating phenomenon.

(a) K_L slightly contains K_1^0 having $CP = -1$ (Indirect CP violation).

K_L state is described with a complex parameter ϵ as

$$|K_L\rangle = \epsilon|K_1\rangle + |K_2\rangle, \tag{2.9}$$

where ϵ represents the magnitude of CP asymmetry and is given $|\epsilon| = 2.3 \times 10^{-3}$.

(b) K_2^0 having $CP = +1$ directly decays into 2π's having $CP = -1$ (Direct CP violation).

$$K_2^0 \to \pi^+\pi^- \text{ or } \pi^0\pi^0 \tag{2.10}$$

(c) Both (a) and (b).

Note that we do not have any evidence for direct CP violation yet.

2.1.2 Standard Model Description of CP Violation

CP violation in the three generation Standard Model of electroweak interactions stems from the fact that the mass eigenstates are different from the weak interaction eigenstates as far as quarks are concerned. (This may also be true in the lepton sector as shown in the recent experiment on atmospheric neutrinos indicating neutrino oscillations [5].)

The main part of the Standard Model is the Electroweak Model having $SU(2)_L \times U(1)_Y$ gauge symmetry. In order to account for CP violation, its Lagrangian needs to have a nontrivial complex phase. The complex phase only appears in the part of Yukawa interactions between quarks and Higgs scalars,

$$-\mathcal{L}_{Yukawa} = f_{ij}\overline{q}_{iL}\Phi n_{jR} + g_{ij}\overline{q}_{iL}\tilde{\Phi}p_{jR} + hermitian\ conjugate, \tag{2.11}$$

where,

$$\Phi = \begin{pmatrix} \phi^+ \\ \phi^0 \end{pmatrix}, \tag{2.12}$$

$$\tilde{\Phi} = i\sigma^2\Phi^* = \begin{pmatrix} \phi^{0*} \\ -\phi^- \end{pmatrix}, \tag{2.13}$$

$$q_{iL} = \begin{pmatrix} p_i \\ n_i \end{pmatrix}, \tag{2.14}$$

$$p_{iL(R)} = \frac{1}{2}(1 \mp \gamma_5)p_i, \quad p_i = (u, c, t), \tag{2.15}$$

$$n_{iL(R)} = \frac{1}{2}(1 \mp \gamma_5)n_i, \quad n_i = (d, s, b), \tag{2.16}$$

$f_{ij},\ g_{ij}$; arbitrary complex number.

Under the spontaneous symmetry breaking, $SU(2)_L \times U(1)_Y \rightarrow U(1)_{EM}$, the complex field ϕ^0 is shifted and becomes real and the field ϕ^+ vanishes, then the Higgs has a vacuum expectation value, $\langle\phi\rangle_0$,

$$\langle\phi\rangle_0 = \frac{1}{\sqrt{2}}\begin{pmatrix} 0 \\ v \end{pmatrix}. \tag{2.17}$$

After spontaneous symmetry breaking, what remain for $\mathcal{L}_{Yukawa}$ are the mass terms,

$$-\mathcal{L}_{mass} = \frac{v}{\sqrt{2}}(f_{ij}\overline{p}_{iL}p_{jR} + g_{ij}\overline{n}_{iL}n_{jR}) + h.c. \tag{2.18}$$

$$\equiv \quad M^p_{ij}\overline{p}_{iL}p_{jR} + M^n_{ij}\overline{n}_{iL}n_{jR} + h.c. \tag{2.19}$$

$$M^p_{ij} = \frac{v}{\sqrt{2}}f_{ij}, \quad M^n_{ij} = \frac{v}{\sqrt{2}}g_{ij} \tag{2.20}$$

Since M^p_{ij} and M^n_{ij} are not diagonal generally, in order to see the mass eigenstates we must diagonalize these mass matrices. We know that any square matrix, hermitian or not, can be diagonalized by means of two unitary matrices;

$$U^\dagger_L M^p U_R = M^u_{diag}, \quad D^\dagger_L M^n D_R = M^d_{diag}, \tag{2.21}$$

$$p_{L(R)} = U_{L(R)}u_{L(R)}, \quad n_{L(R)} = D_{L(R)}d_{L(R)}, \tag{2.22}$$

where, $u_{L(R)}$ and $n_{L(R)}$ are the mass eigenstates. The interactions of quarks with W bosons are then given by in the mass eigenstates,

$$-\mathcal{L}_W \quad = \quad \frac{g}{\sqrt{2}}\overline{p}_{iL}\gamma_\mu n_{iL}W_{+\mu} + h.c. \tag{2.23}$$

$$= \quad \frac{g}{\sqrt{2}}\overline{u}_{iL}V_{ij}\gamma_\mu d_{iL}W_{+\mu} + h.c., \tag{2.24}$$

$$V = U^\dagger_L D_L. \tag{2.25}$$

In the weak interaction, the quarks interact with W through the $SU(2)_L$ doublet,

$$q_{iL}: \quad \begin{pmatrix} u \\ d' \end{pmatrix}_L \quad \begin{pmatrix} c \\ s' \end{pmatrix}_L \quad \begin{pmatrix} t \\ b' \end{pmatrix}_L, \tag{2.26}$$

where,

$$\begin{pmatrix} d' \\ s' \\ b' \end{pmatrix} = V \begin{pmatrix} d \\ s \\ b \end{pmatrix}. \tag{2.27}$$

Hence, it is not the quark mass eigenstates but the mixing among the different generations of them that interact with W bosons. The mixing matrix V is referred to as Kobayashi-Maskawa(KM) matrix [6].

The KM matrix is a unitary 3×3 matrix and contains four physical parameters, among which three are real rotation angles and the remaining one is a phase. It is this single phase that causes CP violation.

2.1.3 The Unitarity Triangle

In the KM model, CP violation is attributed to a single phase in the quark mixing matrix,

$$V = \begin{pmatrix} V_{ud} & V_{us} & V_{ub} \\ V_{cd} & V_{cs} & V_{cb} \\ V_{td} & V_{ts} & V_{tb} \end{pmatrix}. \tag{2.28}$$

The nontrivial complex phase is typically assigned to the furthest off-diagonal elements, V_{ub} and V_{td}. It is convenient to use the approximate parameterization of KM matrix suggested by Wolfenstein [7],

$$V = \begin{pmatrix} 1-\frac{\lambda^2}{2} & \lambda & \lambda^3 A(\rho - i\eta) \\ -\lambda & 1-\frac{\lambda^2}{2} & \lambda^2 A \\ \lambda^3 A(1-\rho-i\eta) & \lambda^2 A & 1 \end{pmatrix} + O(\lambda^4), \tag{2.29}$$

where there are four parameters, λ, A, ρ and η. Of the four, λ and A are relatively well determined, less is known about ρ and η that specify the KM CP-violating phase. The parameter λ is well determined from strange particle decays, nuclear β decay, and the production of charm in ν interactions to be [4]

$$\lambda = 0.2196 \pm 0.0023. \tag{2.30}$$

The parameter A is given from the measurement of the branching ratio $Br(b \to cl\nu)$ to be [4]

$$A = 0.819 \pm 0.035. \tag{2.31}$$

The relative strength of $b \to u$ and $b \to c$ transitions in semileptonic B decays determines the ratio [4]

$$|V_{ub}/V_{cb}| = 0.08 \pm 0.02 \quad \text{or} \quad \sqrt{\rho^2+\eta^2} = 0.364 \pm 0.091. \tag{2.32}$$

Unitarity of the KM matrix implies

$$\sum_i V_{ij}^* V_{ik} = \delta_{jk} \tag{2.33}$$

which gives the following relation involving V_{ub} and V_{td},

$$V_{td}V_{tb}^* + V_{cd}V_{cb}^* + V_{ud}V_{ub}^* = 0. \tag{2.34}$$

This expression can form a so-called "Unitarity triangle" in the complex plane, as shown in Figure 2.1. The three internal angles are defined as

$$\phi_1 \equiv arg\left(\frac{V_{cd}V_{cb}^*}{V_{td}V_{tb}^*}\right), \quad \phi_2 \equiv arg\left(\frac{V_{ud}V_{ub}^*}{V_{td}V_{tb}^*}\right), \quad \phi_3 \equiv arg\left(\frac{V_{cd}V_{cb}^*}{V_{ud}V_{ub}^*}\right). \tag{2.35}$$

The BELLE detector is designed to measure these three angles and test if they lie in the range predicted by the KM model [13].

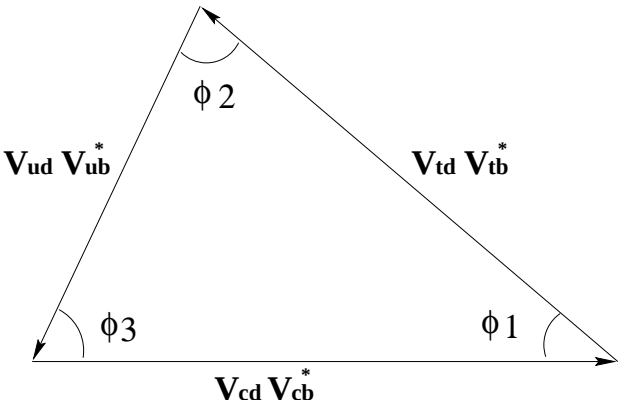

Figure 2.1: Unitarity triangle of the KM matrix.

2.1.4 CP Violation in B decays

• **$B^0 - \overline{B}^0$ mixing**

The neutral B mesons $|B^0\rangle$ and $|\overline{B}^0\rangle$ can mix via Feynman diagrams shown in Figure 2.2. An arbitrary B meson state is given by

$$|\Psi_B(t)\rangle = a(t)|B^0\rangle + b(t)|\overline{B}^0\rangle, \tag{2.36}$$

or,

$$\Psi_B(t) = \begin{pmatrix} a(t) \\ b(t) \end{pmatrix}. \tag{2.37}$$

And it is governed by a time-dependent Schrödinger equation

$$i\frac{\partial}{\partial t}|\Psi_B(t)\rangle = \mathbf{H}|\Psi_B(t)\rangle = E|\Psi_B(t)\rangle, \tag{2.38}$$

where $\mathbf{H}$ is a 2×2 matrix, and its matrix elements can be written as

$$\mathbf{H} = \begin{pmatrix} H_{11} & H_{12} \\ H_{21} & H_{22} \end{pmatrix} = \begin{pmatrix} \langle B^0|\mathbf{H}|B^0\rangle & \langle B^0|\mathbf{H}|\overline{B}^0\rangle \\ \langle \overline{B}^0|\mathbf{H}|B^0\rangle & \langle \overline{B}^0|\mathbf{H}|\overline{B}^0\rangle \end{pmatrix}, \tag{2.39}$$

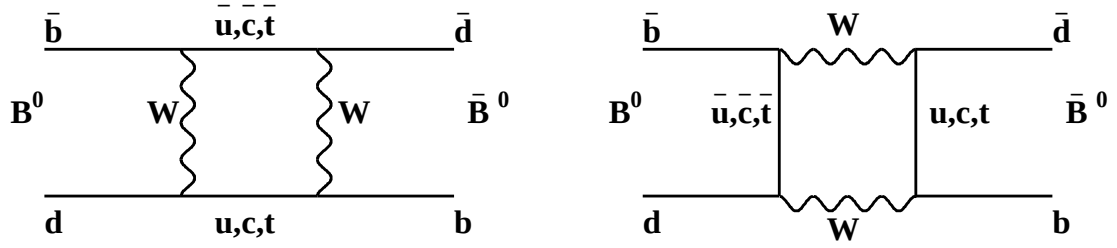

Figure 2.2: Box diagrams of $B^0 - \overline{B}^0$.

where the states are normalized to unity. Considering that the wave function of the decaying particle is in general described as

$$\Psi(t) = \Psi(0)e^{-i(m-\frac{i}{2}\Gamma)t}, \tag{2.40}$$

then we have

$$\mathbf{H} = \mathbf{M} - \frac{i}{2}\mathbf{\Gamma}, \tag{2.41}$$

where $\mathbf{M}$ and $\mathbf{\Gamma}$ are Hermitian 2×2 matrices, which are called the mass and decay matrices, respectively,

$$\mathbf{M} = \begin{pmatrix} m_{11} & m_{12} \\ m_{12}^* & m_{22} \end{pmatrix}, \quad \mathbf{\Gamma} = \begin{pmatrix} \Gamma_{11} & \Gamma_{12} \\ \Gamma_{12}^* & \Gamma_{22} \end{pmatrix}. \tag{2.42}$$

If we assume CPT invariance which guarantees equality of the lifetime between particle and anti-particle, then we have

$$\langle B^0|\mathbf{H}|B^0\rangle = \langle \overline{B}^0|\mathbf{H}|\overline{B}^0\rangle \equiv m_0 - \frac{i}{2}\Gamma_0, \tag{2.43}$$

and thus,

$$\mathbf{H} = \begin{pmatrix} \langle B^0|\mathbf{H}|B^0\rangle & \langle B^0|\mathbf{H}|\overline{B}^0\rangle \\ \langle \overline{B}^0|\mathbf{H}|B^0\rangle & \langle \overline{B}^0|\mathbf{H}|\overline{B}^0\rangle \end{pmatrix} = \begin{pmatrix} m_0 - \frac{i}{2}\Gamma_0 & m_{12} - \frac{i}{2}\Gamma_{12} \\ m_{12}^* - \frac{i}{2}\Gamma_{12}^* & m_0 - \frac{i}{2}\Gamma_0 \end{pmatrix}. \tag{2.44}$$

The eigenstates of this Hamiltonian represent physically meaningful mass eigenstates. The heavy and light eigenstates denoted by B_H and B_L, and their eigenvalues λ_H,λ_L are given by

$$\begin{aligned} |B_H\rangle &= \frac{1}{\sqrt{|p|^2+|q|^2}}\{p|B^0\rangle - q|\overline{B}^0\rangle\}, \\ |B_L\rangle &= \frac{1}{\sqrt{|p|^2+|q|^2}}\{p|B^0\rangle + q|\overline{B}^0\rangle\}, \end{aligned} \tag{2.45}$$

$$\begin{aligned} \lambda_H &= m_0 - \frac{i}{2}\Gamma_0 - pq \equiv M_H - \frac{i}{2}\Gamma_H, \\ \lambda_L &= m_0 - \frac{i}{2}\Gamma_0 + pq \equiv M_L - \frac{i}{2}\Gamma_L, \end{aligned} \tag{2.46}$$

where,

$$\begin{aligned} p &= (m_{12} - \frac{i}{2}\Gamma_{12})^{1/2}, \\ q &= (m_{12}^* - \frac{i}{2}\Gamma_{12}^*)^{1/2}. \end{aligned} \tag{2.47}$$

The mass difference ΔM and decay width deference $\Delta\Gamma$ between them are defined as follows:

$$\Delta M \equiv M_H - M_L, \quad \Delta\Gamma \equiv \Gamma_H - \Gamma_L. \tag{2.48}$$

The width difference is, however, expected to be negligible for $B_d(b\overline{d}, \overline{b}d)$ mesons[2],

$$\Delta\Gamma/\Gamma \leq 10^{-2}. \tag{2.49}$$

$\Delta\Gamma$ has not been measured so far, so we neglect it, hence,

$$\Gamma_H = \Gamma_L \equiv \Gamma. \tag{2.50}$$

On the other hand, ΔM has been measured [8],

$$x_d \equiv \Delta M/\Gamma \cong 0.7. \tag{2.51}$$

The time evolution of these mass eigenstates are given as the solutions of (2.38) by

$$\begin{aligned} B_H(t) &= B_H(0)e^{-i(M_H - \frac{i}{2}\Gamma)t}, \\ B_L(t) &= B_L(0)e^{-i(M_L - \frac{i}{2}\Gamma)t}. \end{aligned} \tag{2.52}$$

Now we consider the time evolution of the states B^0 or $\overline{B}^0$ produced in a strong interaction at $t = 0$. A state which is created at time $t = 0$ as initially pure B^0 is denoted $|B^0_{phys}\rangle$, having $B_L(0) = B_H(0) = 1/(2p)$. Similarly an initially pure $\overline{B}^0$ having $B_L(0) = -B_H(0) = 1/(2q)$ is denoted $|\overline{B}^0_{phys}\rangle$. Then, from (2.45) and (2.52) the time evolution of these states are given by

$$\begin{aligned} |B^0_{phys}(t)\rangle &= g_+(t)|B^0\rangle + \frac{q}{p}g_-(t)|\overline{B}^0\rangle, \\ |\overline{B}^0_{phys}(t)\rangle &= \frac{p}{q}g_-(t)|B^0\rangle + g_+(t)|\overline{B}^0\rangle, \end{aligned} \tag{2.53}$$

where,

$$\begin{aligned} g_+(t) &= e^{i(M - \frac{1}{2}\Gamma)t}\cos(\Delta M t/2), \\ g_-(t) &= ie^{i(M - \frac{1}{2}\Gamma)t}\sin(\Delta M t/2), \end{aligned} \tag{2.54}$$

[2]For $B_s(b\overline{s}, \overline{b}s)$ mesons the width difference may be significant

and

$$M \equiv \frac{M_H + M_L}{2}. \tag{2.55}$$

• CP **violation in decay**

If the amplitude for a decay $B \to f$ and its CP conjugate process $\overline{B} \to \overline{f}$ have different magnitudes, CP violation occurs. This type of CP violation is called CP violation in decay, or direct CP violation, which occurs in both charged and neutral decays.

An example of this type is the decay $B^{\pm} \to \pi^0 K^{\pm}$ shown in Figure 2.3. There are at least two different components contributing to the amplitude of these decays, so-called "tree" and "penguin" contributions. These decay amplitudes can then be written as

$$A(B^+ \to \pi^0 K^+) = |A_t| e^{i(\phi_t + \delta_t)} + |A_p| e^{i(\phi_p + \delta_p)}, \tag{2.56}$$

$$A(B^- \to \pi^0 K^-) = |A_t| e^{i(-\phi_t + \delta_t)} + |A_p| e^{i(-\phi_p + \delta_p)}, \tag{2.57}$$

where the suffixes t and p denote "tree" and "penguin", respectively, and $A_i (i = t, p)$ are real amplitudes. Two types of phases appear in the decay amplitudes: the weak phases ϕ_i are the CP violating parameters coming from KM matrix, and have opposite signs. The strong phases δ_i usually arise from rescattering effects due to strong interactions, and have same signs.

The decay widths are estimated to be

$$\Gamma(B^+ \to \pi^0 K^+) \sim |A(B^+ \to \pi^0 K^+)|^2$$

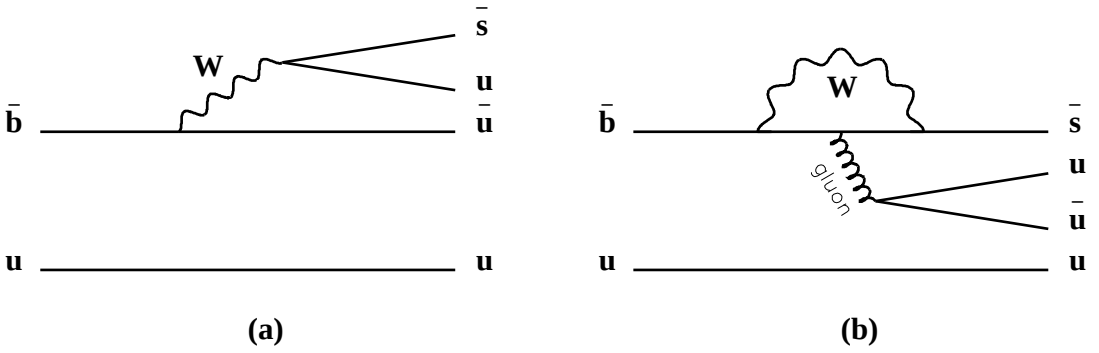

Figure 2.3: Feynman diagrams for the decay $B^+ \to \pi^0 K^+$, (a)Tree diagram, (b)Penguin diagram.

$$= |A_t|^2 + A_p|^2 + 2|A_t||A_p|cos(\Delta\phi + \Delta\delta), \quad (2.58)$$

$$\begin{aligned}\Gamma(B^- \to \pi^0 K^-) &\sim |A(B^- \to \pi^0 K^-)|^2 \\ &= |A_t|^2 + A_p|^2 + 2|A_t||A_p|cos(-\Delta\phi + \Delta\delta), \quad (2.59)\end{aligned}$$

where, $\Delta\phi \equiv \phi_t - \phi_p, \Delta\delta = \delta_t - \delta_p$. Then we have

$$\Gamma(B^+ \to \pi^0 K^+) - \Gamma(B^- \to \pi^0 K^-) \sim -2|A_t||A_p|sin(\Delta\phi)sin(\Delta\delta). \quad (2.60)$$

Therefore CP violation can be observable if $|A_t| \neq 0$, $|A_p| \neq 0$, $sin(\Delta\phi) \neq 0$ and $sin(\Delta\delta) \neq 0$ are satisfied. Hence, there need to be two interfering amplitudes $|A_t|$,$|A_p|$ and these amplitudes must simultaneously have both different weak ϕ_i and different strong phases δ_i.

Note that calculations of direct CP-violating asymmetries have significant theoretical uncertainties. Especially, it is very hard to calculate the non-trivial strong phase shifts which are required for direct CP violation.

• **CP violation in the interference of decay and mixing**

Consider decays of neutral B mesons into final states f_{CP}, which are accessible in both B^0 and $\overline{B}^0$ decays [9]. Due to $B^0 - \overline{B}^0$ mixing, there exist two decay channels,

$$B^0 \to B^0 \to f_{CP}, \quad B^0 \to \overline{B}^0 \to f_{CP}. \quad (2.61)$$

The decay amplitudes for pure B^0, $\overline{B}^0$ states are defined as,

$$\mathcal{A}_{CP} \equiv \langle f_{CP}|B^0\rangle, \quad \overline{\mathcal{A}}_{CP} \equiv \langle f_{CP}|\overline{B}^0\rangle, \quad (2.62)$$

and for convenience, we also define

$$r_{f_{CP}} \equiv \frac{q}{p}\frac{\overline{\mathcal{A}}_{CP}}{\mathcal{A}_{CP}}. \quad (2.63)$$

Then time-dependent decay amplitudes are given from (2.53) and (2.54) by

$$\begin{aligned}\langle f_{CP}|B^0_{phys}(t)\rangle &= \mathcal{A}_{CP}[g_+(t) + r_{f_{CP}}g_-(t)], \\ \langle f_{CP}|\overline{B}^0_{phys}(t)\rangle &= \mathcal{A}_{CP}\left(\frac{p}{q}\right)[g_-(t) + r_{f_{CP}}g_+(t)]. \quad (2.64)\end{aligned}$$

The time-dependent decay widths are, hence, written as

$$\begin{aligned}\Gamma(B^0_{phys}(t) \to f_{CP}) &= |\mathcal{A}_{CP}|^2 e^{-\Gamma t}[\frac{1+|r_{f_{CP}}|^2}{2} + \frac{1-|r_{f_{CP}}|^2}{2}\cos(\Delta M t) - \mathrm{Im} r_{f_{CP}} \sin(\Delta M t)], \\ \Gamma(\overline{B}^0_{phys}(t) \to f_{CP}) &= |\mathcal{A}_{CP}|^2 e^{-\Gamma t}[\frac{1+|r_{f_{CP}}|^2}{2} - \frac{1-|r_{f_{CP}}|^2}{2}\cos(\Delta M t) + \mathrm{Im} r_{f_{CP}} \sin(\Delta M t)].\end{aligned} \tag{2.65}$$

Here we define the time-dependent CP asymmetry,

$$A_{f_{CP}}(t) \equiv \frac{\Gamma(B^0_{phys}(t) \to f_{CP}) - \Gamma(\overline{B}^0_{phys}(t) \to f_{CP})}{\Gamma(B^0_{phys}(t) \to f_{CP}) + \Gamma(\overline{B}^0_{phys}(t) \to f_{CP})}. \tag{2.66}$$

Substituting (2.65) for (2.66), we have

$$A_{f_{CP}}(t) = \frac{(1-|r_{f_{CP}}|^2)\cos(\Delta M t) - 2\mathrm{Im} r_{f_{CP}} \sin(\Delta M t)}{1+|r_{f_{CP}}|^2}. \tag{2.67}$$

In the case of B^0_d, $|\Gamma_{12}| \ll |M_{12}|$, so q/p can be approximated as

$$\begin{aligned}\frac{q}{p} &= \sqrt{\frac{m^*_{12} - i\Gamma^*_{12}/2}{m_{12} - i\Gamma_{12}/2}} \\ &\approx \sqrt{\frac{m^*_{12}}{m_{12}}} = \frac{V^*_{tb}V_{td}}{V_{tb}V^*_{td}} \equiv e^{-2i\phi_M},\end{aligned} \tag{2.68}$$

where we use the fact that m_{12} is related to the KM matrix such that

$$m_{12} \propto (V_{tb}V^*_{td})^2, \tag{2.69}$$

and ϕ_M shows the phase of mixing(Figure 2.2), which is related to the phase of the KM matrix($\phi_M = \phi_1$,in B^0_d case). If direct CP violation is not involved in the decay process and only a single weak phase ϕ_D contributes to the decay amplitudes, then $\mathcal{A}_{CP}/\overline{\mathcal{A}}_{CP}$ can be written as

$$\mathcal{A}_{CP}/\overline{\mathcal{A}}_{CP} = \eta_f e^{-2i\phi_D}, \tag{2.70}$$

where η_f is the CP eigenvalue of the final state f_{CP} and takes $\eta_f = \pm 1$. Finally we have

$$\begin{aligned}A_{f_{CP}}(t) &= \eta_f \mathrm{Im} r_{f_{CP}} \sin(\Delta M t) \\ &= \eta_f \sin 2(\phi_M + \phi_D)\sin(\Delta M t).\end{aligned} \tag{2.71}$$

This type of CP violation is called CP violation in the interference of decay and mixing, and of great importance at the BELLE experiment.

2.1.5 Determination of the Shape of Unitarity Triangle

At the B factory, B^0 and $\overline{B}^0$ are produced in a coherent $B^0\overline{B}^0$ state via $\Upsilon(4S)$ resonance. They remain in this coherent state until one of particles decays. That is, at any time until one particle decays, there exists always one B^0 and one $\overline{B}^0$, although each of the two particles evolve in time as described above in terms of $B^0 - \overline{B}^0$ mixing. Thus, when one particle decays, the other particle that will continue to evolve is sure to be antiparticle of the decaying particle.

As mentioned above, decays of neutral B mesons into a CP eigenstate f_{CP} produce time-dependent CP asymmetries given by

$$A_{f_{CP}}(t) = \frac{\Gamma(B^0 \to f_{CP}) - \Gamma(\overline{B}^0 \to f_{CP})}{\Gamma(B^0 \to f_{CP}) + \Gamma(\overline{B}^0 \to f_{CP})} = \sin 2\phi_{CP} \cdot \sin(\Delta M \cdot t), \tag{2.72}$$

where, ΔM denotes the mass difference between the two B^0 mass eigenstates and t shows the proper time difference between the B^0 and $\overline{B}^0$ decays. The t range is from $-\infty$ to ∞, thus the time-integrated asymmetry vanishes. Therefore a determination of t is indispensable for measuring a CP asymmetry in experiments at the $\Upsilon(4S)$. This is why we use asymmetric energy beams at the B factory – the resulting motion of the center of mass(CM) allows t to be measured. The angle ϕ_{CP} is the phase concerning the $B^0 - \overline{B}^0$ mixing amplitude and the $B^0 \to f_{CP}$ decay amplitude and is directly related to the internal angles of the unitarity triangle. Thus, by measuring the time evolution of B decays, we can determine the unitarity triangle angles.

It is necessary to know which B^0 or $\overline{B}^0$ decays into a CP eigenstate f_{CP}; this is called flavor tagging. It can be achieved by tagging the decays specific to B^0 or $\overline{B}^0$, such as $B^0 \to l^+\nu X$,$\overline{B}^0 \to l^-\nu X$, and $B^0 \to K^+X$, $\overline{B}^0 \to K^-X$. Figure 2.4 illustrates an example of the time-dependent CP asymmetry measurement, where $B^0 \to J/\psi K_L$ mode whereby ϕ_1 can be measured is shown.

- **ϕ_1 measurement**

The ϕ_1 angle can be measured via the decay $B^0 \to J/\psi K_S$. Especially $B^0 \to J/\psi K_S \to l^+l^-\pi^+\pi^-$ is the most promising mode since the branching ratio for this decay has been measured and the signals are very clean with no appreciable background. Figure 2.5

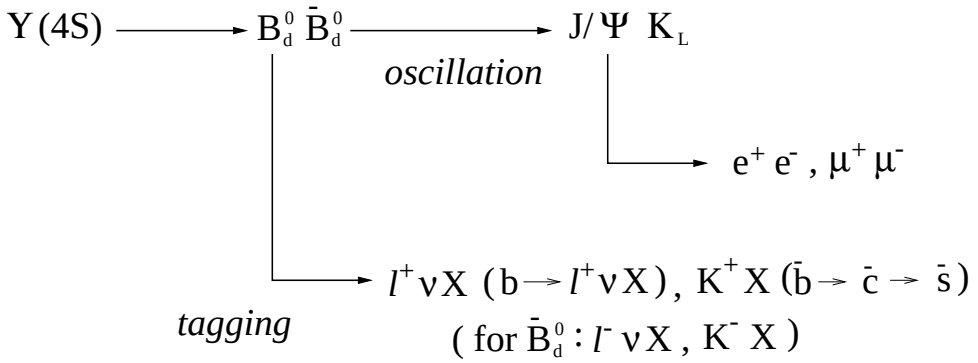

Figure 2.4: Detection of $B^0 \to J/\psi K_L$.

shows the Feynman diagrams for this decay. The weak phase in the tree diagrams is represented by $V_{cb}^* V_{cs}$. There are additional contributions from the penguin diagram represented by $V_{ib}^* V_{is} (i = u, c, t)$. We can, however, regard these as almost equal to $V_{cb}^* V_{cs}$ by considering $\sum V_{ib}^* V_{is} = 0$ and $|V_{cb}^* V_{cs}|, |V_{tb}^* V_{ts}| \gg |V_{ub}^* V_{us}|$. Thus the measurement of ϕ_1 via $B^0 \to J/\psi K_S$ is straightforward. Other possibilities are the decays $B^0 \to J/\psi K_L$ and $B^0 \to D^{(*)} D^{(*)}$.

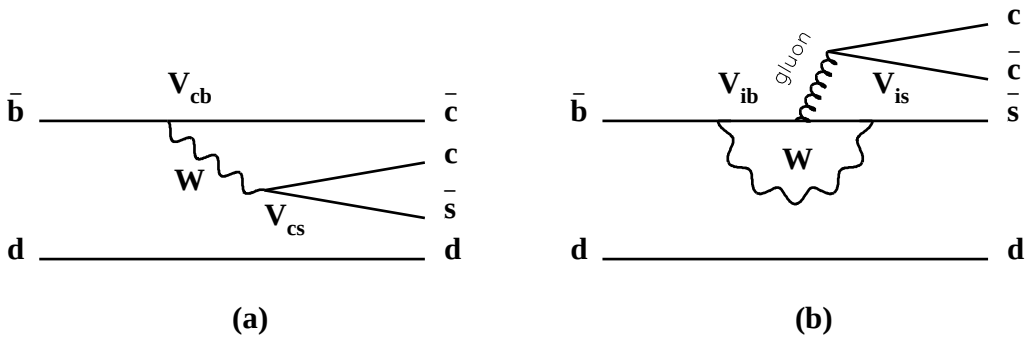

Figure 2.5: Diagrams for $B^0 \to J/\psi K_S$,(a) Tree diagram and (b) Penguin diagram.

• ϕ_2 **measurement**

The ϕ_2 angle can be obtained from the decay $B^0 \to \pi^+\pi^-$. The weak phase in the tree diagram(Figure 2.6(a)) is given by $V_{ub}^* V_{ud}$. On the other hand, the weak phases in the penguin diagram(Figure 2.6(b)) is given by $V_{id} V_{is}^* (i = u, c, t)$. In $B^0 \to \pi^+\pi^-$ case, every $V_{id} V_{is}^* (i = u, c, t)$ is same order $O(\lambda^3)$, then the weak phases in the penguin diagram is different from that in the tree diagram. Thus we cannot relate the experimental data directly to the ϕ_2 angle. In principle, the effect of the penguin contribution can be

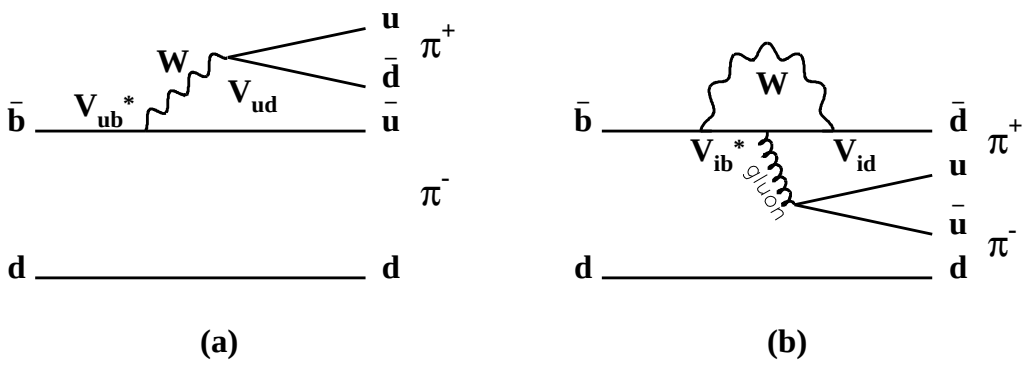

Figure 2.6: Diagrams for $B^0 \to \pi^+\pi^-$,(a) Tree diagram and (b) Penguin diagram.

eliminated by means of an isospin analysis of the amplitude for $B^0 \to \pi^+\pi^-$, $B^0 \to \pi^0\pi^0$ and $B^\pm \to \pi^\pm\pi^0$[10].

• ϕ_3 **measurement**

In principle, ϕ_3 can be determined from the time dependent CP asymmetry for $B_s^0 \to \rho K_S$ in analogy to the ϕ_1 via $B^0 \to J/\psi K_S$ and the ϕ_2 via $B^0 \to \pi^+\pi^-$. There are, however, ambiguities from penguins and difficulties in using B_S decay modes.

Another possible way to determine ϕ_3 is to measure direct CP violation in $B^\pm \to \{D^0, \overline{D}^0, D_{CP}\}K^\pm$ or $B^0(\overline{B}_d^0) \to \{D^0, \overline{D}^0, D_{CP}\}K_S$ decays [11], where D_{CP} means the CP eigenstate of D^0. There are no penguin contributions in these modes, only the tree diagrams shown in Figure 2.7 contribute to these decays. The decay amplitudes can be written as

$$A(B^+ \to D^0 K^+) \equiv A_D = V_{ub}^* V_{cs} e^{i\delta_D}, \tag{2.73}$$

$$A(B^+ \to \overline{D}^0 K^+) \equiv A_{\overline{D}} = V_{cb}^* V_{us} e^{i\delta_{\overline{D}}}, \tag{2.74}$$

where δ_D and $\delta_{\overline{D}}$ are hadronic phases. Since the CP eigenstates of the D^0 are given by

$$D_{1,2} \equiv (D^0 \pm \overline{D}^0)/\sqrt{2}, \tag{2.75}$$

its decay width is calculated as

$$\Gamma[B^+ \to D_{CP} K^+] = \int d\Gamma \frac{|A_D|^2}{2}[1 + |r_D|^2 \pm 2 r_D cos(\phi_3 - \pi + \delta_s)], \tag{2.76}$$

where,

$$r_D = |A_{\overline{D}}/A_D|, \quad \delta_s = \delta_D - \delta_{\overline{D}}. \tag{2.77}$$

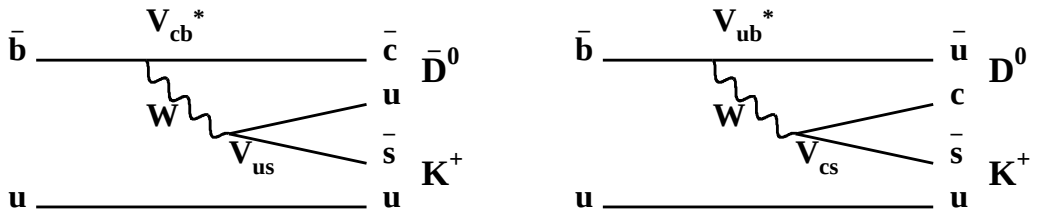

Figure 2.7: Diagrams for (a) $B^+ \to D^0 K^+$, and (b) $B^+ \to \overline{D}^0 K^+$.

For $B^- \to D_{CP} K^-$ decay, we have

$$\Gamma[B^- \to D_{CP} K^-] = \int d\Gamma \frac{|\overline{A}_D|^2}{2}[1 + |\overline{r}_D|^2 \pm 2 r_D cos(\pi - \phi_3 + \delta_s)]. \tag{2.78}$$

Thus, if the absolute values of four independent amplitudes are measured, ϕ_3 can be obtained. This can be achieved by measuring the branching ratios.

It is also important to measure the sides of the unitarity triangle.

• V_{cb} **and** V_{ub} **measurement**

V_{cb} and V_{ub} can be determined from inclusive semileptonic B decays[3]. However, The inclusive mode rates contain a model-dependent constant,

$$\Gamma(b \to c l\nu) \;=\; \frac{G_F^2 m_b^5}{192\pi^3} |V_{cb}|^2 \Phi\Big(\frac{m_c}{m_b}\Big), \tag{2.79}$$

where Φ is a phase factor and b-quark mass m_b has large uncertainty. Another way is to use the exclusive $B \to D^* l\nu$ decay. In Heavy Quark Effective Theory(HQET), the hadronic form factors are normalized at the $B \to D^* l\nu$ kinematic endpoint. Although the event rate near the kinematic endpoint is small, a determination $|V_{cb}|$ from this rate has small model-dependent systematic error. Thus we need to produce a huge number of B mesons for this measurement.

The value $|V_{ub}/V_{cb}|$ can be determined from inclusive decays $b \to u l\nu$ and $b \to c l\nu$ by

$$\frac{\Gamma(b \to u l\nu)}{\Gamma(b \to c l\nu)} = \frac{\Phi(m_u/m_b)}{\Phi(m_c/m_b)} \Big|\frac{V_{ub}}{V_{cb}}\Big|^2, \tag{2.80}$$

although model-dependent uncertainties are here, too.

[3] "Inclusive" semileptonic B decays mean $B \to X l\nu$, where X is arbitrary if permitted.

- V_{td} **measurement**

V_{td} can be obtained from $B_d^0 - \overline{B}_d^0$ mixing. V_{td} is related to ΔM by

$$\Delta M = \frac{G_F^2}{6\pi^2} m_B m_t^2 F\left(\frac{m_t^2}{m_W^2}\right) \eta_{QCD} B_{B_d} f_{B_d}^2 |V_{tb}^* V_{td}|^2, \tag{2.81}$$

where m_t is the top quark mass, F is a function dependent on m_t and m_W, η_{QCD} is a factor for QCD corrections, B_{B_d} is a "bag" factor used to account for the vacuum insertion approximation, and f_{B_d} is a form factor of the B_d meson. By measuring ΔM, we can determine $|V_{tb}^* V_{td}|$. However, $B_{B_d} f_{B_d}^2$ has large ambiguities.

Another possibility is to measure the ratio of radiative decay $B \to \rho\gamma$ and $B \to K^*\gamma$ which is given approximately by $|V_{td}|^2/|V_{ts}|^2$.

Figure 2.8 summarizes how we determine the shape of the unitarity triangle.

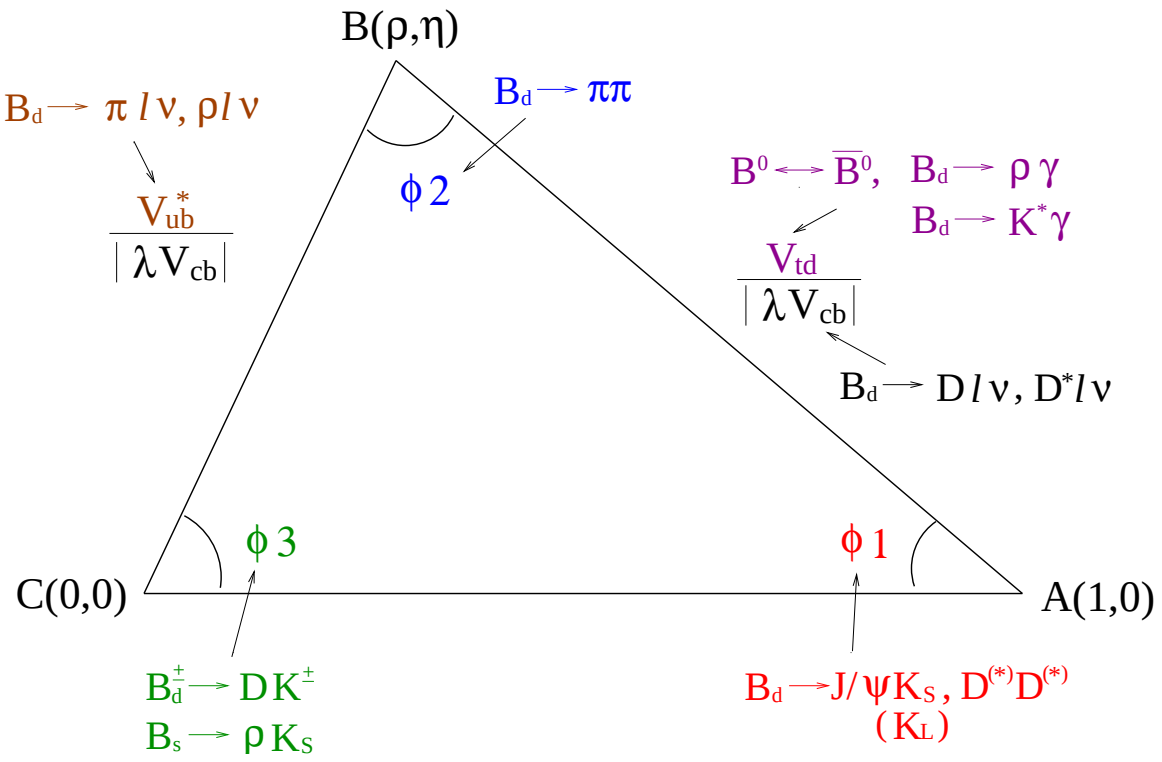

Figure 2.8: Determination of the shape of Unitarity triangle.

2.2 Accelerator(KEKB)

KEKB is an asymmetric electron-positron collider designed to study CP violation in the B meson system with a center of mass energy of 10.58 GeV. B mesons are produced via the $\Upsilon(4S)$ resonance. However, the mass difference between $\Upsilon(4S)$ and $B\overline{B}$ is so small that the produced B mesons only have 0.34 GeV/c at the most and hardly move in rest frame. Then, in order to measure the time evolution of B mesons, an asymmetric collider which produces moving $\Upsilon(4S)$, namely moving B mesons along the beam axis in the laboratory frame is required.

The beam energy asymmetry is generally given by Lorentz boost parameter $\beta\gamma$ to be

$$\beta\gamma = \frac{E_- - E_+}{\sqrt{s}},$$

where, E_- and E_+ represent the energy of electron and positron respectively, and $\sqrt{s}$ is the rest energy of $\Upsilon(4S)$, 10.58 GeV/c^2. The larger the energy asymmetry, the more precise the time evolution measurement of B mesons becomes. On the other hand, considering the detector acceptance and other B decay modes that are not related to the time evolution measurement, smaller energy asymmetry is desirable. Figure 2.9 shows the integrated luminosity required for measuring CP asymmetry with a 3σ significance as a function of $\beta\gamma$. We can find that the integrated luminosity is almost stationary in the region of $\beta\gamma = 0.4 \sim 0.8$. Combining these considerations, $\beta\gamma = 0.42$ has been chosen at KEKB, and the beam energy of electron and positron are determined to be

$$\begin{aligned} E_- &= 8.00\ GeV, \\ E_+ &= 3.50\ GeV, \end{aligned}$$

respectively. Then, the average momentum of the produced B mesons becomes about 2.3 GeV/c in the laboratory frame. Electrons have higher energy than positrons in order to avoid ion trapping, which becomes much serious at low energies. Positron ring, therefore, is called low-energy ring(LER) and electron ring high energy ring(HER).

The overall layout of KEKB is shown in Figure 2.10 and its main parameters are listed in Table 2.1. The two rings are installed side by side in the TRISTAN tunnel of 3 km circumference. KEKB has only one interaction point(IP) in the Tsukuba experimental hall where the BELLE detector is installed. The straight section at Fuji is used for

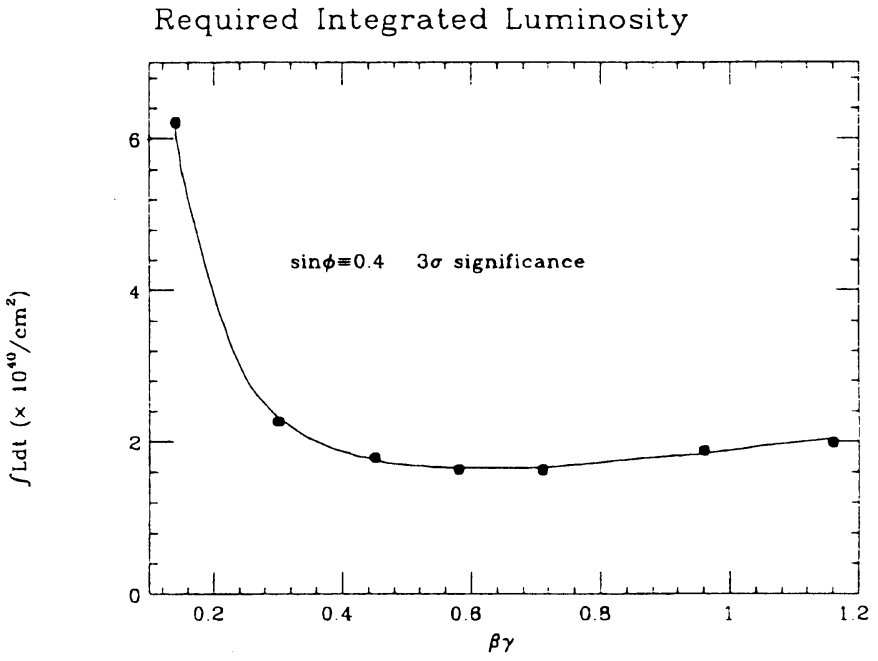

Figure 2.9: Integrated luminosity required for measuring CP asymmetry.

injecting beams from the Linac, and also for installing RF cavities of the LER. The RF cavities for the HER are installed in the straight sections of Nikko and Oho.

Since B mesons have many decay modes, the branching ratio of each B decay modes is rather small, so in order to measure the CP asymmetry in the B meson system, we need to produce a large number of B mesons. Therefore a large integrated luminosity is required for the B-factory accelerator. It is estimated that at least 100 fb^{-1} integrated luminosity is necessary to measure the important parameters in the Standard Model. To achieve this for the first few years of the experiment, the target peak luminosity for KEKB should be 1.0×10^{34} $\text{cm}^{-2}\text{s}^{-1}$. This luminosity is 250 times as large as that of TRISTAN and 20 times as large as that of CESR at Cornell University which gets the largest luminosity in the world so far. The luminosity L of an electron-positron collider is given by,

$$L = 2.2 \times 10^{34} \xi (1 + r) \left(\frac{EI}{\beta_y^*} \right)_{\pm}, \tag{2.82}$$

where, ξ represents beam-beam tuneshift, r, the ratio of vertical beam size to horizontal beam size at the collision point, I, beam current in A, E, beam energy in GeV, and β^*, beta-value at the interaction point. The signs $+$ and $-$ mean that this formula is

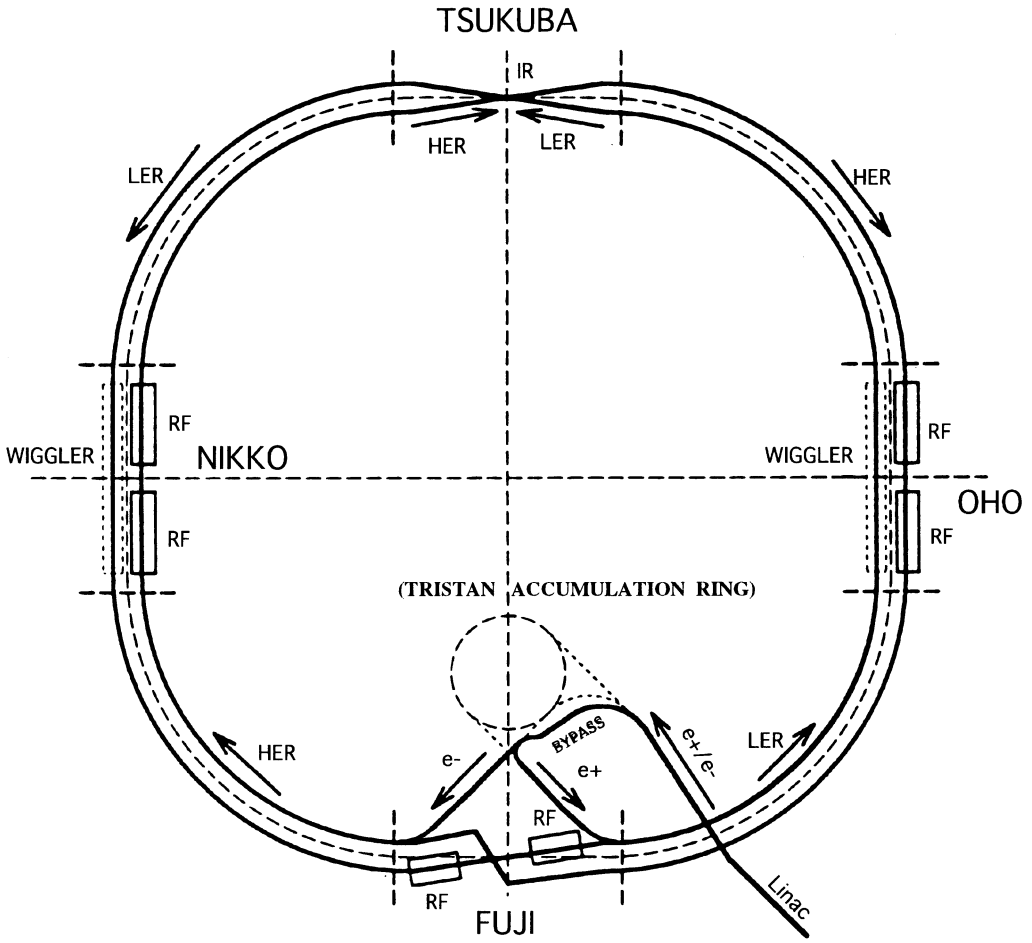

Figure 2.10: Overall layout of KEKB

applicable both to electron and positron rings. The beam-beam tuneshift ξ is usually between 0.03 and 0.05. The beam can be so flat that r becomes as small as the the order a few %. After all, in order to raise the luminosity, we need to choose a small β^*, large ξ and I. In the design of KEKB, we assume $\xi \approx 0.05$ and $\beta^* = 1$ cm (this value is rather small compared with 4 cm of TRISTAN). Then, the beam intensities required for $L = 1.0 \times 10^{34} cm^{-2} s^{-1}$ are 1.1 A for the HER and 2.6 A for the LER. The stored current is distributed into bunches. Each bunch, however, can store a few mA at most. Therefore as much as 5,000 bunches are accumulated in each ring at KEKB. It corresponds to 60 cm bunch spacing. These high-current and large number of bunches let KEKB challenging.

To realize above designs, new technologies are introduced into KEKB. New RF cavities are used; normal-conducting cavities with high stored energy(ARES) and superconducting

Table 2.1: Main parameters of KEKB.

Ring		LER	HER	
Energy	E	3.5	8.0	GeV
Circumference	C	3016.26		m
Luminosity	L	1.0×10^{34}		$cm^{-2}s^{-1}$
Crossing angle	θx	± 11		$mrad$
Tune shifts	$\xi x/\xi y$	0.039/0.052		
Beta function at IP	$\beta x^*/\beta y^*$	0.33/0.01		m
Beam current	I	2.6	1.1	A
Natural bunch length	σz	0.4		cm
Energy spread	$\sigma E/E$	7.7×10^{-4}	7.8×10^{-4}	
Bunch spacing	sB	0.6		m
Particles / bunch		3.3×10^{10}	1.4×10^{10}	
Emittance	$\varepsilon x/\varepsilon y$	$1.8 \times 10^{-8}/3.6 \times 10^{-10}$		m
Synchrotron tune	νs	$0.01 \sim 0.02$		
Betatron tune	$\nu x/\nu y$	45.52/45.08	46.52/46.08	
Momentum compaction factor	αp	$1.0 \times 10^{-4} \sim 2.0 \times 10^{-4}$		
Energy loss / turn	Uo	0.87	4.8	MeV
RF voltage	Vc	5∼10	10∼20	MV
RF frequency	fRF	508.887		MHz
Harmonic number	h	5120		
Energy damping decrement	$To/\tau E$	2.5×10^{-4}	5.9×10^{-4}	
Bending radius	ρ	15.3	76.6	m
Length of bending magnet	Lb	0.86	4.3	m

cavities. As the vacuum duct material, copper has been chosen for its ability to withstand a high peak heat load and to shield radiation from the beam. The salient feature of KEKB is ± 11 mrad crossing angles at the collision point. Advantage of finite crossing angle is that we need no separation dipole magnets where incoming beam to IP emits synchrotron lights, and they may cause backgrounds and complicated interaction region design. One anxiety for finite crossing angle is that it may excite synchrobetatron resonances causing luminosity reduction. To avoid this problem, KEKB is developing crab cavities as a fall-back option. Figure 2.11 illustrates the principle of crab crossing. A pair of crab cavities are located at both sides of IP. Incoming bunches are tilted by a crab cavity and collide head-on in a center-of-mass frame at IP and outgoing bunches are tilted back by the other crab cavity [12].

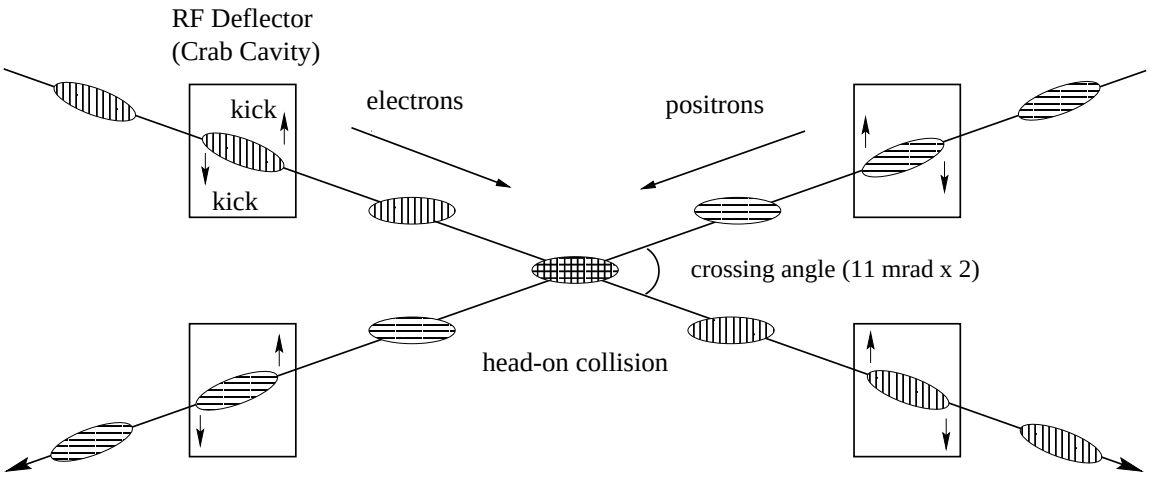

Figure 2.11: Principle of crab crossing.

2.3 BELLE Detector

The BELLE detector is shown in Figure 2.13 and Figure 2.14. The detector is configured around a 1.5 Tesla superconducting solenoid and iron structure surrounding the KEKB beams. B meson decay vertices are measured by a silicon vertex detector(SVD) situated just outside of a cylindrical beryllium beam pipe. Charged particle tracking is provided by a wire drift chamber(CDC). Particle identification is provided by dE/dx measurements in the CDC, and aerogel Čerenkov counter(ACC) and time-of-flight counter(TOF) arrays situated radially outside of the CDC. Electromagnetic showers are detected in an array of CsI crystals located inside the solenoid coil. Muons and K_L^0 mesons are identified by KLM which has arrays of resistive plate counters(RPCs) interspersed in the iron return yoke of the magnet. The detector covers the laboratory polar angles extending from 17° to 150°. Some of the otherwise uncovered angles are instrumented with BGO crystal arrays on the surfaces of the QCS cryostats in the forward and backward directions.

The brief outlines of individual detector components are described in the following [13][14]. The expected performance of the detector is summarized in Table 2.2. In the following, we use the coordinate system defined by Figure 2.12.

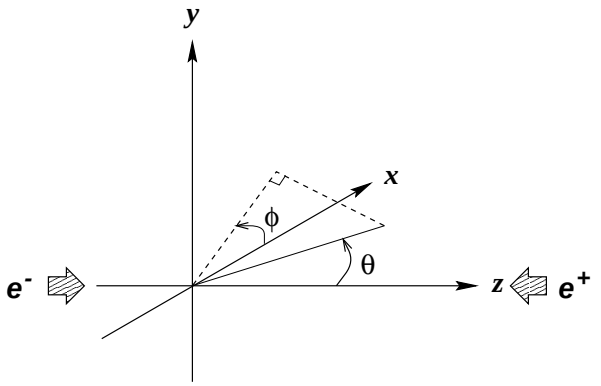

Figure 2.12: Definition of BELLE coordinate system.

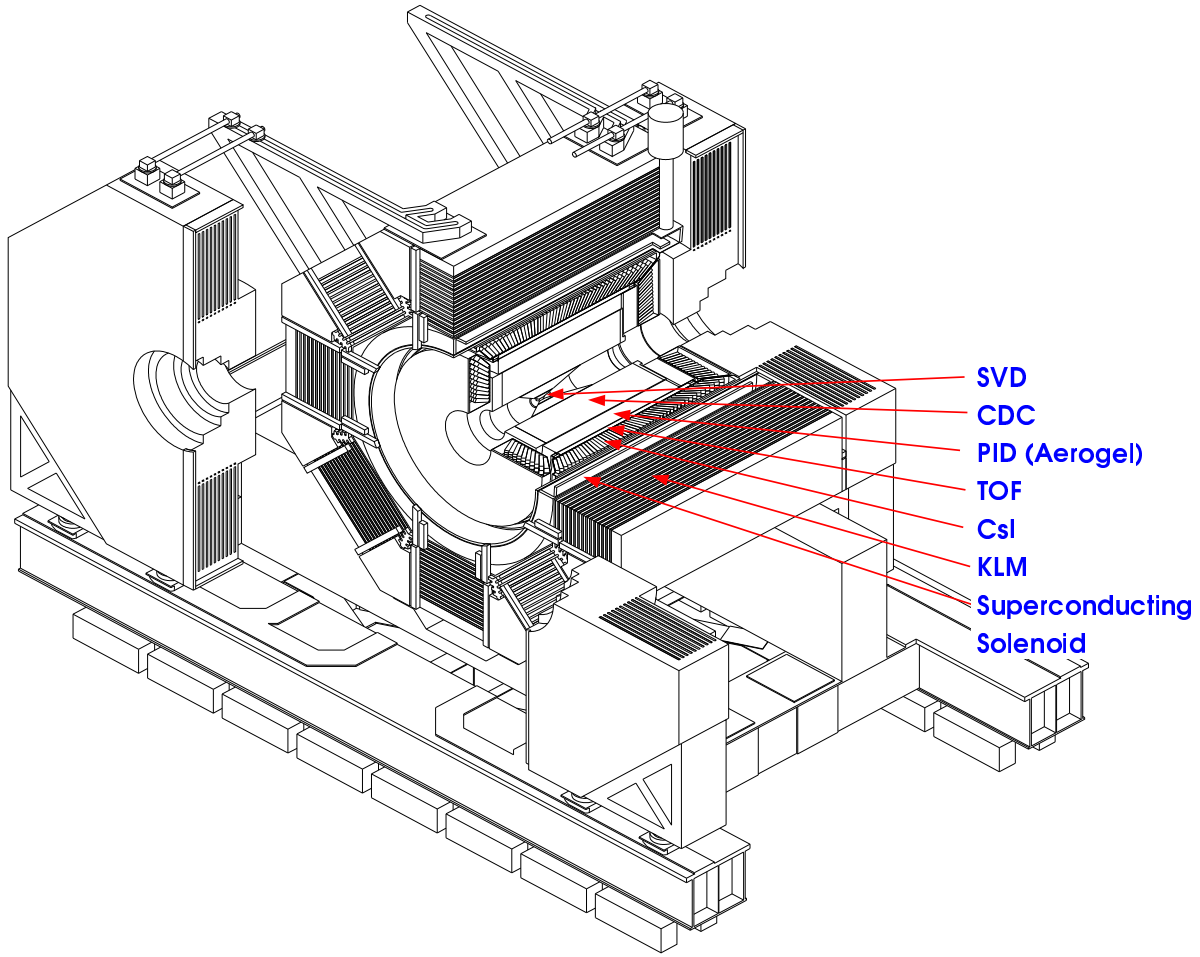

Figure 2.13: Schematic of BELLE detector.

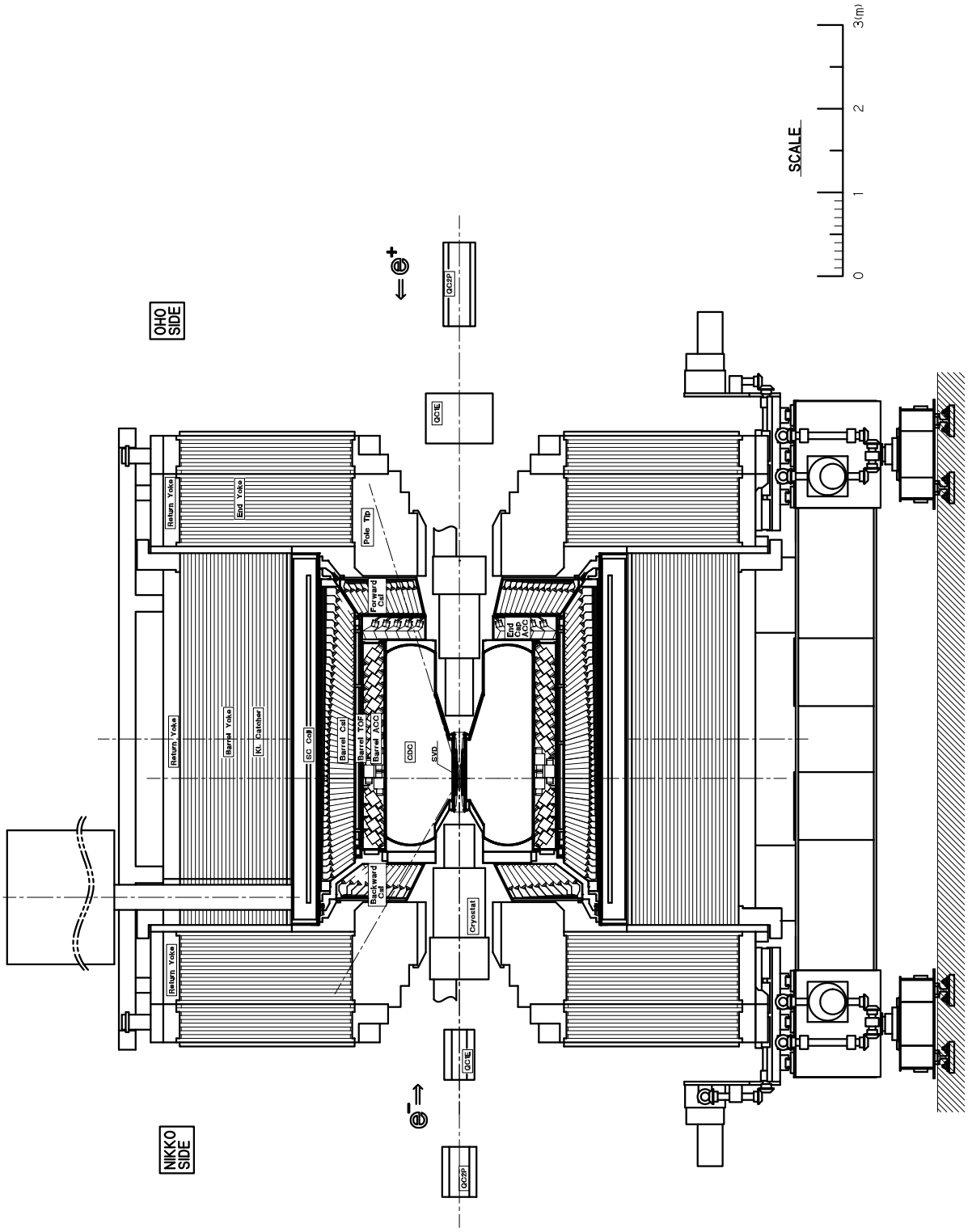

Figure 2.14: Side view of BELLE detector.

Table 2.2: Parameters of expected performance for individual detector components.

Detector	Type	Configuration	Readout	Performance
Beam pipe	Beryllium double-wall	Cylindrical, r=2.3 cm 0.5mm Be/2mm H_2O/0.5mm Be		Helium gas and Water cooled
SVD	Double Sided Si Strip	300 μm-thick, 3 layers r = 30.0 - 60.5 mm 23° $\leq \theta \leq$ 140°	 ϕ: 40960 z: 40960	$\sigma_{r\phi} \leq 10\mu$m σ_z=7-40μm $\sigma_{\Delta z} \sim 80$ μm
CDC	Small Cell Drift Chamber	Anode: 50 layers Cathode: 3 layers r = 8.5 - 88 cm 17° $\leq \theta \leq$ 150°	 A: 8.4 K C: 1.7 K	$\sigma_{r\phi}$ = 130 μm σ_z = 200 $\sim$ 1400μm σ_{p_t}/p_t =0.3%$\sqrt{p_t^2+1}$ $\sigma_{dE/dx}$ = 5.3%
ACC	$n \simeq 1.01$ Silica Aerogel	$\sim$12x12x12 cm^3 blocks 960 barrel/228 endcap FM-PMT readout	 < 2188	 $N_{p.e.} \geq 6$ K/π 1.3<p<3.6GeV/c
TOF	Scintillator	128 ϕ segmentation r = 120 cm, 2.5 m-long	128×2	σ_t = 100 ps K/π up to 1.2GeV/c
CsI	CsI(Tl) crystal	Towered structure $\sim$ 6x6x30 cm^3 crystals Barrel: r = 125 - 162 cm Endcap: z = -102 and +196 cm	 6624 1152(f) 960(b)	σ_E/E= 0.67%/$\sqrt{E}\oplus$1.8% σ_{pos}=0.5 cm/$\sqrt{E}$ E in GeV
MAGNET	super conducting	inn.rad. = 170 cm		B = 1.5 Tesla
KLM	Resistive Plate Counter	15(14)layers for Barrel(Endcap) (47mm Fe+44mm gap) two RPCs in each gap Barrel: z and ϕ strips Endcap: θ and ϕ strips	 21856 16128	$\Delta\phi$=$\Delta\theta$=30mr for K_L σ_t=a few ns 1% hadron fakes

2.3.1 Silicon Vertex Detector(SVD)

As mentioned above, the primary goal of this experiment is the measurement of asymmetry in the proper time distribution when one of the $B\overline{B}$ pair decays into a CP eigenstate. The proper time difference Δt is obtained from the distance between the decay vertices of the two B mesons along the beam direction, Δz, such that,

$$\Delta t \simeq \Delta z / c\beta\gamma, \tag{2.83}$$

where, $\beta\gamma$ is the Lorentz boost factor due to the asymmetric beam energies ($\beta\gamma = 0.42$ at BELLE). Since the typical decay distance for B mesons at BELLE experiment is 200 μm, better than 100 μm spatial resolution is required for the vertex detector. Multiple Coulomb scattering also affects the detector design. Vertex detection precision is made difficult by multiple Coulomb scattering in the beam pipe and the first layer of the vertex detector. Since the vertex resolution improves inversely with the distance to the first detection layer, the first detection layer has to be placed as close as possible to the beam pipe.

In order to satisfy these demands, double-sided silicon strip detectors(DSSDs) are adopted as the vertex detector elements. The DSSD is made of 300 μm thick n-type silicon bulk with strips orthogonal to each other on both sides of the substance. If a reverse bias is applied to the strips, the thickness of the depletion layer increases. When a charged particle traverses there, electron-hole pairs are produced. By picking up the signals at the strips, we can measure the position of the passing particle. Figure 2.15 shows the whole configuration of the SVD detector [15]. It is composed of 3 layers, each of which is located at 30.0 mm, 45.5 mm and 60.5 mm from the center of the beam pipe and consists of 8, 10, and 14 detector units. Front end VLSI chips are mounted on DSSDs at each end of the detector unit. SVD detector covers a polar angle of $23^\circ \leq \theta_{lab.} \leq 140^\circ$.

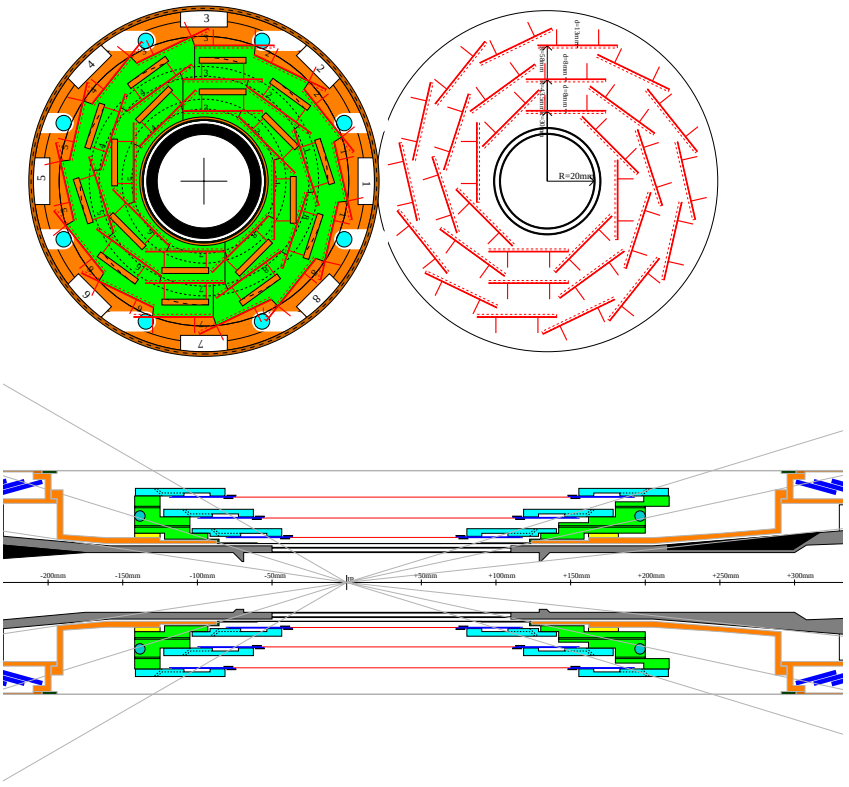

Figure 2.15: SVD detector configuration.

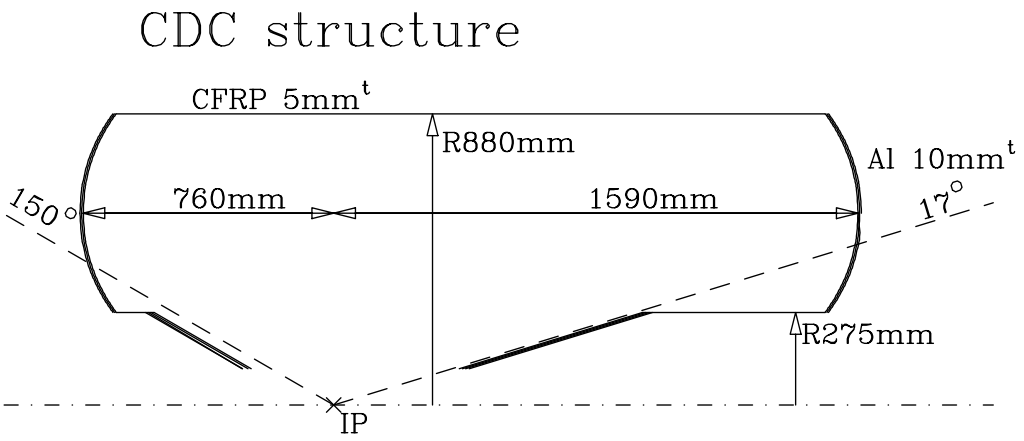

Figure 2.16: The structure of CDC.

2.3.2 Central Drift Chamber(CDC)

A drift chamber is used for the tracking of charged particles. It generally consists of a large number of wire electrodes and a gas container. The gas molecules are ionized by a charged particle passing through the detector. The liberated electrons drift toward the anode wires, then they are multiplied rapidly by a strong electric field near the wire. This signal is read out from the wire. We can determine the position of the passing particle with good resolution by measuring the drift time of the electrons.

The central drift chamber(CDC) provides charged particle tracking and measurements of the energy loss dE/dx for particle identification. Since the charged particle which are subjected to a magnetic field by the 1.5 Tesla solenoid coil follow a helical orbit, then from the bending radius of the charged particle track the momentum of the particle can be measured. In addition, the energy loss dE/dx of the particle through ionization depends on the relative velocity($\beta = v/c$). A measurement of the dE/dx enables therefore a determination of the particle velocity, and together with the momentum it is possible to identify the particle.

The CDC structure is shown in Figure 2.16. It is asymmetric in z for providing the $17° \leq \theta \leq 150°$ angular coverage. It consists of 3 cathode layers and 50 wire layers. There are two types of wire layers. One is an axial wire strung parallel to the beam axis, and the other is small-angle-stereo wire inclined by some angles against the beam axis in order to measure the z coordinate.

Considering low-Z gas importance both for minimizing multiple Coulomb scattering contributions to the momentum resolution and for reducing background from synchrotron radiation, a 50% helium -50% ethane gas mixture is selected for the CDC.

The CDC provides a spatial resolution $\sigma_{r\phi}$=120 μm, a momentum resolution better than $\sigma_{p_t}/p_t \sim 0.5\%\sqrt{p_t^2+1}$, and dE/dx resolution $\sim 5.3\%$.

2.3.3 Aerogel Čerenkov Counter(ACC)

Particle identification, especially the separation of $\pi^{\pm}$ and $K^{\pm}$ is indispensable for studying CP violation in the B system. The ACC is a threshold Čerenkov counter equipped with silica aerogels having a low refractive index and designed to achieve π/K separation more than 1.2 GeV/c momentum range. When a charged particle traverses a layer of material with refractive index n, and its velocity $v = \beta c$ exceeds the light velocity c/n in the material;

$$n > \frac{1}{\beta} = \sqrt{1 + \left(\frac{m}{p}\right)^2},$$

then Čerenkov light is emitted. Together with the momentum information of CDC, by checking if the Čerenkov is emitted or not, it is possible to identify the particle.

The ACC is divided into two parts: a barrel array and an endcap array. These are shown in Figure 2.17 and 2.18. The barrel ACC array consists of 960 modules: 16 modules in the z(θ) direction and 60 modules in azimuth. The refractive index for the barrel counters varies 1.010 to 1.028 with θ considering θ dependence of the hadron momentum spectrum. Čerenkov light from the aerogel radiators is detected using fine-mesh photomultiplier tubes(FMPMTs). The diameter of the FMPMT(2", 2.5" and 3") varies corresponding to difference in the index. The aerogel blocks are typically $12\times12\times12$ cm^3. One or two FMPMTs are attached to them. The endcap ACC consists of 228 modules. All of the endcap counters use $n = 1.03$ aerogel. A typical endcap counter is 12×12 cm^2 in cross section and 10 cm thick, and is viewed by a single 3"-FMPMT.

2.3.4 Trigger/Time of Fright Counter(TOF/TSC)

The TOF is a plastic scintillation counter and takes charge of π/K separation up to 1.2 GeV/c momentum range. The time of flight of a particle is given by, for a flight pass L,

$$T = \frac{L}{c}\sqrt{1 + \left(\frac{m}{p}\right)^2},$$

then the precise measurements of the time of flight together with the momentum information of CDC enable us to identify the particle.

The TOF/TSC system consists of 128 barrel TOF counters and 64 barrel TSC(Trigger Scintillation Counter) counters. Two trapezoidally shaped TOF counters and one TSC counter, with a 2 cm intervening radial gap, form one module. The arrangement of a

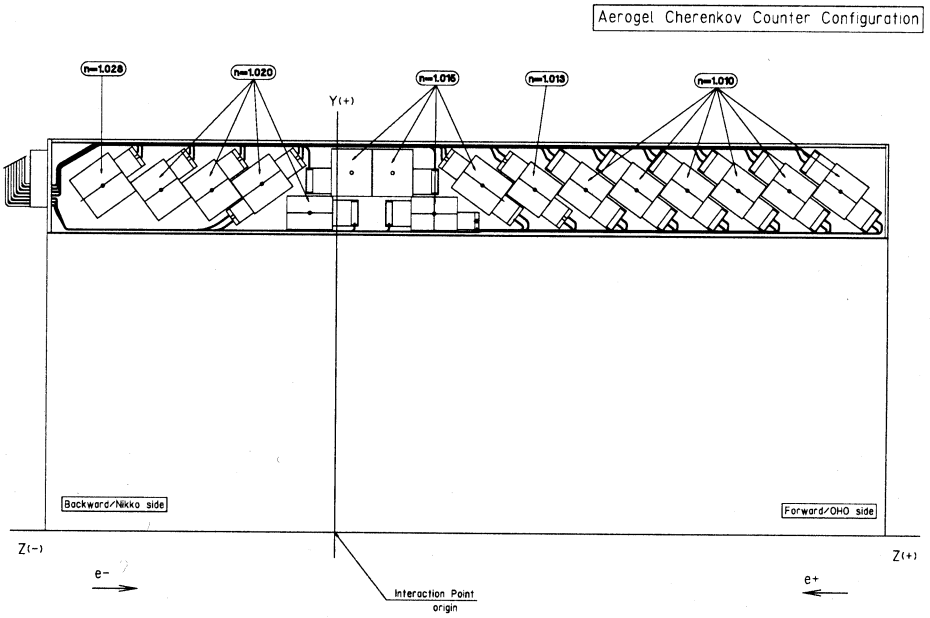

Figure 2.17: Schematic view of barrel ACC.

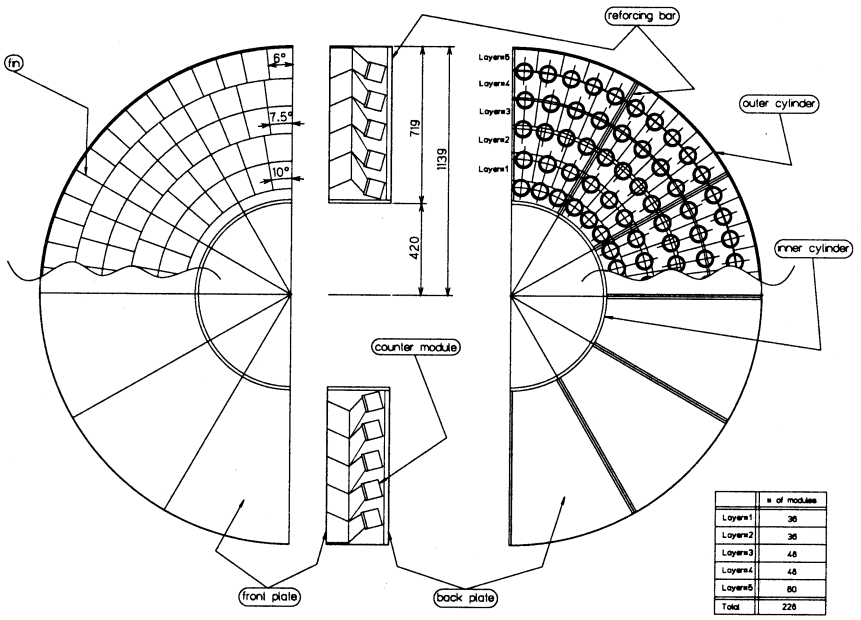

Figure 2.18: Schematic view of endcap ACC.

module is shown in Figure 2.19. Two 2"FMPMTs are mounted to the both ends of TOF counters and a single 2"FMPMT is mounted to TSC counters. These modules are individually mounted to the inner wall of the CsI container. The parameters for the TOF/TSC system is listed in Table 2.3.

This TOF system provides 3σ π/K separation up to 1.2 GeV/c with a TOF time resolution of 100 ps. A coincidence between TSC and TOF counters provides a clean event timing to the BELLE trigger system.

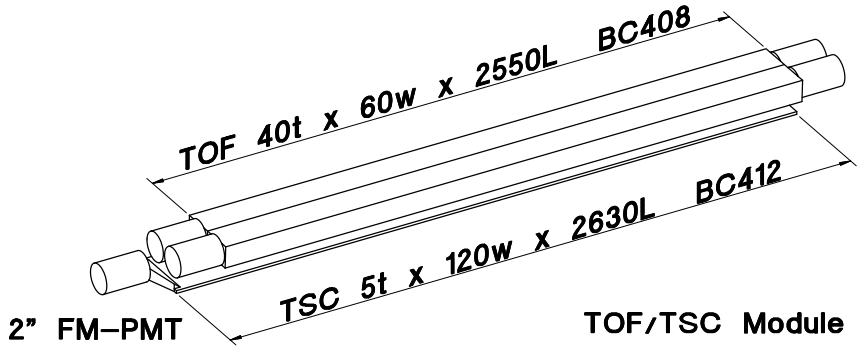

Figure 2.19: Schematic view of TOF/TSC module.

Table 2.3: Parameters of the TOF and TSC counters.

	Thickness(cm)	z(cm) coverage	r(cm)	ϕ segmentation	No.of PMT
TOF	4.0	-72.5,+182.5	122.0	128	2
TSC	0.5	-80.5,+182.5	117.5	64	1

2.3.5 Cesium Iodide Calorimeter(CsI)

The CsI is an electromagnetic calorimeter. Photons and electrons traversing a medium create electromagnetic showers. We can measure the energies by detecting these showers with the electromagnetic calorimeter.

The main purpose of the CsI calorimeter is the detection of photons with high efficiency and good resolution. Almost one-third of the particles produced from the B meson decays is a π^0, which decays into two photons, and most of these photons have relatively low energy. Thus sensitivity to low energy photons is very crucial. On the other hand,

important two-body decay modes such as $B \rightarrow K^*\gamma$ and $B^0 \rightarrow \pi^0\pi^0$ produce photons with energy up to 4 GeV. It is important to retain good resolution up to this energy.

Considering these requirements, CsI(Tl) crystals having features of high light output, short radiation length and good mechanical properties are used as the material for BELLE electromagnetic calorimeter. The overall configuration of the CsI is shown in Figure 2.20. The barrel calorimeter consists of 6624 CsI(Tl) elements, each being about 6×6 cm^2 in cross section and 30 cm (16.2 radiation length) in length. The endcap contains 2112 CsI(Tl) crystals. The CsI covers $17^\circ \leq \theta_{lab.} \leq 150^\circ$ region.

The CsI can provide energy resolution of 3% for 40 MeV and 1.6 % for 1.5 GeV photons [16].

2.3.6 K_L^0/μ Detector(KLM)

The KLM is the outermost detector located outside the superconducting solenoid and aims to detect K_L and muon which can not be detected at inner detectors. The KLM detector consists of a barrel part and two endcap parts. The structure of both parts is a repetition of 47 mm thick iron plates separated by 44 mm thick slots, into which resistive plate counter(RPC) modules are placed. The iron plates serves as an absorber material for K_L and muon detection and also as the flux return for the solenoid's magnetic field. There are 15 slots in the barrel and 14 in the endcaps. The barrel is divided azimuthally into octants and the endcaps are divided into quadrants.

For K_L detection, we use the hadronic shower created by K_L meson's interactions in the CsI, the coil, or the iron plate. Muons are distinguished from charged pions by their aligned and deep hit patterns in the KLM compared with pions' broad and shallow patterns.

The details on the KLM detector is described in the following chapter.

2.3.7 Extreme Forward Calorimeter(EFC)

The purpose of the extreme forward calorimeter(EFC) located at very small angles is to detect the particles which are out of the BELLE detector acceptance, $17^\circ \leq \theta_{lab.} \leq 150^\circ$, and to monitor the luminosity. In e^+e^- machines the luminosity is determined by measuring a well-known QED process such as $e^+e^- \rightarrow e^-e^+$(Bhabha scattering) or $e^+e^- \rightarrow$

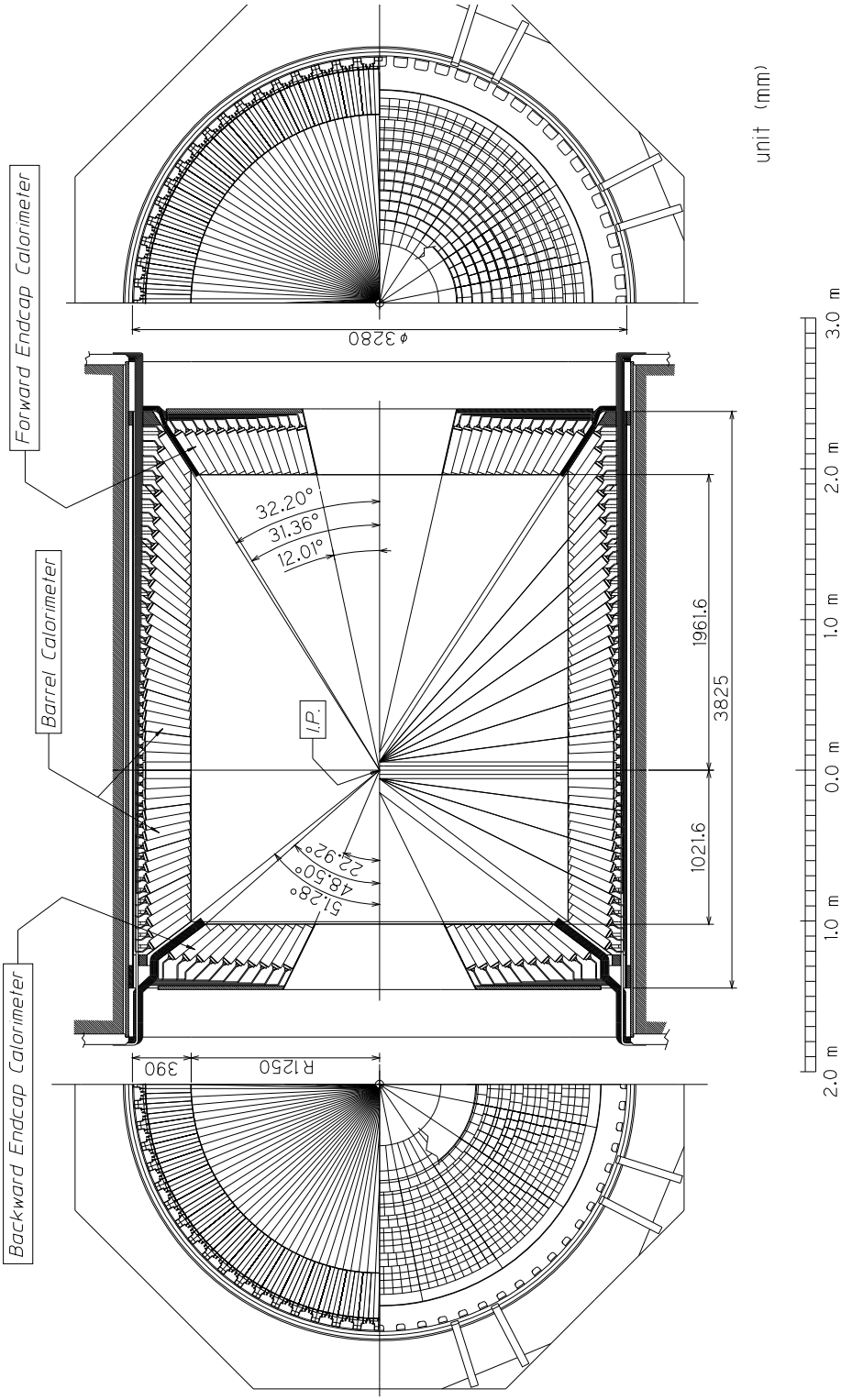

Figure 2.20: The overall configuration of CsI.

$e^+e^-\mu^+\mu^-$. Since the event rates of these processes are high with a small angle detector, it is possible to measure Luminosity with good precision at the EFC.

BGO crystals are used as an active medium for the electromagnetic showers. The principle of BGO is similar to that of CsI(Tl). The resultant scintillation light is collected by photodiodes. The crystals are divided into 5 segments in θ and 32 in ϕ. 320 crystals are used in total.

Chapter 3

K_L^0/μ Detector (KLM)

3.1 Physics Requirements

The KLM subsystem is designed to detect K_L^0 mesons and muons with high acceptance, efficiency, and purity [13].

Since K_L^0 mesons are neutral and have a long life time of $c\tau \sim 15.5$ m, they can not be detected at inner detectors. The KLM detector identifies K_L^0 by making use of its hadronic interactions in the CsI calorimeter, the coil, or the KLM itself. Detection of K_L^0 is essential for the mode $B^0 \to J/\psi K_L^0$ whereby we can measure the angle ϕ_1 of the unitarity triangle (see section 2.1.5). We measure the position of the K_L^0 meson's interactions, thus the momentum direction, and the K_L^0 direction measurement alone is sufficient for searching for $B^0 \to J/\psi K_L^0$ since the K_L^0 momentum can be calculated from the kinematic constraints if the direction is known with better than 30 mrad angular resolution.

The KLM detector also identifies muons with high efficiency and purity over a broad momentum range. Muons are used in the CP violation measurements to identify the flavor of the tagging B meson through its semileptonic decay, and to reconstruct $J/\psi \to \mu^+\mu^-$. They are also important for the studies of rare B decays. Distinction from charged pions is important for muon identification. While charged pions are attenuated by strong interactions in the CsI calorimeter and the absorbing material of the KLM, muons travel further into the KLM and leave much cleaner and straighter tracks. In actual analysis, muons are reconstructed by matching the track measured in the KLM with the extrapolation of

the track in the CDC.

To satisfy these requirements, we adopted position-sampling designs, in which thin detector planes and absorber plates alternate to form a multi-layer sandwich. Hence, to be thin is required for the detector layers. Since the KLM is the outermost detector, it should cover large area. And furthermore, when it comes to multi-layer structure, a large number of detectors are needed, thus the detector layers should be low cost, simple and robust for easiness of fabrication. Considering the BELLE experiment is planning to be performed over a period of ten years, long term durability together with high detection efficiency is also required.

The KEKB is a lepton collider and the event rate is not so high and estimated to be about 200 Hz. The event rate concerning KLM is expected to be lower than the rate of cosmic ray ($\sim$ 0.01 Hz/cm^2), thus high rate capability is not necessarily required for the detector layers.

A simulation study taking account of multiple scattering of K_L^0 in the substance shows that 5 cm spatial resolution corresponding to 30 mrad angular resolution is sufficient for K_L^0 detection [17]. Although the multiple scattering of muon is less than K_L^0, 5 cm spatial resolution is considered to be sufficient also for muon identification if the hits in multi-layer are combined.

In view of these requirements, the KLM structure was settled as described in the following section.

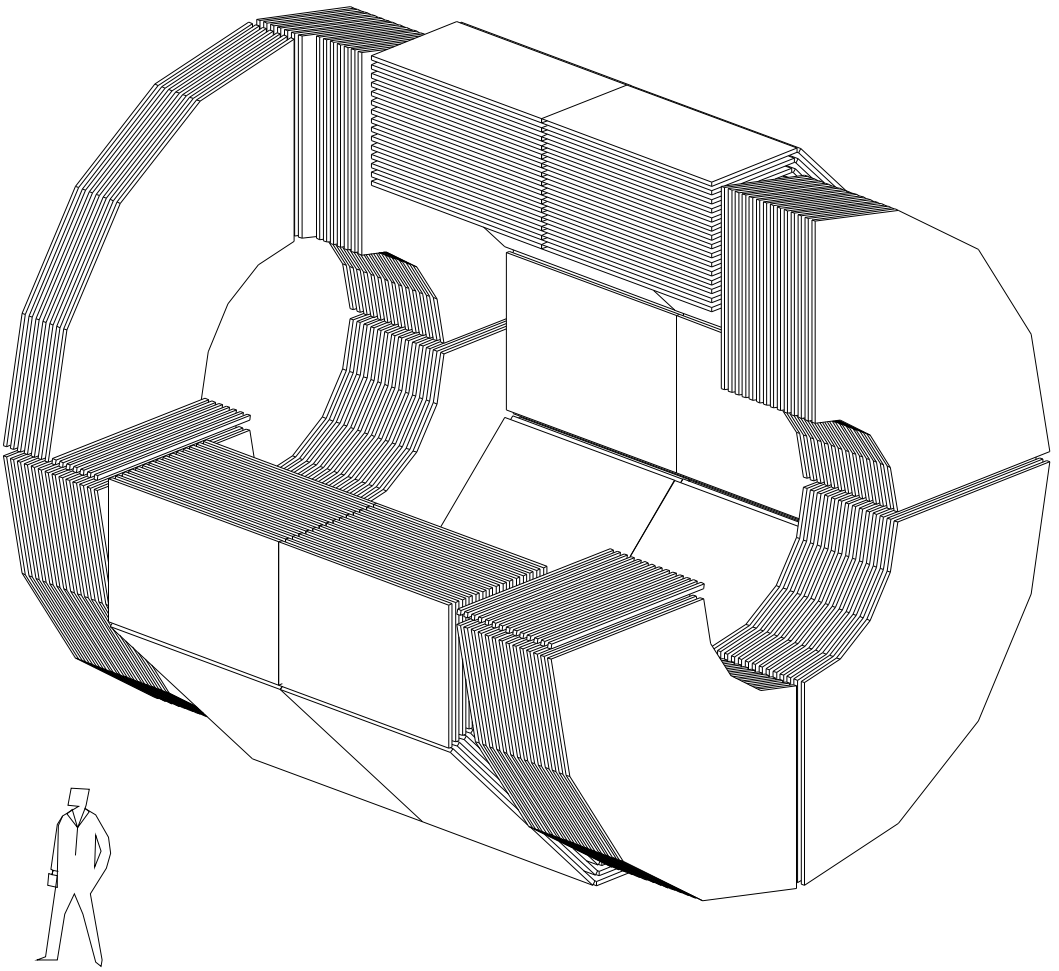

Figure 3.1: Schematic view of KLM detector.

3.2 Structure

Figure 3.1 shows a schematic view of KLM detector. The KLM detector consists of a cylindrical barrel part and two endcap parts. The barrel is divided azimuthally into octants and the endcaps are divided into quadrants. The structure of both parts is a repetition of 47 mm thick iron plates separated by 44 mm thick slots for the detectors. In addition to serving as an absorber material for K_L and muon detection, the iron plates serve as the flux return for the solenoid's magnetic field. There are 15 slots in the barrel and 14 in the endcaps. The area covered by the detector layers amount to about 1800 m^2.

RPCs (Resistive Plate Counters) were chosen as the detector for the KLM due to their good time and spatial resolution, inherent simplicity - with no internal wire - and low cost. An RPC is a charged particle detector utilizing a constant and uniform electric

field produced by two parallel electrode plates made of a material with high bulk resistivity. When a charged particle traverses the active volume and ionizes the gas between the plates, a discharge occurs. The area affected by the discharge is limited by the high resistivity of the plates. Further details on RPCs are described in chapter 4. A characteristic of the BELLE RPC is using a float glass with the volume resistivity of $10^{12} - 10^{13}$ Ω·cm as its resistive electrode. Glass was selected because of its ready availability (standard soda-lime float glass used in household windows is employed) and its inherent stability. The two glass electrodes are separated by 2 mm Noryl spacers with high resistivity.

RPC modules are placed into the 44 mm thick slots. Each RPC module has a superlayer design containing two independent RPC layers (inner and outer). The barrel modules contain two RPCs with about 220 cm in length and between 151 cm (at innermost layers) and 267 cm (at outermost layers) in width. There are a total of 240 modules and 480 RPCs in the barrel. On the other hand, the endcap modules are shaped as quarter disks as shown in Figure 3.2, and each superlayer quadrant contains ten wedge-shaped RPCs (see Figure 3.4) arranged in two layers of five wedges each. The two layers in each endcap module are arranged to stagger each other to reduce overlapping of the insensitive regions due to edge spacers. There are a total of 112 modules and 1120 RPCs in the endcap.

The readout for each superlayer consists of sets of orthogonal strips. In the barrel region these strips provide two-dimensional position measurements of ϕ and z (straight ϕ and z strips), whereas for the endcap the strips are oriented so as to provide r and ϕ measurements (quarter-circular θ and radial ϕ strips, see Figure 3.3). Since the spatial resolution required for the KLM is about 5 cm, the natural strip width for the KLM is about 5 cm. The practical strip widths were chosen to match the modularity of the readout electronics (groups of 12). To this end, there are 48 z and either 36 (inner 6 superlayers) or 48 (outer 9 superlayers) ϕ strips for each barrel module, and 48 θ and 96 ϕ strips for each endcap module. There are a total of 37,984 readout strips. For the barrel the width of pickup strips is 4.5 cm in z and between 4.3 cm and 5.5 cm in ϕ, while for the endcap the width of each quarter-circular θ strips is 3.6 cm and the width of radial ϕ strips varies from 1.86 cm at the inner radius to 4.76 cm at the outer radius.

Figure 3.5 illustrates a superlayer structure of the RPC module. A high voltage (HV)

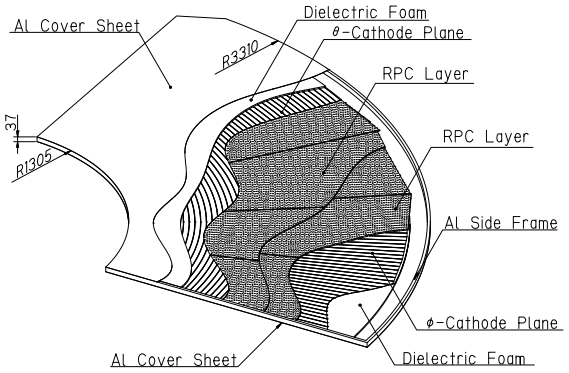

Figure 3.2: Cutaway view of Endcap KLM module.

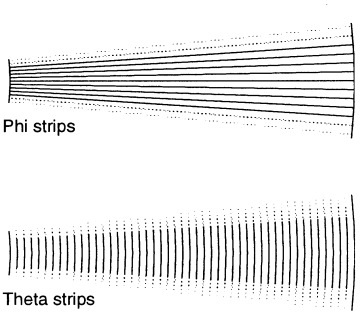

Figure 3.3: Readout strips for Endcap KLM module.

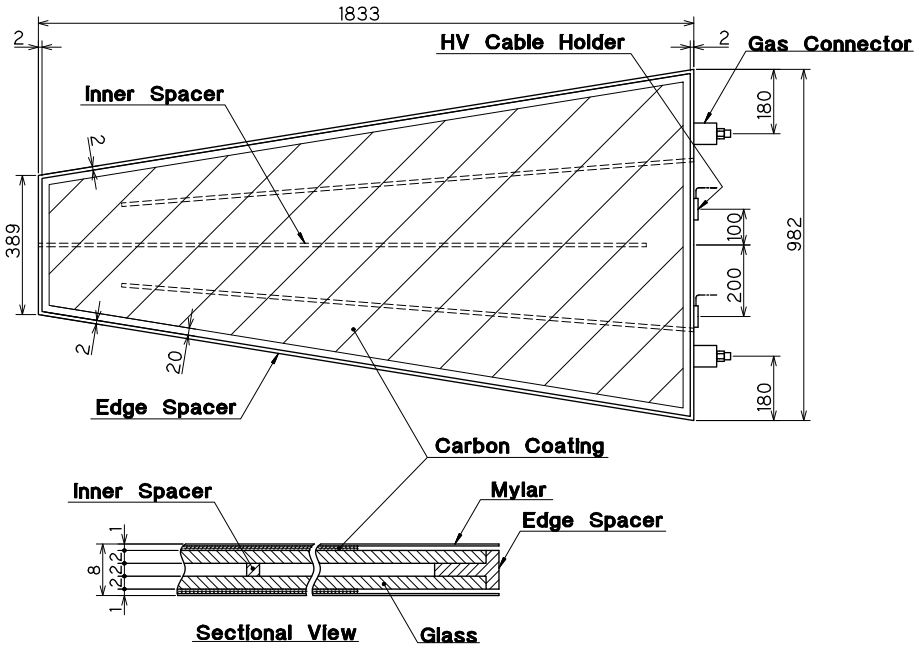

Figure 3.4: Schematic view of endcap RPC.

is supplied to the same direction so as to pick up signal from both readout planes even if either RPC in a superlayer fires. Thus if the single-layer inefficiency is η, the inefficiency for the superlayer will be η^2. Typically $\eta \simeq 10\%$.

3.3 Endcap KLM Performance with Cosmic rays

The installed endcap modules have been tested by using cosmic rays. In this section, we summarize the obtained results. The details of the test are reported in [18] and [19]. The gas mixture we have used are a mixture of 32% argon, 8% butane-silver (iso-butane:normal butane = 3:7) and 60% Freon 134a (HFC134a), which is nonflammable (see chapter 5).

- **Efficiency**

The module efficiency was measured by using cosmic-ray tracks triggered. The efficiency plateaus of a typical module for single-layer (inner and outer) and superlayer are shown in Figure 3.6. The efficiencies of each single-layer are more than 90% at 8 kV. The efficiency for the superlayer reaches above 98%.

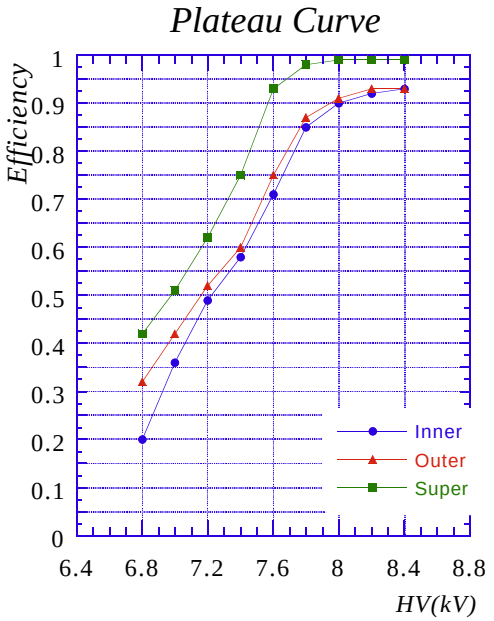

Figure 3.6: Efficiency vs high voltage for inner, outer, and superlayer.

- **Track resolution**

Figure 3.7 shows an example of reconstructed track of cosmic ray. When a cosmic ray traverses an RPC, the streamer in the gas gap induces signals on the strips in a region of a few millimeters wide. Sloping particle tracks broaden this charge distribution, thus a signal can be induced on more than one strip. Figure 3.9 and Figure 3.9 show the

residual distributions of x and y directions respectively for a typical module. The spatial resolution is 1.2 cm in x and 1.1 cm in y. These values are comparable to the design value.

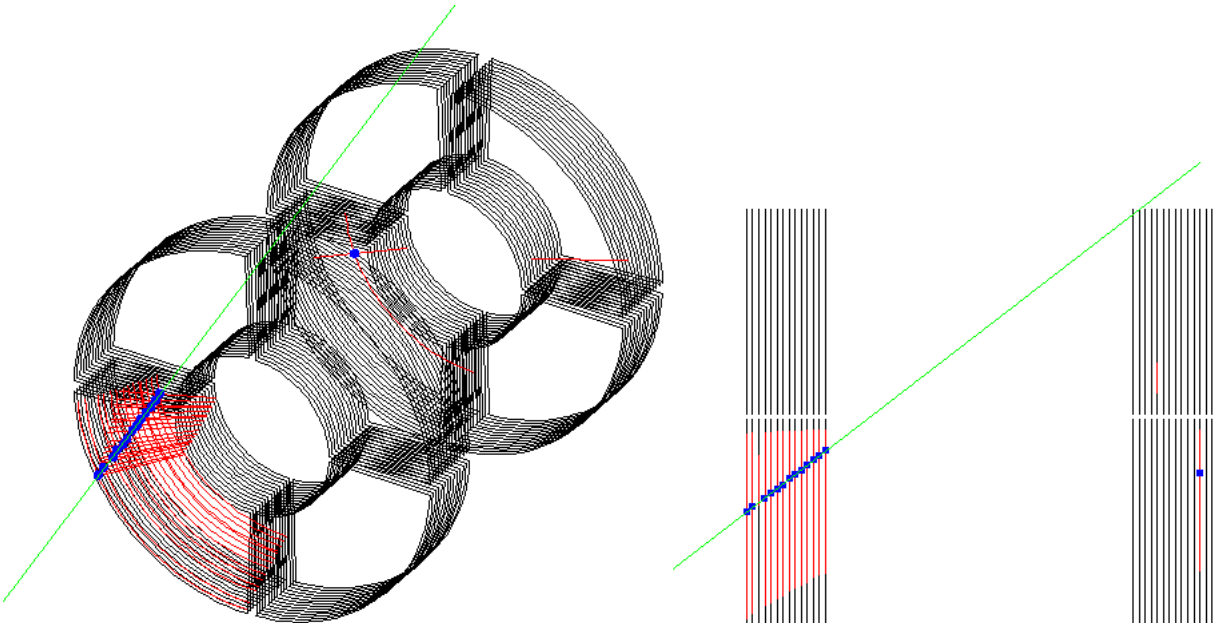

Figure 3.7: Reconstructed cosmic-ray track in the endcap KLM.

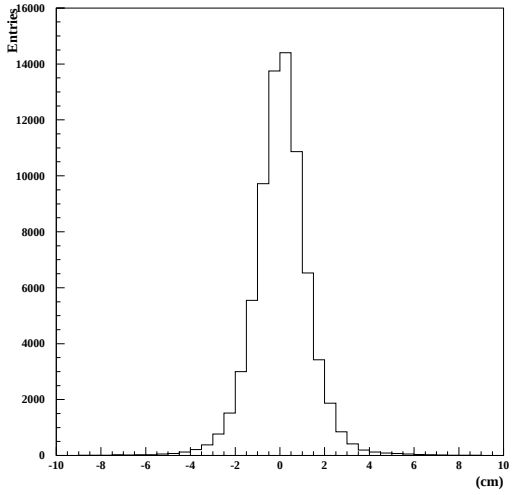

Figure 3.8: Residual distribution for x directions.

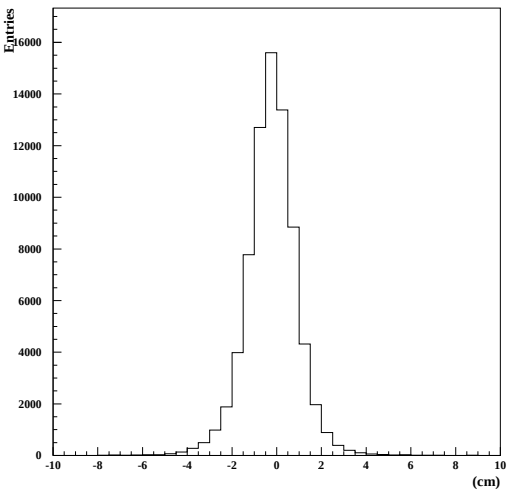

Figure 3.9: Residual distribution for y directions.

Chapter 4

Resistive Plate Counter (RPC)

4.1 Historical overview

RPCs(Resistive Plate Counters) which are kinds of parallel-plate counters utilizing gas multiplication induced in the uniform electric field generated by two parallel electrode plates were developed by Santonico *et al.* in the early 1980s [20].

RPCs were derived from Keuffel spark counters and Pestov spark counters. The characteristics of each counter are presented below.

• Keuffel's Parallel-Plate Counter

Wire chambers such as the Geiger-Muller counter produce the electric field decreasing as 1/r around the wire, wherein liberated electrons drift toward the wire and only very close to the wire the field gets strong enough to allow gas multiplication. The jitter of the electrons drift motion up to the multiplication region near the wire makes time resolutions modest such as about 0.1 μsec for the Geiger-Muller counter.

In order to overcome this modest time resolution, Keuffel developed a parallel-plate counter shown in Figure 4.1 in the 1940s [21]. He employed the parallel-plate geometry where the field was uniform and strong sufficient to multiply an electron avalanche. The counter consisted of rectangular sheets of copper or copper-plated steel spaced 2.5 mm and 35 cm^2 in area. They were located within a glass envelope to which a gas mixture of argon and ethylene was confined with a total pressure of 1/2 atmosphere. Since the space-charge geometry, unlike the Geiger-Muller counter, was not such that the discharge

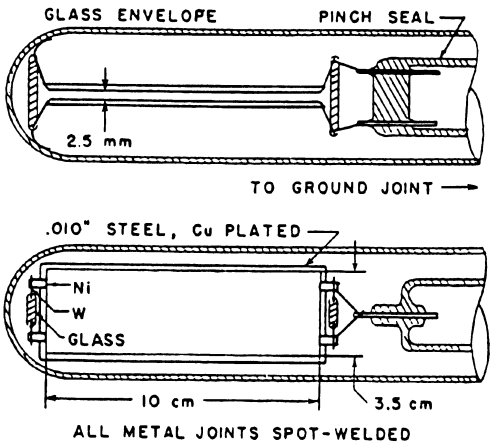

Figure 4.1: Keuffel's Parallel-Plate Counter.

was self-quenching in the parallel-plate counter, once the discharge occurred, it continued so long as the high voltage was applied. Thus an external electronic quenching circuit which let the high voltage down for a duration ($0.01 \sim 0.05$ sec) after the discharge was used for "cooling off" the counter.

The parallel-plate counter provided about 90% efficiency and the order of 10 nsec time resolution, and the position resolution was determined by the area of the counter itself since the discharge spread over the whole active region. The amplitude of the pulse from the parallel-plate counter was several hundred volts. There were several problems. First, they were not capable of high counting rates because of the quenching duration ($0.01 \sim 0.05$ sec). Second, there were technical difficulties in constructing the counter such as the processing of the plate surface and the installation into the glass tube with the two plates kept parallel rigidly. Third, the lifetime of the counter were restricted to one or two months due to the occurrence of "spot burst" causing continuous discharges on the surface of the cathode plate.

• Pestov's Planer Spark Counter

In the 1970s, Pestov *et al.* developed a planer spark counter with a high counting rate and a large area [22]. Figure 4.2 shows a schematic view of the planer spark counter. It was composed of a semiconducting glass with high resistivity as the anode electrode and a copper-coated glass as the cathode. The gap spacing between the electrodes was

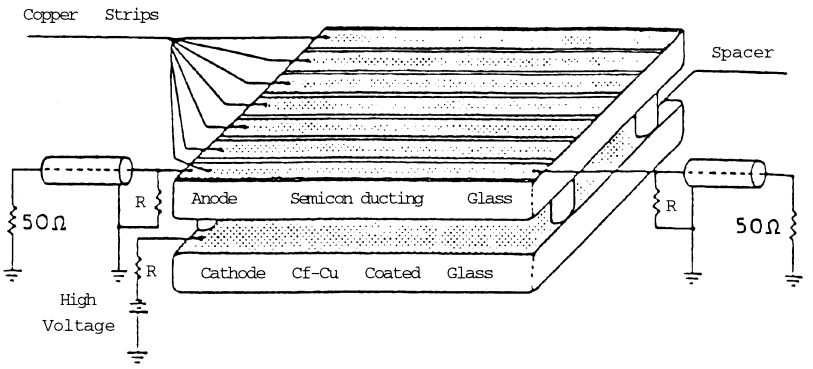

Figure 4.2: Pestov's Planer Spark Counter.

kept 100 μm - 200 μm, where a gas mixture containing quenching agents such as iso-butane and ethylene which quenched spurious discharges due to photon absorption was circulated with a pressure of about 10 atmospheres. The discharges initiated in the gas by the passage of charged particles were localized by the high resistivity of the electrode and the quenching characteristics of the gas. The signals were read out from the copper strips fixed on the outer surface of the anode.

This counter offered a fine time resolution up to 30 ps together with high detection efficiency and have used as TOF counters. Its application, however, is limited by the complexity in using the high gas pressure, the high requirements of mechanical precision to keep the gas gap 100 μm - 200 μm, and the expensiveness of the semiconducting glasses.

• Santonico's Resistive Plate Counter

In the 1980s, Santonico *et al.* developed a resistive plate counter (RPC) whose electrodes were made of Bakelites with a bulk resistivity of the order of 10^{10-12} Ω·cm and spaced by 1.5 mm - 2 mm between which a gas mixture of argon, butane and Freon at normal pressure was circulated (Figure 4.3). The simplifications introduced into the RPC such as the absence of high pressure, the low requirements of mechanical precision and the low cost make it applicable to several cosmic ray and accelerator experiments as muon detector (MINI[23], E771[24], L3[25] and so on).

The characteristics of the RPC are as follows.

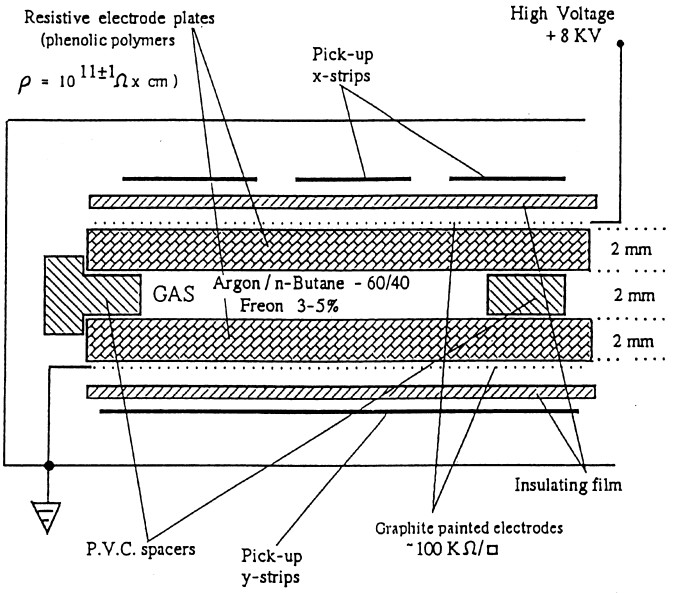

Figure 4.3: Santonico's Resistive Plate Counter.

- Large amplitude of the signal ($\sim$ 100 mV) - no need to use amplifiers.
- Good time resolution (a few nsec).
- Simple and robust design - easiness of the production even in large dimensions.
- Low cost.

4.2 Principles of Operation

Figure 4.4 outlines the principle of operation of the RPC. If a high voltage is applied to the resistive electrodes, a uniform electric field (usually 4 - 4.5 kV/mm) is generated between the electrodes. When a charged particle traverses there, primary ion pairs are produced along its trajectory. The number of primary ion pairs follows Poisson-like statistics and is estimated to be 5 - 10 on average for the RPC with 2 mm gap spacing at normal gas pressure, given minimum ionizing particles [26].

The liberated electrons are accelerated by the electric field and initiate an avalanche. The total number of ions at the time t after the gas ionization is given in the form,

$$N(t) = N_0 \exp(\alpha v t), \tag{4.1}$$

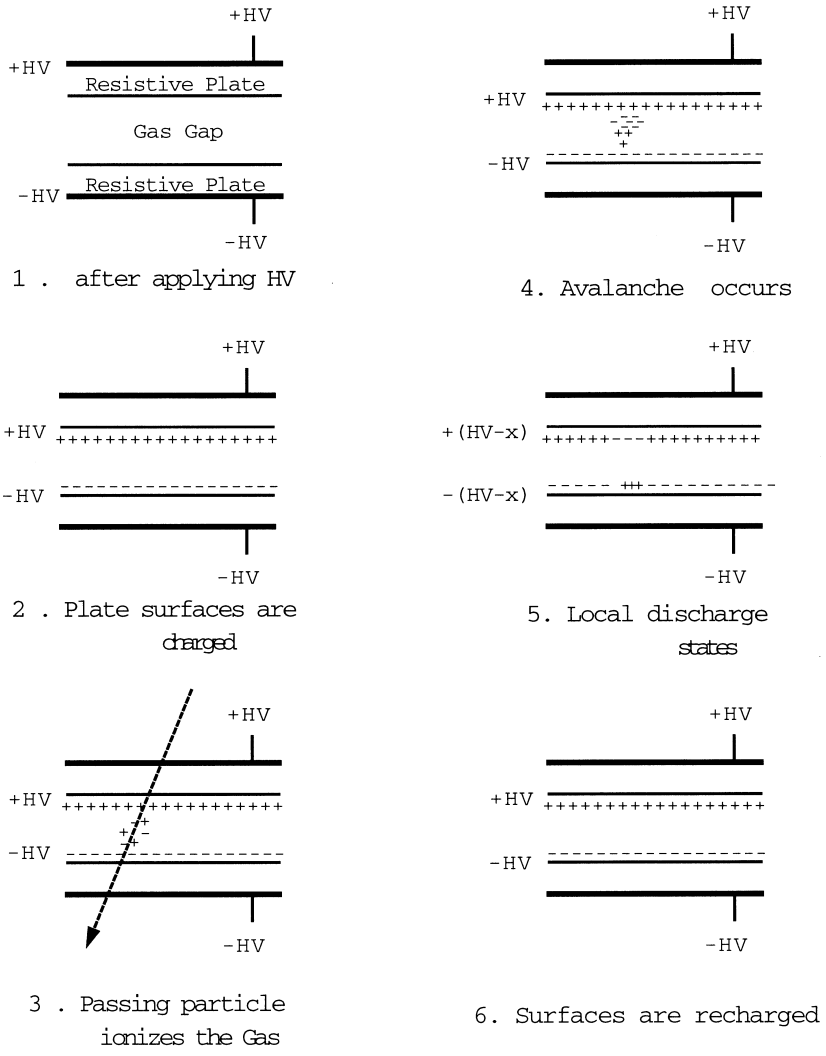

Figure 4.4: Principles of Operation of RPC.

where N_0 is the number of primary ion pairs, α is the first Townsend coefficient, and v is the drift velocity of electrons. When the gas multiplication $M = N/N_0$ exceeds the Raether condition: $M \sim 10^8$ [26], the avalanche develops into a streamer, then a discharge occurs.

This discharge, however, is prevented from spreading over the whole gas volume, firstly because, due to the high resistivity of the electrodes, the electric field is suddenly switched off in a limited region around the point where the discharge occurred, and secondly because butane and Freon quench the discharge by photon absorption and electron capture respectively, which will be explained in section 5.2.

Since under the uniform electric field, the sequence of transitions: free electron →

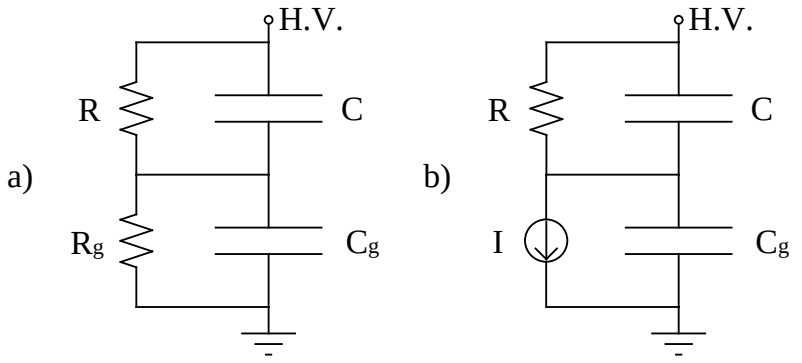

Figure 4.5: Equivalent circuit of the discharge cell.

avalanche → streamer, can occur in a very short time and with minimal fluctuations, a better time resolution is achievable compared with wire chambers. For the streamer signal, however, the equation (4.1) does not hold any longer and the total charge obtained is not proportional to the number of primary ion pairs, so that the RPC can not measure the energy loss of the passing particles.

Since the discharges are, as described above, localized in a limited region, RPC can be regarded as the set of a large number of small "discharge cells" [27]. Figure 4.5 illustrates the equivalent circuit of the "discharge cell". The capacitors C and C_g correspond to the resistive plates and the gas gap respectively and so do the the resistance R and R_g. For a non-ionized gas (Figure 4.5 a), $R_g = \infty$ and the supplied voltage is entirely applied to the gas gap. When the gas is crossed by a ionizing particle, the electric discharge generated in the gas can be represented by a current generator (Figure 4.5 b) which discharges the "gas capacitor" C_g so that the voltage initially applied to the gas is transferred to the resistive plate. After that, C_g is recharged and the system goes back to the initial condition (Figure 4.5 a).

The time duration needed for recharging the resistive plates is given by

$$\tau = R(C + C_g) = \rho\epsilon_0 \left(\epsilon_\tau + \frac{2d}{g}\right), \tag{4.2}$$

where, ρ is the bulk resistivity of the electrodes, ϵ_0 and ϵ_r are the vacuum and the relative dielectric constant respectively, d is the thickness of the plates, and g is the gas gap. If $\rho = 10^{12}$ Ω·cm (glass electrode), we have $\tau \sim 1$ sec. This relaxation time is considerably long compared with the duration of the discharge which is typically ∼10 nsec for the RPCs. The large difference between these two characteristic times insures that during

the discharge the electrode plates behave like insulators so that only a limited area around the discharge point remains inactive for a dead time of the order of τ.

The area of the discharge cell is proportional to the total charge Q fed in the gas such as

$$S = \frac{Qg}{\epsilon_0 V}, \tag{4.3}$$

where V is the difference of electric potential between the electrodes. Given $d = 2$ mm, $V = 8$ kV, and $Q = 100$ pC (see Figure 5.13), we have $S \simeq 3$ mm^2.

From (4.2) and (4.3), inefficiency of the detector is approximated to be

$$\eta_{loss} \sim r\tau S = \frac{rQ\rho}{V}(g\epsilon_r + 2d), \tag{4.4}$$

where r is the rate of incoming particle flux. The rate capability is an important issue for the RPC. The Q is a crucial parameter in determining the rate capability of an RPC. The discharge occurring in the gas indeed can only be fed by a limited current that can flow across a pair of electrode plates with high resistivity. A small value of Q allows therefore to keep the relaxation time short so that the detection efficiency stands high, even in presence of intense flux of ionizing particles. From this point of view, there have been several attempts to operate RPC not in streamer mode but in avalanche mode in which the obtained charge is drastically reduced to a few pC due to low gas gain, and high rate capabilities have been demonstrated [28]. We do not go into details on the avalanche operation here.

As known from (4.4), too high resistivity of the electrodes also causes inefficiency. Resistivity appropriate for the electrodes of the RPC is considered to be $\rho = 10^{10} - 10^{13}$ Ω·cm.

4.3 Signal readout

The signal from the RPC are picked up by either strips or pads that are located on the outside surface of the RPC. The electrode are coated with thin graphite layers (see Figure 4.3) or carbon layers through which high voltage is supplied. Due to their high surface resistivity, they are transparent to the electrical discharges generated inside the gas. This allows a capacitive readout through external pickup electrodes.

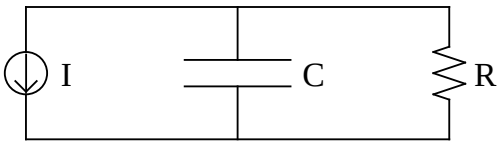

Figure 4.6: Equivalent circuit of the readout electrode.

The signals can be read out both from the anode (negative pulse) and the cathode (positive pulse) electrode sides. If two sets of strips are located in different directions (for example, orthogonal X and Y) on the each surface of the RPC, it is possible to measure the position of passing charged particles.

The strips behave as signal transmission lines of well defined impedance, which make it possible to transmit the signals at large distance with minimal loss of amplitude and time information. Impedance matching of pickup strips with the signal cable is achieved by adjusting the distance between the strip plane and the ground plane located outside the strip plane.

Figure 4.6 shows the equivalent circuit of the readout electrode [27]. C represents the electrode capacity and R the resistance connecting the electrode to ground. In the case of using strips as the readout electrodes, the capacity C is independent from the strip length since the strips can be regarded as signal transmission lines. It depends on the charge spread which is thought to be of the order of 1 cm^2. Then C is typically $\sim$1 pC. When the characteristic impedance of the line is 100 Ω, since the signal propagates in both directions along the strip with R $\sim$ 50 Ω, the time constant RC is therefore of the order of 50 psec which is much shorter than the rise time of the signal ($\sim$10 nsec).

On the contrary, the pad can be treated as a capacitor so that C depends on the area of the pad. For a large pad, time constant RC could be much longer than the signal duration. In this case, the output signal would be strongly integrated with a reduced amplitude following V = Q/C and a long exponential fall time. Furthermore, the larger the pad becomes, the more noises are likely to be picked up. Thus the pad size cannot be arbitrarily large. We have used a 25 $\times$ 25 cm^2 pad connected to a cable with 50 Ω characteristic impedance for the studies discussed in the following chapters. In this case, the time constant RC is estimated to be of the order of 10 nsec which is comparable to the signal duration.

Chapter 5

Study of Nonflammable Gas Mixture

5.1 Introduction

We have been using the gas mixture of 25% argon, 25% butane, and 50% HFC-134a(Freon) for testing glass RPCs. We call it standard gas [29]. The standard gas with such butane fraction is classified to be flammable. It is better to use a nonflammable gas mixture for safety or for avoiding complicated procedures that are required for handling flammable gases. However, decreasing the ratio of butane (this means the gas mixture is becoming nonflammable) which is expected to prevent the secondary discharges by absorbing ultraviolet photons might affect the RPC performance. We tested nonflammable gas mixture as well as standard gas by using small (30×30 cm^2) RPCs and compared the counter performance between them.

5.2 Gas Mixture

As the gas for the RPC, we use three kinds of gases, argon, butane and Freon(HFC-134a). Their behaviors in the RPC are as follows.

- **Argon (Ar)**

Argon is mainly ionized by incoming charged particles. The liberated electrons are multiplied by an electric field to form an avalanche and a subsequent streamer.

• **Butane (C_4H_{10})**

In the process of gas multiplication, recombinations between positive ions and electrons occur and ultraviolet(UV) photons which lead to the secondary ionizations are emitted. In such case, the discharges may spread over rather broad region so that we cannot determine the location of the initial discharge with some accuracy. Butane reduces the secondary discharges by absorbing UV photons in the wavelength region covering argon spectrums.

We are using butane-silver which is a mixture of 70% normal-butane and 30% iso-butane. Although we had used pure iso-butane that is much more expensive than butane-silver, it was verified that iso-butane and butane-silver show similar performance [31]. In the following, butane means butane-silver.

• **Freon,HFC-134a (CH_2FCF_3)**

Freon has high electron affinity (electro-negative) and keeps the streamer from spreading transversely due to electron capture.

The gas mixtures we have tested were twenty combinations of butane and argon concentration listed in Table 5.1, and no butane and no argon gas mixtures as well. Whether the mixed gas is flammable or nonflammable depends on the ratio of butane. Figure 5.1 illustrates the flammable regions of butane and air when mixed with various proportion of nitrogen and carbon dioxide [32]. Although this figure does not directly apply to the present case in which a mixture of argon and Freon is used as inert gas, a fact that butane is less flammable when surrounded by carbone dioxide compared to a case when it is surrounded by nitrogen indicates that the limits of inflammability of a gas mixture depends on the heat capacity of inert gas in the mixture. As a consequence of the calculations of heat capacities of inert gas, the gas containing 12% butane is estimated to be on the limit between flammable and nonflammable [30]. The gas with more than 12% butane is considered to be flammable and less than 12% butane to be nonflammable.

Table 5.1: Twenty combinations of the tested gas mixture.

Butane	Argon	HFC-134a(Freon)
4%	20%	
8%	25%	25 $\sim$ 76%
12%	30%	adjusted to 100%
25%	35%	in total
	50%	

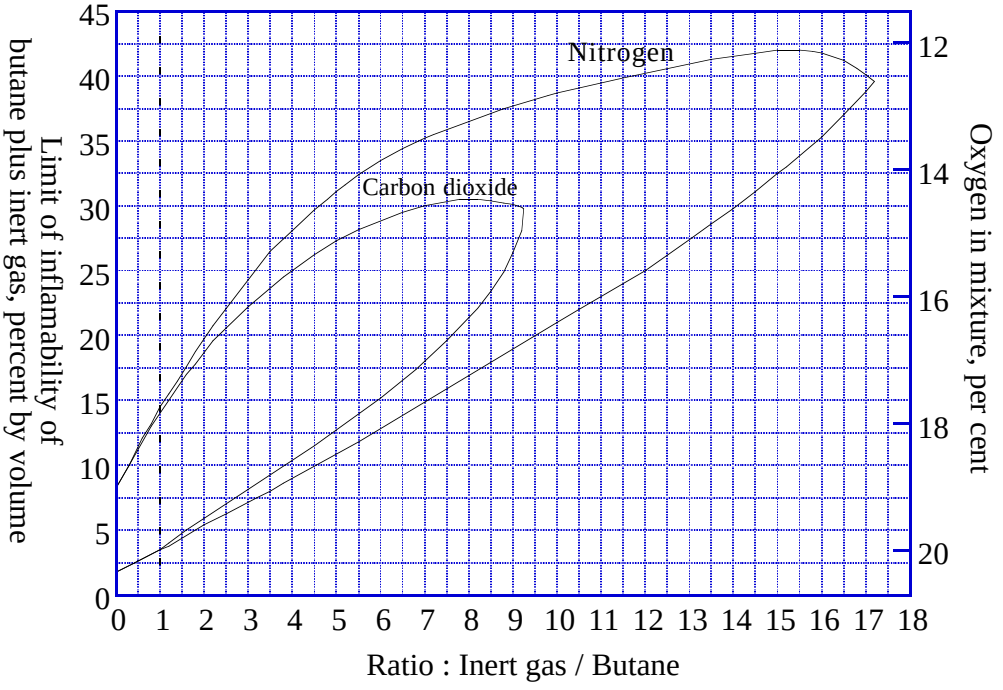

Figure 5.1: Limits of inflammability of butane and air when mixed with various proportions of nitrogen and carbon dioxide.

5.3 Experimental Setup

We made 30×30 cm^2 large RPCs using 2 mm thick float glasses. A float glass is produced by means of "float process" in which molten glass is fed onto a molten tin bath. One side of the glass surface is made in contact with the tin, while the other is exposed to the air, thus the material characteristic of each surface is different. The surface resistivity of the "tin face" is measured to be $(1.01 \pm 0.03) \times 10^{12}$ $\Omega/\Box$ with less dispersion compared with that of "air surface" measured to be $\sim 5 \times 10^9$ to $\sim 7 \times 10^{10}$ $\Omega/\Box$ [33]. Then, we decided to use the "tin face" as the inside surface of the RPC. Figure 5.2 and Figure 5.3 describe the overview of the RPC used for the present studies. The RPC consists of two plates of 2 mm thick float glass as a resistive electrodes. Its gap spacing which is filled with a gas is kept 2 mm by the two types of spacers; edge spacer and inner spacer. The edge spacers are 2 mm thick and T-shaped Noryl spacers by which the RPC is surrounded and they also shut the gas tightly. The inner spacers are three Noryl with about 2×2 mm^2 cross section and 17 cm long which are located as shown in Figure 5.2 so that the gap can be kept 2 mm rigidly and to form gas' flowing route. A 25×25 cm^2 carbon tape, SHINTRON STR-9140 with a surface resistivity of $\sim 5 \times 10^7$ $\Omega/\Box$ on which a high voltage is supplied through a Cu tape and a HV connector is put on the outside of the glass. A plus and a minus high voltages are supplied to each of the two glass electrodes. This carbon tape plane is covered with a mylar sheet and is insulated from the outside. The gas inlet and outlet are secured by the two gas connectors.

Argon, butane and Freon gas from their bottles are mixed at the gas mixer with mass flow controller which controls the flow of individual gas, then the mixed gas is supplied to the RPCs. The flow rate was set about 20 cc/min in total.

Figure 5.4 shows the experimental setup and the logic of the measurement system for testing the RPC performance by using cosmic rays. Cosmic rays are triggered by the 3-fold coincidences of scintillation counters, T1, T2, and T3. T1 and T3 have 20×20 cm^2 active area, and T2 has 9×20 cm^2 active area, in the case of using 18 copper strips to measure multiple hit of strips (see later), however, 1×20 cm^2 "finger" scintillation counter has been used for T2 in order to use the cosmic ray passing through in the center of the strips and to count the hit strips exactly. To absorb electromagnetic showers 5 cm thick lead blocks are placed between the RPC and T3. The gate duration has been set to

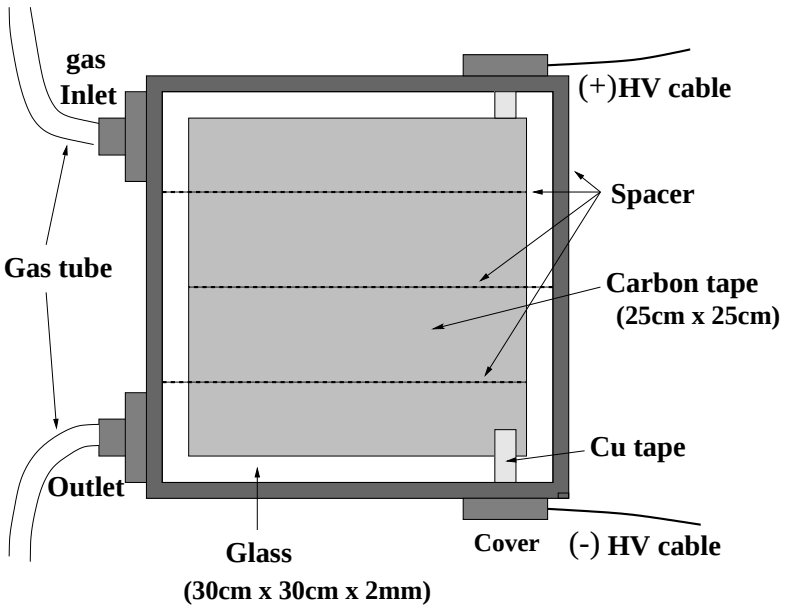

Figure 5.2: Top view of the RPC.

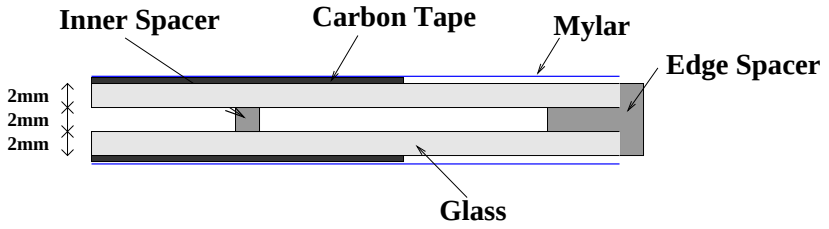

Figure 5.3: Cross section of the RPC.

500 nsec.

At first, a 25×25 cm^2 copper pad has been used to read out the signals from the RPC as shown in Figure 5.5(a). The pad is placed on the surface of the RPC. Since its surface is transparent to the electric pulses originated from inside RPC due to its high resistivity, we can read the signal through copper strips without connecting to high voltage electrodes. The 10 mm thick dielectric foam is placed between the pad and the ground plane for impedance matching of the readout pad with 30 m coaxial cable with a characteristic impedance of 50 Ω. The signals from the RPC are transported through the coaxial cable and are divided into two at the linear Fan In/Out. One goes into ADC(LeCroy2249W)-input, and the other goes into TDC(LeCroy2228A)-stop and a scaler by way of a discriminator. The threshold of the discriminator has been set at 30 mV through this experiment. What we have measured in this setup are the efficiency, the dark current, the single count rate, the ADC(charge) distribution, and the TDC(time) distribution depending on HV

and gas mixtures. In order to measure the discharge(streamer) size, we have used 18 strips with 3 mm wide and 2 mm in gap spacing for readout as shown in Figure 5.5(b), besides one 25 × 25 cm^2 pad. The 2 mm thick PVC is placed between the readout strips and the ground plane for impedance matching of readout strips. In this setup we have mainly measure the multiple hit; the number of hit strips.

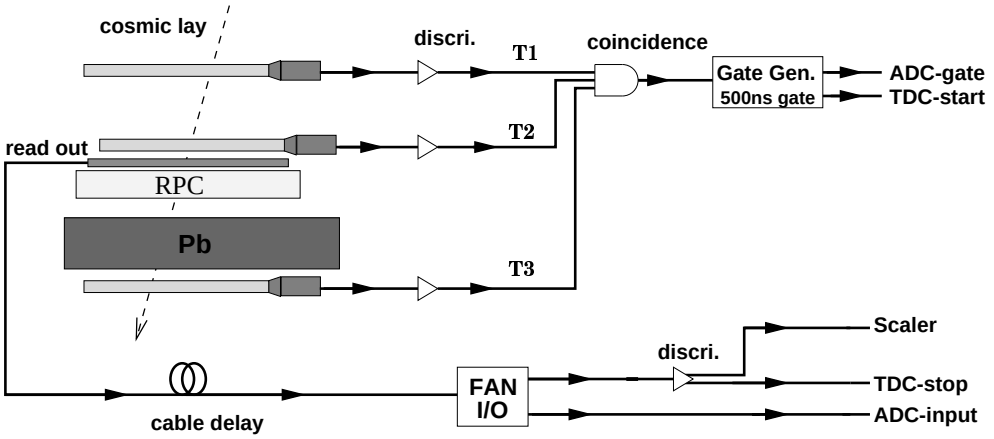

Figure 5.4: The logic concerning trigger.

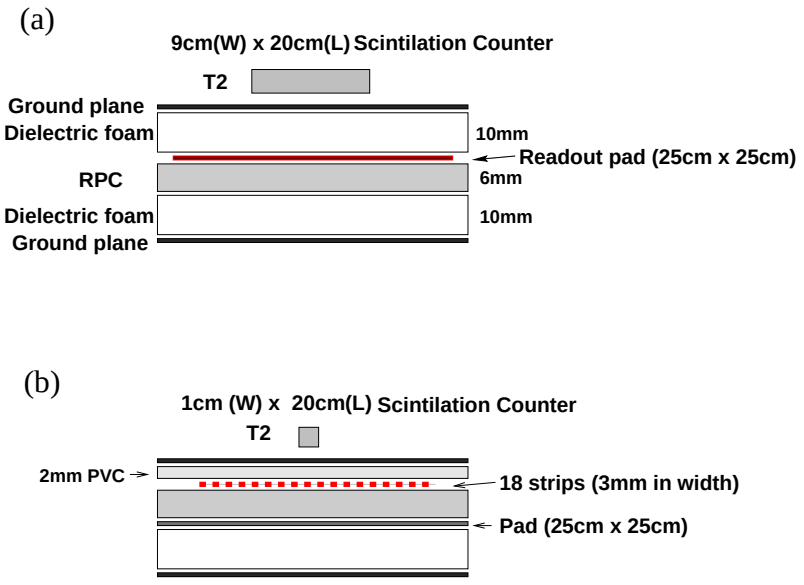

Figure 5.5: Schematics for readout. The 25 × 25 cm^2 pad has been used for reading out the signals normally (a), however 18 readout strips with 3 mm wide has also been used to measure the discharge size (b). The 10 mm thick dielectric foam in (a) and the 2 mm thick PVC in (b) are placed for impedance matching of the readout.

5.4 Quantities Characterizing the RPC Performance

In this section, the quantities which characterize the RPC performance are explained.

- **HV**

A plus and a minus high voltages are applied to the anode and the cathode of the RPC, respectively. The HV supplied for the RPC is written as $\pm x$ kV, which means the electric potential difference between the two electrodes is $2x$ kV.

- **Efficiency**

The efficiency of the RPC is derived by measuring the simultaneous rates of coincidences between the hit in the RPC and the 3-fold coincidences of scintillation counters. That is, let the signal from the RPC be S and the signals from the scintillators T_1, T_2 and T_3 respectively, then the efficiency is defined as

$$\text{efficiency} \equiv \text{rate}\left(\frac{S \cdot T}{T}\right), \tag{5.1}$$

where,

$$T = T_1 \cdot T_2 \cdot T_3. \tag{5.2}$$

The signal from the RPC S is derived from the record of the TDC. When the signal from the RPC has the pulse hight more than the threshold of the discriminator (30 mV) and leaves the meaningful record on the TDC, we consider that there is a hit in the RPC. 1000 cosmic ray events, $T = 1000$ were collected for each test.

- **Single count rate**

The single count rate is defined as the number of pulses generated in the RPC, including both signals and noises. The pulse from the RPC is read out by the pad and is fed into the discriminator. If its pulse height exceeds the threshold of the discriminator, it is counted in the scaler. The width of the output pulse from the discriminator is set to 70 nsec. The single count rate is described in Hz/cm^2.

• **Dark current**

The dark current is defined as the current supplied to the RPC from the high voltage power supply. Reading out this value is done by using the current monitor terminal in the HV power supply with the accuracy of 10 nA. Divided by the size of the readout pad, the dark current is described in $\mu A/m^2$.

• **Time resolution**

Hit times in the RPC is recorded on the TDC in terms of the time difference between the time when the trigger signal from scintillators enters the TDC-start and the one when the signal from the RPC enters the TDC-stop. In order to reduce the errors arising from the scintillators, we have used two RPCs in piles for measuring time resolution. When the difference between hit times in the two RPCs is plotted, time resolution is defined from the standard deviation of a Gaussian fit of this distribution as the standard deviation divided by $\sqrt{2}$.

• **Charge**

The ADC gate is opened by the trigger signal from the scintillators. The gate duration has been set to 500 nsec by the gate generator. During this duration, all the charges from the readout pad, if any, is integrated, and recorded on the ADC. The long gate duration insures that possible secondary discharges, generated by the primary one via photoionization processes, are efficiently detected if any, even though abnormally delayed.

• **Strip multiplicity**

The strip multiplicity is defined as the mean number of hit strips when the discharges arising from passing cosmic rays occurred in the RPC. The signal picked up from each strip is sent to each TDC channel independently via discriminator with 30 mV threshold. We have estimated the pulse size by measuring this multiplicity.

5.5 Results

• **Efficiency curve**

Figure 5.6 shows the efficiency curves as a function of HV for three types of gas mixtures, Argon 25%/Butane 0%/Freon 75%(no butane mixture), Argon 0%/Butane 8%/Freon 92%(no argon mixture), and Argon 25%/Butane 25%/Freon 50%(standard gas). The efficiency for the gas mixture without butane is about 60% at the most. Its signals have after-pulses heavily, and the dark current, the single count rate, the charge, are very high. The effect of the secondary discharges is significant in this gas mixture. On the other hand, the RPC with no argon gas mixture shows more than 90% efficiency. Its operating HV, however, is quite high. Considering the operation for a long term, it is not good to operate the RPC at such a high HV.

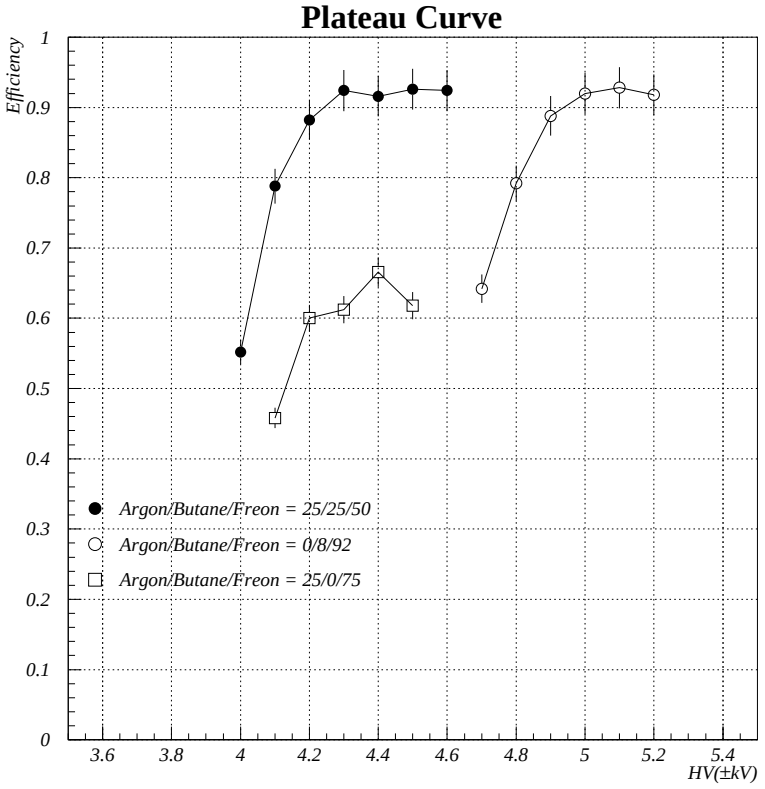

Figure 5.6: Efficiency curves for the gas without butane and without argon.

Figure 5.7 shows the efficiency curves for each gas mixture of 20 combinations listed in Table 5.1. Each plot (a), (b), (c) and (d) shows the case of using 25%, 12%, 8% and 4% butane gas mixtures respectively, and (c) and (d) correspond to nonflammable gas

mixtures. Each gas mixture shows more than 90% efficiency in the plateau region with similar curve shape.

For comparison of the RPC performance for different gas mixtures, we define a plateau HV as shown in Figure 5.8. We choose three points out of five points in the region of rising efficiency so that the fitting line of these three points can have the steepest slope, and we calculate the mean value of another three points which is clearly in the region of plateau. Then, we calculate the cross point HV(knee HV) of these two lines. The plateau HV is defined as 200 V/mm above the knee HV. In the following, the data at the nearest tested HV to the plateau HV are referred for comparison.

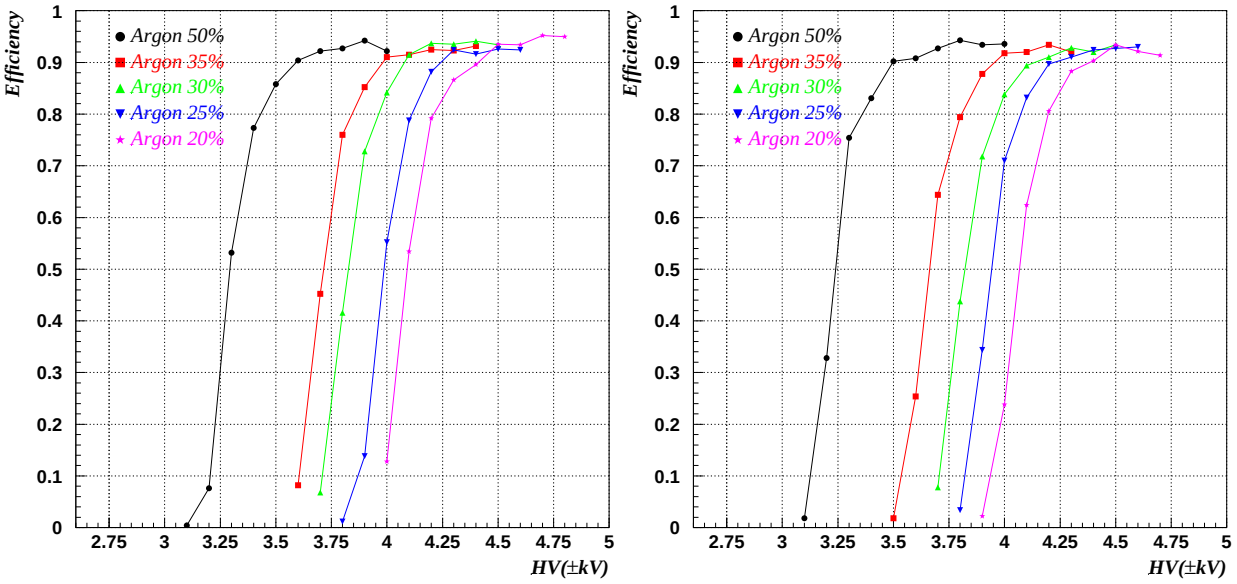

(a)butane 25%

(b)butane 12%

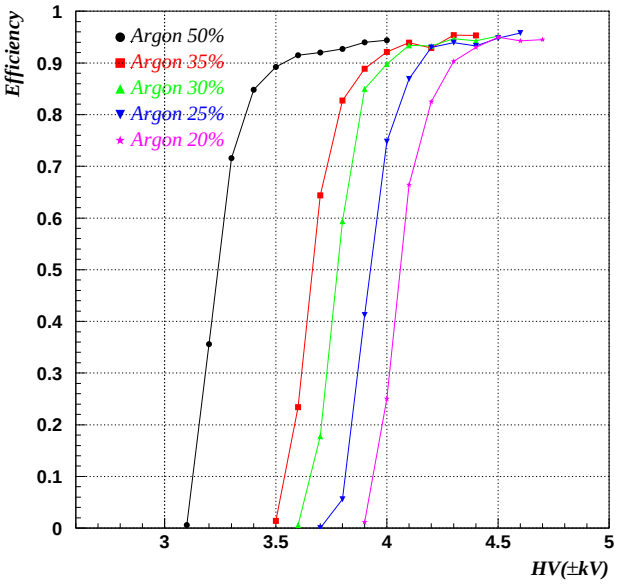

(c)butane 8%

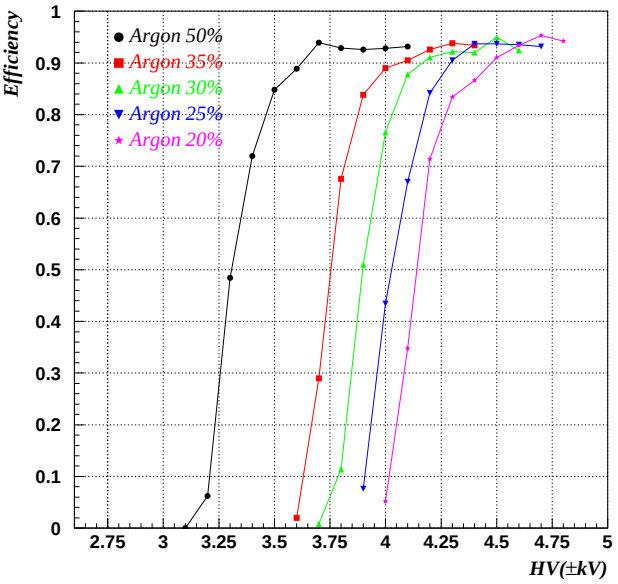

(d)butane 4%

Figure 5.7: Efficiency curves for each gas mixture of 20 combinations. (a), (b), (c) and (d) shows for the case of using 25% butane, 12% butane, 8% butane, and 4% butane gas mixture, respectively.

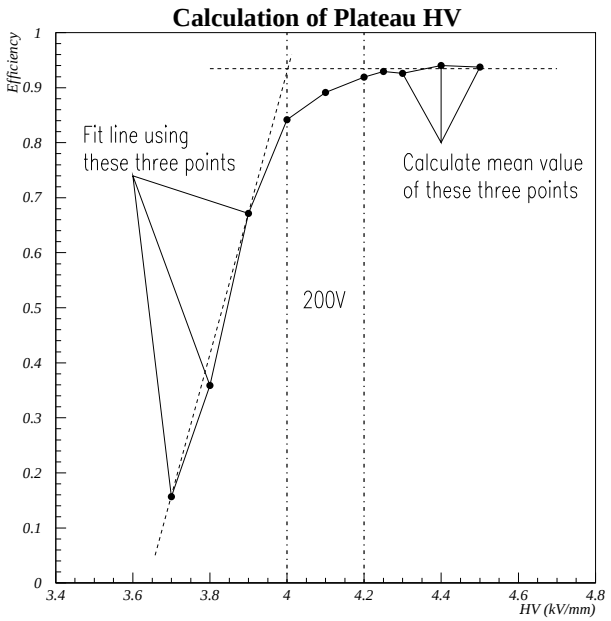

Figure 5.8: Definition of plateau HV.

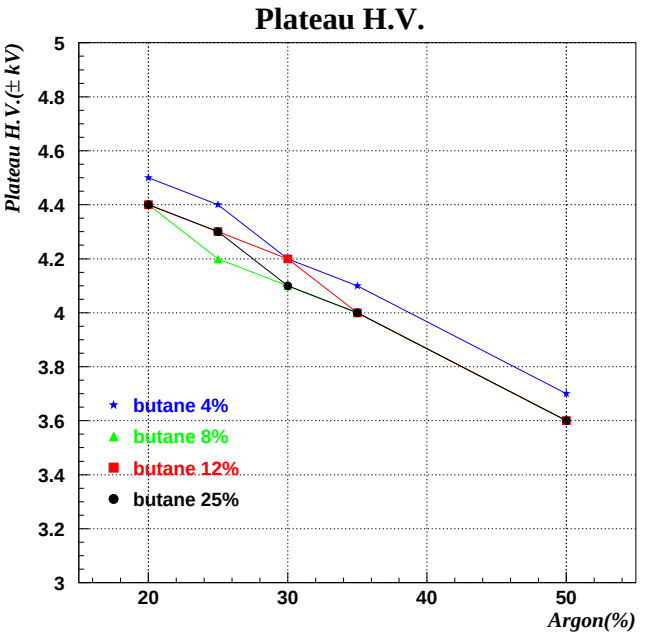

Figure 5.9: Plateau HV for each gas mixture.

Figure 5.9 shows the plateau HV versus Ar fraction including four different butane fractions shown in Table 5.1. The butane fractions are distinguished by the marks. It is clear that plateau HV depends hardly on the butane fraction, but it is determined mainly by the fraction of argon and Freon. Freon is considered to quench the streamer size by absorbing electrons from the avalanche. If there is much Freon in the gas, the avalanche is hard to grow a detectable streamer. Under a constant butane fraction, increasing the fraction of argon means reducing the fraction of Freon, then both effects of a ionized argon and a quenching Freon cause a lower plateau HV. A plateau HV decreases about 130 V/mm with increasing the fraction of argon by 5% under a constant butane fraction.

• **Efficiency, Dark current, Single count rate and Time resolution**

Figure 5.10 shows the efficiency, the dark current and the single count rate for each gas mixture at the plateau HV. Each gas mixture shows more than 90% efficiency. The dark current and the single count rate are about 0.5 μA/m^2 and 0.055 Hz/cm^2 respectively. These values are almost consistent with what have been measured for RPCs for endcap KLM.

Figure 5.11 shows the distributions of time difference between hits in two RPCs, (a) for the standard gas (flammable), and (b) for the gas mixture of Argon 30%/Butane 8%/Freon 62% (nonflammable). There is no significant difference between the two distributions. Time resolution has been evaluated by fitting the distribution to a Gaussian, even though the fit is not the best one. In fact, the distribution is characterized by not only a Gaussian peak, but also non-Gaussian tails, which can be explained partly by particles crossing near the spacers where the electric field is disturbed [34]. Plotting the time resolutions for each gas mixture at the plateau HV, we have Figure 5.12. There are no systematic difference between the time resolutions for flammable(butane 25%, 12%) and for nonflammable(butane 8%, 4%) gas mixtures. The time resolutions are about 2.5 nsec. The distributions of time difference for each of twenty gas mixtures are shown in Figure 5.18 and 5.19.

There are no significant differences for the efficiency, the current, the single count rate and the time resolution, for each gas mixture at the plateau HV. These values are almost independent of the gas mixtures.

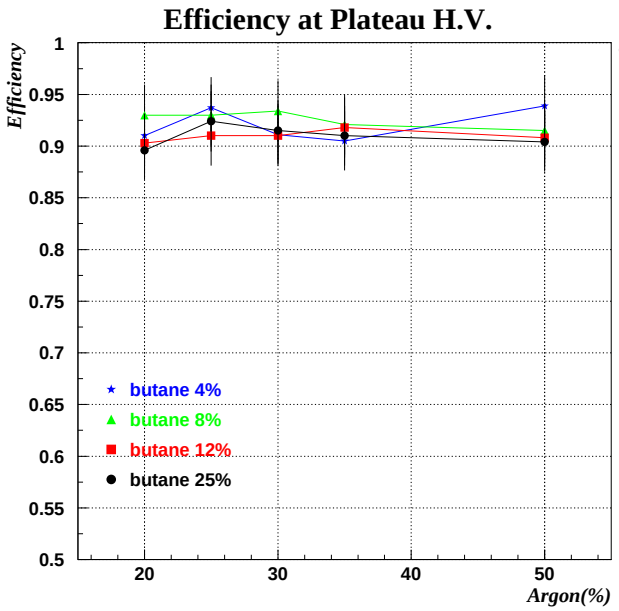

(a)Efficiency

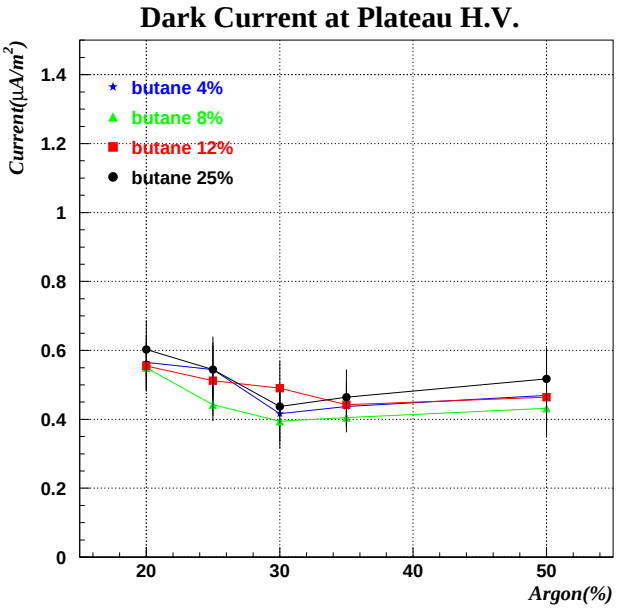

(b)Dark Current

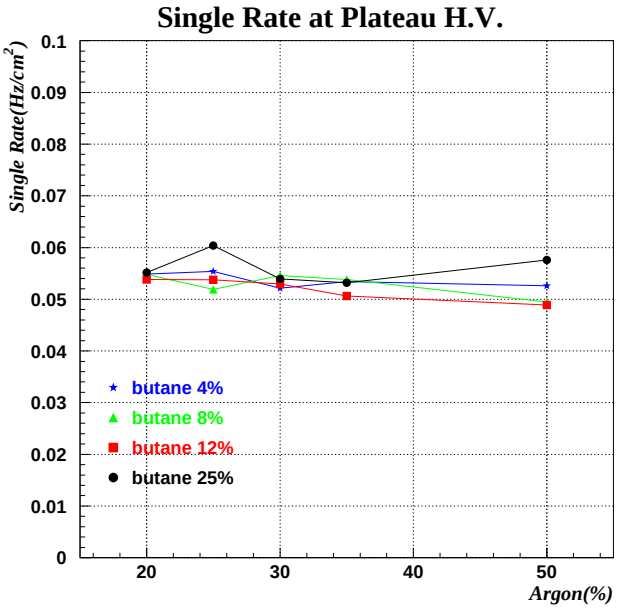

(c)Single Count Rate

Figure 5.10: (a)Efficiency, (b)Dark current and (c)Single count rate versus Ar% at the plateau HV for each of the gas mixtures.

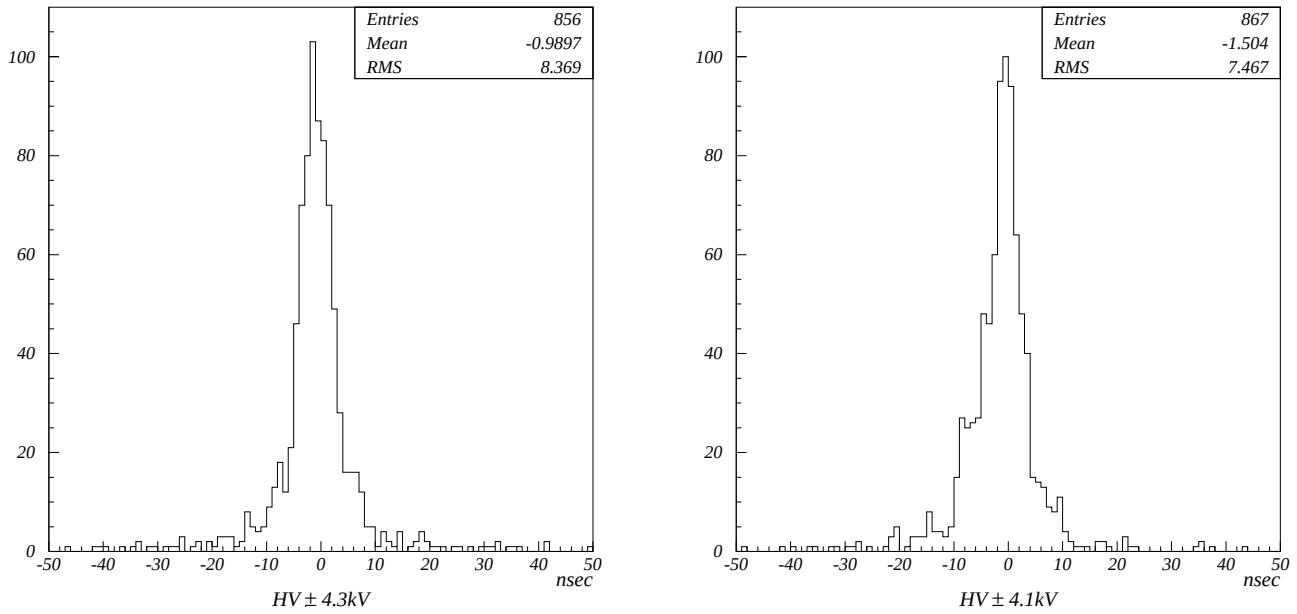

(a) Argon 25%/Butane 25%/Freon 50%

(b) Argon 30%/Butane 8%/Freon 62%

Figure 5.11: Distributions of time difference of hits in two RPCs at the plateau HV, (a) for the standard gas, (b) for one of the nonflammable gas mixtures.

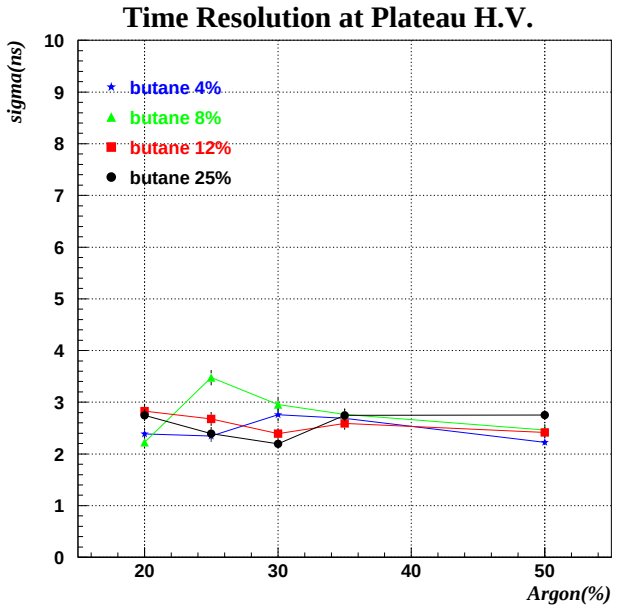

Figure 5.12: Time resolution versus Ar% at the plateau HV for each of the gas mixtures.

• **Charge distribution**

Figure 5.13 shows the charge distributions at the plateau HV for the flammable standard gas (a), and for the nonflammable gas mixture of Argon 30%/Butane 8%/Freon 62% (b). In these figures, we pay attention to the "second" peak following the main(first) peak. The nonflammable gas mixture is likely to have larger the second peak than the standard gas. This second peak is considered to indicate the degree of the secondary discharges. A typical signal from the RPC is a single pulse with 100 mV in pulse hight as shown in Figure 5.14(left), and this corresponds to the first peak in the charge distribution. Some signals, however, contain after-pulses(right), which cause the increasing total charge corresponding to the second peak. Since the after-pulses are considered to originate from the secondary discharges, it can be thought that the gas mixture having more second peak in the charge distribution makes more secondary discharges. Figure 5.20 and 5.21 shows the charge distributions for each of twenty gas mixtures at the plateau HV. We can see that the second peak is likely to become large with decreasing the butane fraction. The effect of reducing the fraction of butane which is considered to prevent the secondary discharges by absorbing UV photons can be seen in these figures. Plotting the first peak ratio in the charge distribution for each gas mixture, we have Figure 5.15. This figure indicates the gases with 25% and 12% butane make about 15% after-pulse and the gases with 8% and 4% butane make about 25% after-pulse. In the case of 0% butane gas mixture, we can hardly find the first peak and the percentage of the after-pulse is almost 100%(not shown). Although no butane gas mixture has 100% after-pulse, if there is even a little butane fraction such as 4%, the after-pulse can be reduced to 25%. A butane is inevitably need, but with even a little butane fraction the second discharges are suppressed quite well. Figure 5.16 shows the mean values of the charges for each gas mixture. No remarkable differences can be seen for the butane fraction in spite of the difference of the second peak. This is because the charge distribution slightly moves to the low with decreasing the butane fraction. Decreasing the butane fraction means increasing the fraction of Freon that quenches the streamer size. As a result, the charge distribution is shifted to the low. In charge distribution, the nonflammable gas mixture is likely to have more second peak compared with the flammable gas mixture. However, this is not significant.

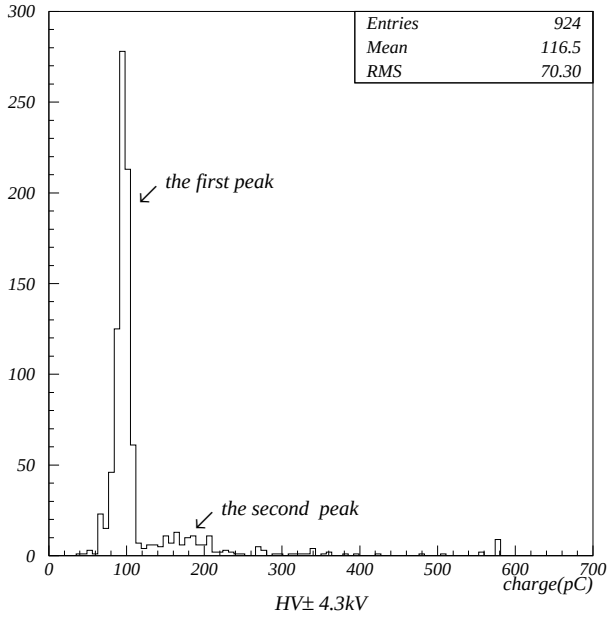

(a) Argon 25%/Butane 25%/Freon 50%

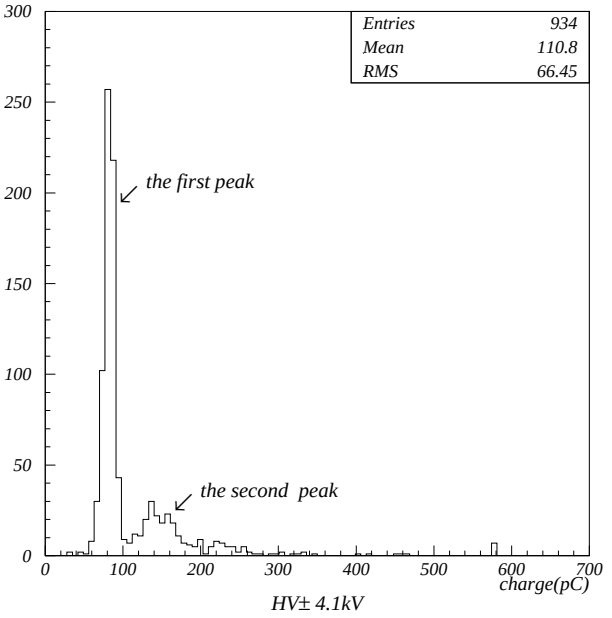

(b) Argon 30%/Butane 8%/Freon 62%

Figure 5.13: Charge distributions at the plateau HV, (a) for the standard gas, (b) for one of the nonflammable gas mixtures.

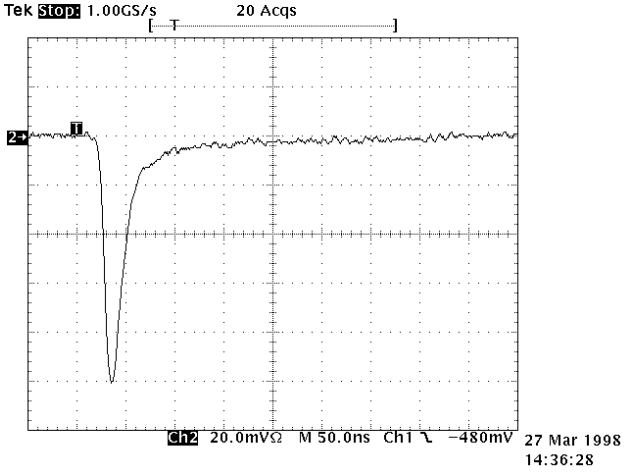

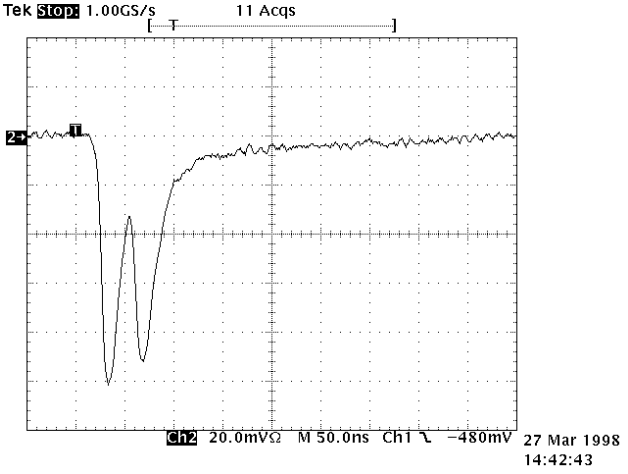

Figure 5.14: The left figure shows the typical signal from the RPC, and the right shows the signal involving after-pulse.

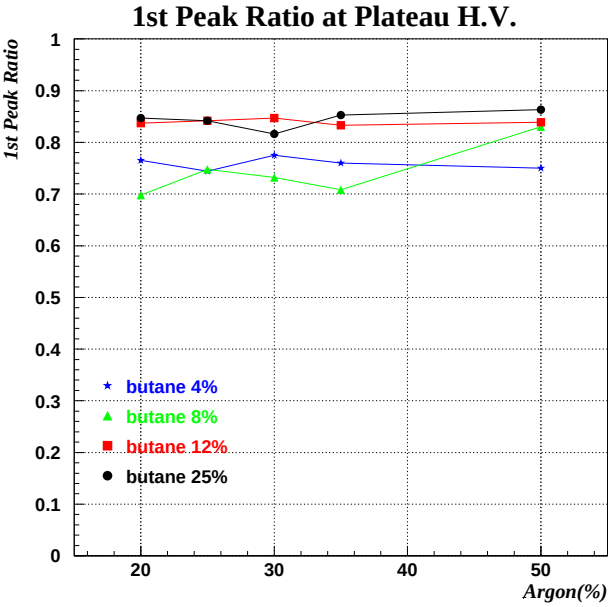

Figure 5.15: 1st peak ratio at the plateau HV for each gas mixtures.

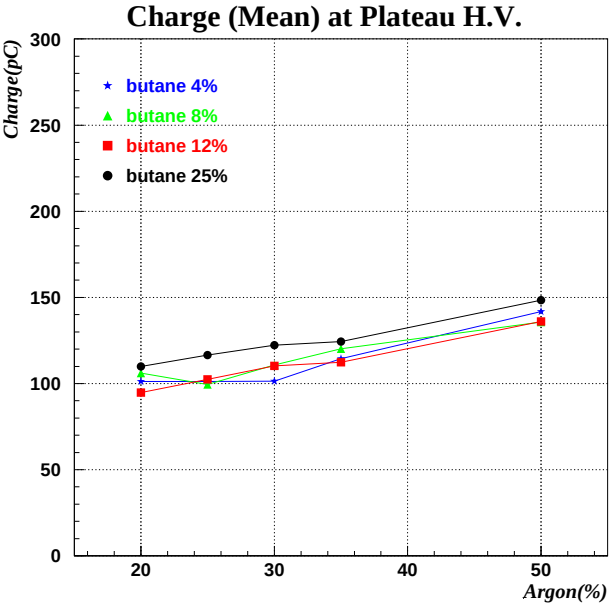

Figure 5.16: Mean charge at the plateau HV for each gas mixtures.

• **Strip multiplicity and discharge size**

Now we see whether the effect of the second discharges by reducing the butane fraction affects the spread of the signal pulse. This is important for the actual analysis in which we measure the particle track. For this purpose, we use 18 strips with 3 mm wide and 2 mm in gap spacing for the pickup of the signals. Figure 5.17 shows the average strip multiplicity at the plateau HV for each gas mixture. Multiplicity is defined as the multiple hit; the number of hit strips. The multiple hit distributions for each gas mixture are shown in Figure 5.22 and Figure 5.23. There are no significant differences for the butane fraction. This indicates that the second discharges would not take place far from the position of the first discharge and it does not influence the spread of the pulse. On the other hand, the multiplicity gets high with increasing the argon fraction. This is because the pulse hight for the gas mixture with much argon tends to get high. Therefore if we choose the threshold appropriately, we will be able to reduce its multiplicity.

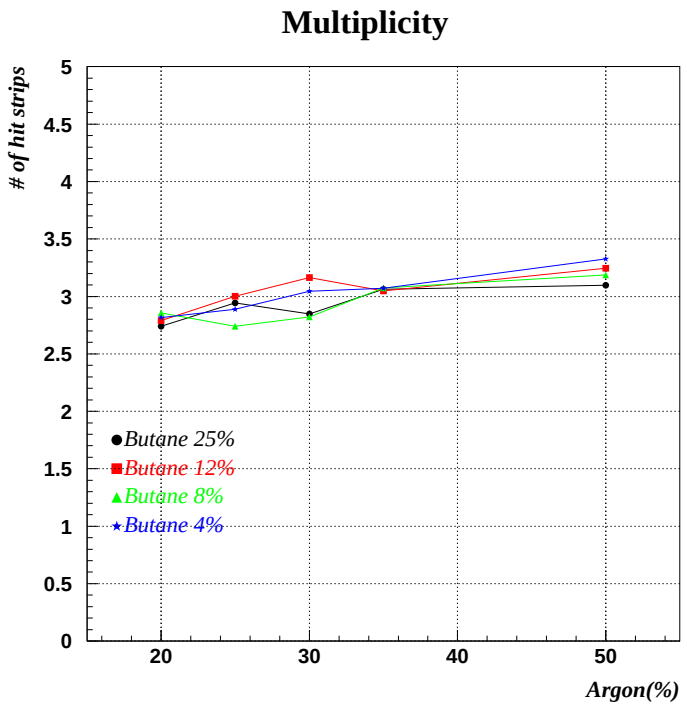

Figure 5.17: Multiplicity; mean value of the number of hit strips, at the plateau HV for each gas mixtures.

5.6 Conclusions

We have tested twenty combinations of gas mixtures. These gas mixtures are classified into a flammable or a nonflammable gas by the fraction of butane. We have compared nonflammable gas mixtures with flammable ones. Each gas mixture results in more than 90% efficiency at the plateau HV. For the dark current, the single count rate and the time resolution, there are no significant differences for each gas mixture at the plateau HV. In the charge distribution, we found the effect of a nonflammable gas mixture reducing the butane fraction. Nonflammable gas mixture is likely to make more secondary discharges. These secondary discharges, however, are not so critical and don't affect the spread of the pulse, that is, no significant differences are found for the multiplicity for the fraction of butane. Moreover, to be nonflammable is good thing in itself for safety or for avoiding complicated procedures required for a flammable gas mixture. Therefore, it is concluded that nonflammable gas mixture is useful enough. And now we use the nonflammable gas mixture of butane/argon/HFC134a = 8/32/60 for the RPCs for the KLM.

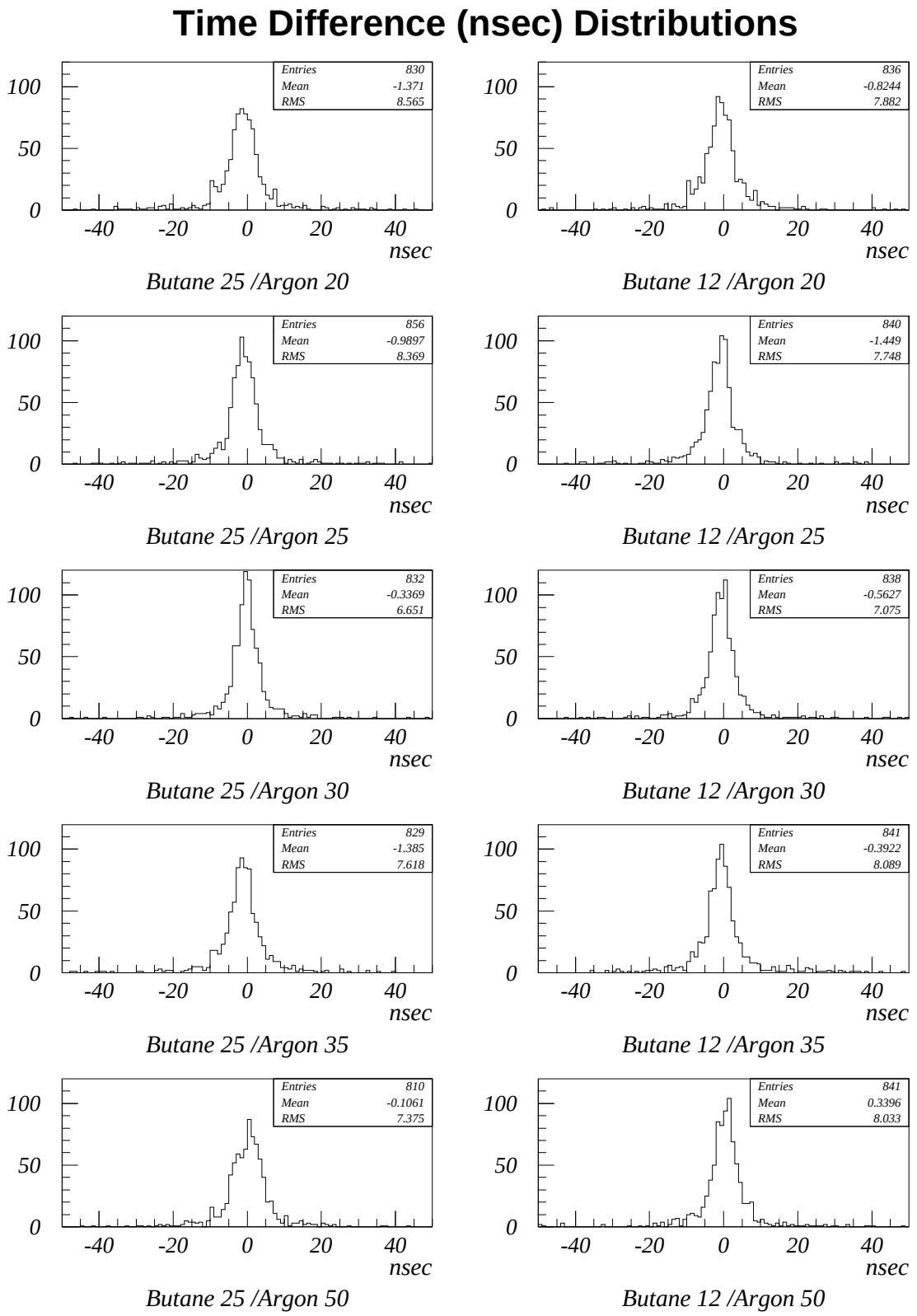

Figure 5.18: Distributions of time difference between hits in two RPCs for flammable gas mixtures at the plateau HV.

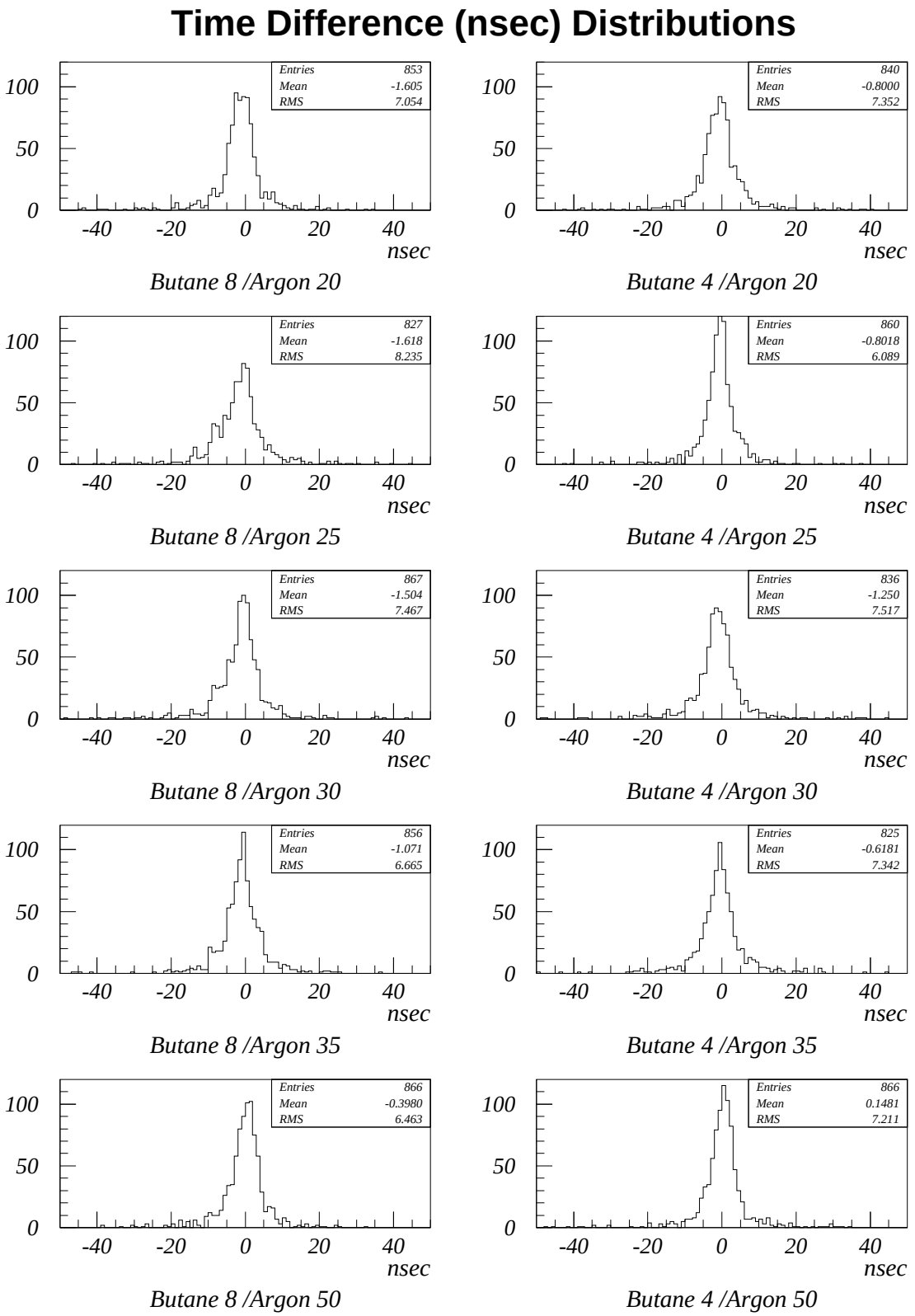

Figure 5.19: Distributions of time difference between hits in two RPCs for nonflammable gas mixtures at the plateau HV.

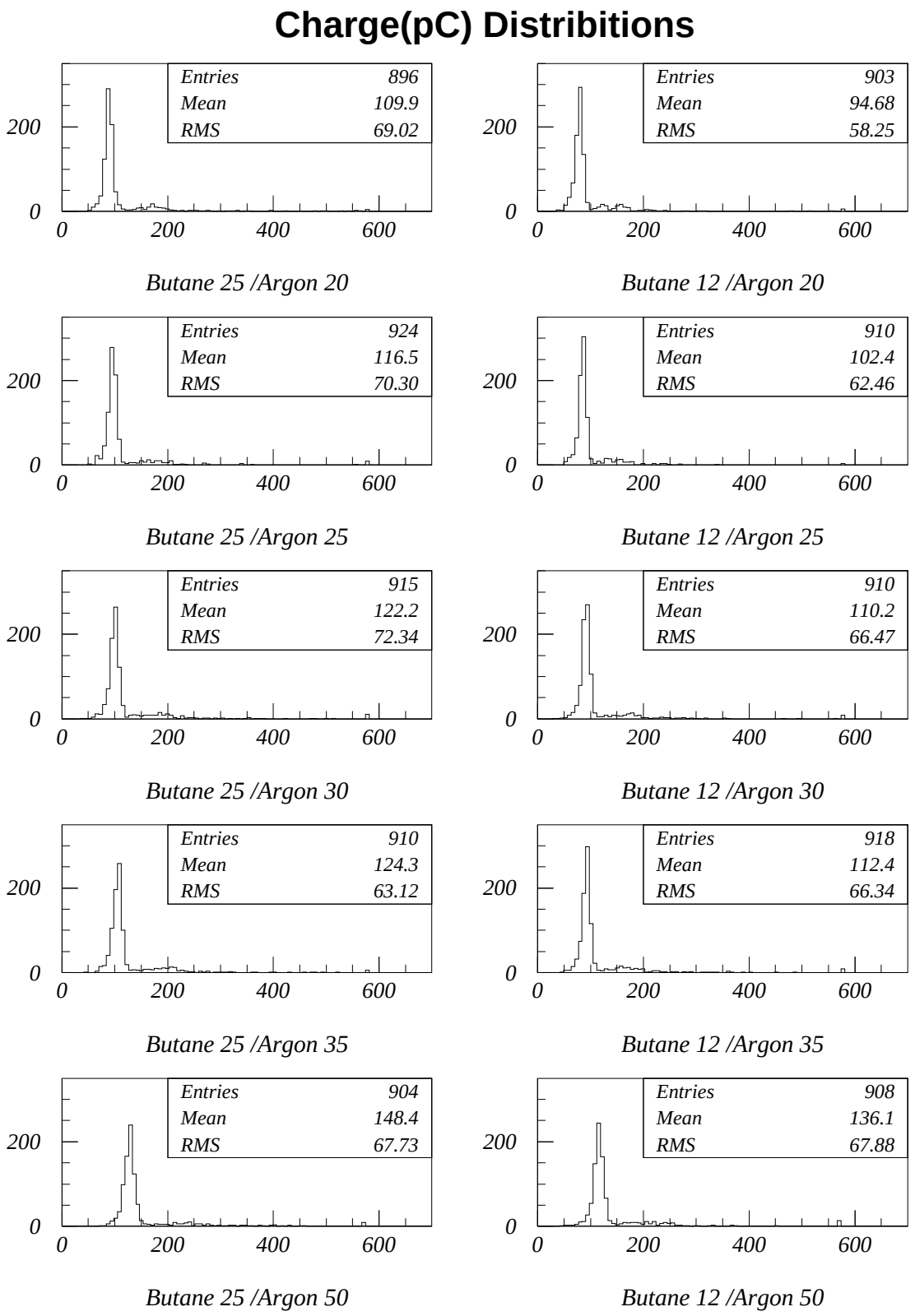

Figure 5.20: Charge distributions for flammable gas mixtures at the plateau HV.

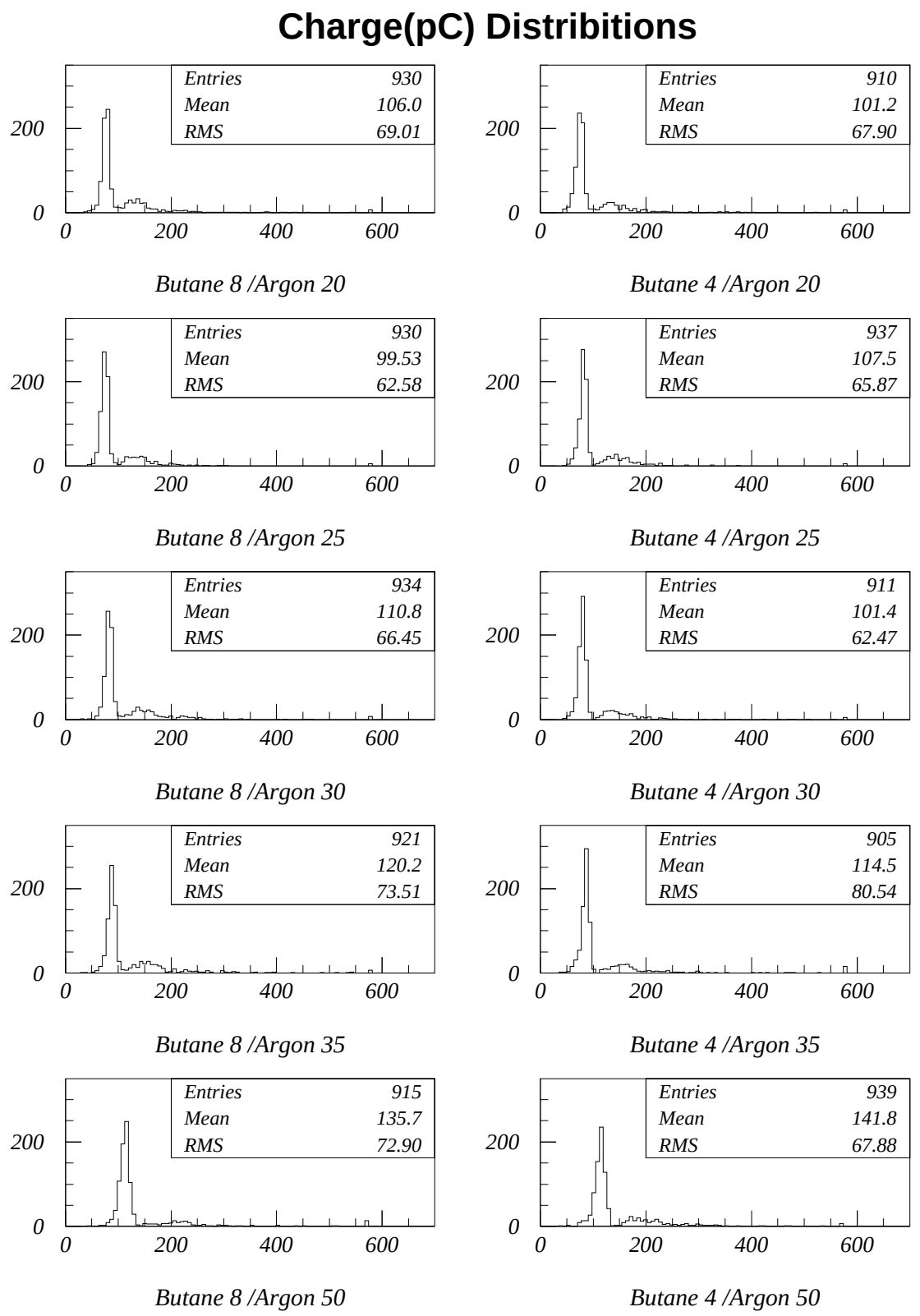

Figure 5.21: Charge distributions for nonflammable gas mixtures at the plateau HV.

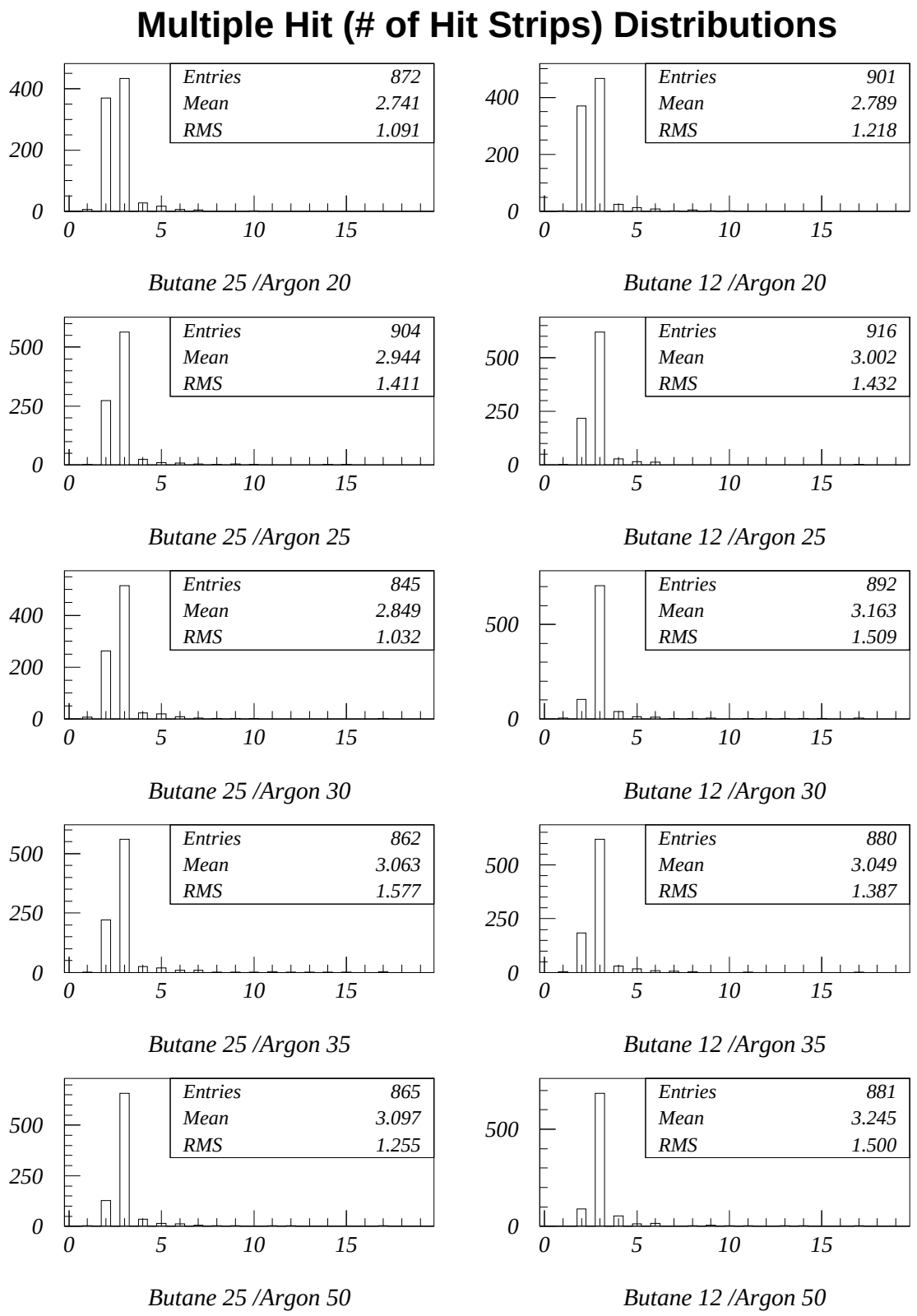

Figure 5.22: Multiple hit distributions for flammable gas mixtures at the plateau HV.

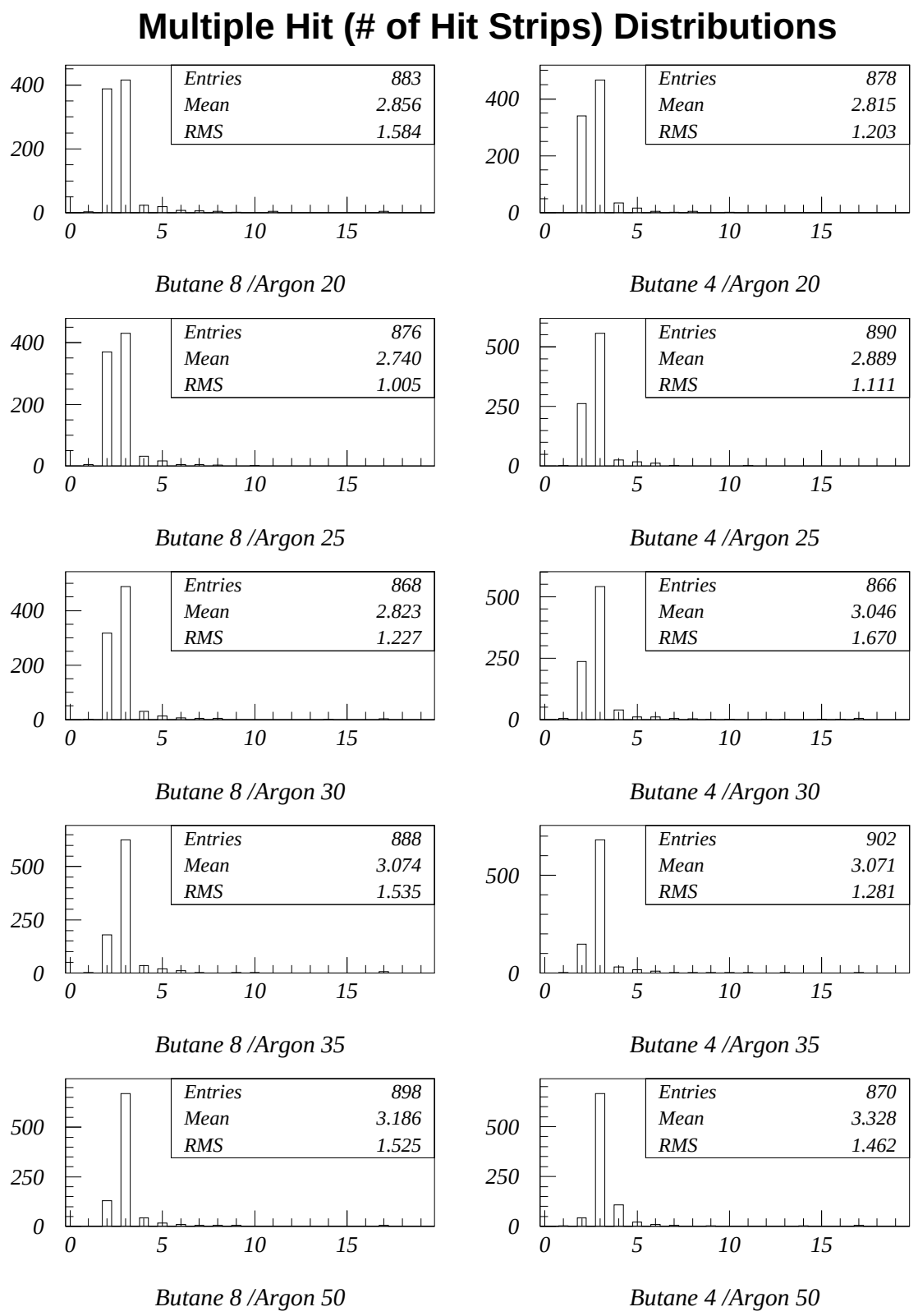

Figure 5.23: Multiple hit distributions for nonflammable gas mixtures at the plateau HV.

Chapter 6

Study of Freonless Gas Mixture

6.1 Introduction

Freons have been used for RPCs as the quenching agent. At first, we used CF_3Br that was known to destroy the atmospheric ozone layer. After examining several gases, we could replace CF_3Br with HFC134a having negligible ozone depletion potential[31], and our favorable gas mixture for the present is the nonflammable one containing 30% argon, 8% butane and 62% HFC134a, as discussed in the previous chapter.

HFC134a, however, has a risk of global warming even if it is not an ozone-depleting substance. Since it is estimated that HFC134a has about 1300 times as high global warming potential as carbon dioxide (CO_2), it is not desirable to use HFC134a if possible.

We have tested two alternative gases, oxygen and sulfur hexafluoride (SF_6), both of which have high electron affinity. Oxygen does not influence global warming at all. Although SF_6 has higher global warming potential than HFC134a per molecule, if the RPC can work showing good performance with a few percent SF_6 concentration, the global warming potential of the whole gas mixture can be reduced to less than that of the HFC134a gas mixture. We actually have tested such gas mixtures.

In this chapter, we present the performance of the RPC when using these Freonless gas mixtures and the additional feasibility to operate RPCs at very low voltage when using SF_6 gas mixtures. The obtained results have been compared with the data for the HFC134a gas mixture.

6.2 The Alternative Gas to the HFC134a

As described in the previous chapter, HFC134a behaves as a quencher of the streamer in the RPC by electron capture, for HFC134a (CH_2FCF_3) contains, in the molecule, four fluorines (F) that are electronegative. An electronegative gas is certainly needed for the RPC in which ionizing particles are subjected to a uniform field which is made by two parallel electrodes and is strong enough to produce gas multiplication. The discharges spread over full region of the RPC easily unless an electronegative gas is added to the RPC. On the contrary, this is not always the case for wire chambers in which ionizing particles are subjected to a radial field, and only very close to the wire, the field gets strong enough so that multiplication starts.

The following are required for the alternative gas to the HFC134a.

- To be electronegative
- To be environmentally friendly
- To be nonflammable
- To be gas at a normal conditions (standard temperature and pressure)

At first, to be electronegative is required by considering the behavior of HFC134a in the RPC. To be environmentally friendly are required from the point of view of environmental protection. To be environmentally friendly means not to cause the global warming as well as ozone depletion. A halogen such as the fluorine (F) is electronegative in general. The chlorine (Cl) and the bromine (Br) are also halogen and electronegative, however, they are known to destroy the ozone layer. Therefore the choice of the gas having these two elements is rejected. To be nonflammable and to be gas at a normal conditions are required for the easiness of the handling.

Considering these requirements, we have chosen oxygen (O_2) and sulfur hexafluoride (SF_6) as substitutes for HFC134a. Electron capture cross sections in the molecule O_2 and in the molecule SF_6 are shown in Figure 6.1 and Figure 6.2, respectively. Both gases are known to be electronegative. In O_2 the cross section peak occurs around an energy of 6 eV with the cross section $\sigma \sim 1.3 \times 10^{-18}$ cm^2, while in the SF_6 the peak is at 0 eV with

$\sigma \sim 5.7 \times 10^{-16}$ and the cross section decreases with electron energy. Typical electron energy in the gaseous chamber is considered to be of the order of 10^{-2} eV $-$ 10 eV [26].

Although O_2 does not cause global warming at all, the problem of inflammability comes up again. Then we have used O_2 combined with CO_2. Figure 6.3 illustrates limits of inflammability of butane and air when mixed with carbon dioxide. Dispersed in the air, a gas mixture that crosses the region surrounded by the points is classified as flammable. The dashed line represents the limits of inflammability. For example, the gas mixture with 4% C_4H_{10} and 5% O_2 follows the solid line and is considered to be nonflammable. Referring to this figure, we have chosen gas mixtures.

Table 6.1 shows the global warming potential (GWP) per molecule for HFC134a and SF_6 as the value for CO_2 to be 1. SF_6 has 24900 times as high GWP as CO_2 while HFC134a has 1300 times as high GWP as CO_2. Although SF_6 has higher GWP than HFC134a per molecule, since the HFC134a gas mixture of Ar 30%/C_4H_{10} 8%/HFC134a 62% contains much HFC134a, if RPC can work efficiently with a few percent SF_6 concentration, the GWP of the whole gas mixture can be reduced to less than that of the HFC134a gas mixture. We have tested three gas mixtures of Ar 90%/C_4H_{10} 8%/SF_6 2%, Ar 90%/C_4H_{10} 9%/SF_6 1% and Ar 89.5%/C_4H_{10} 10%/SF_6 0.5% with a few percent SF_6 concentrations. The GWP of the gas mixture with 1% SF_6 becomes about one-third as high as that of Ar 30%/C_4H_{10} 8%/HFC134a 62% gas mixture as listed in Table 6.2.

The main characteristics of SF_6 are summarized in Table 6.3 together with the data of HFC134a. SF_6 is gas at a normal conditions as well as O_2.

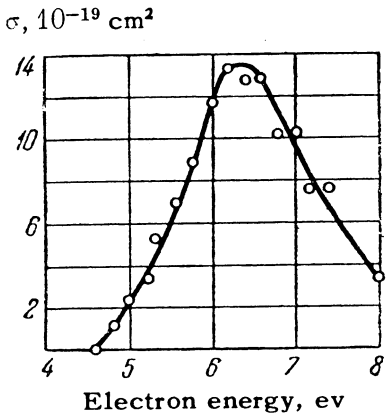

Figure 6.1: Electron capture cross sections in the molecule O_2 [35].

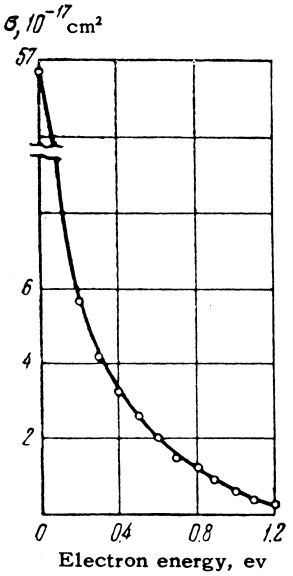

Figure 6.2: Electron capture cross sections in the molecule SF_6 [35].

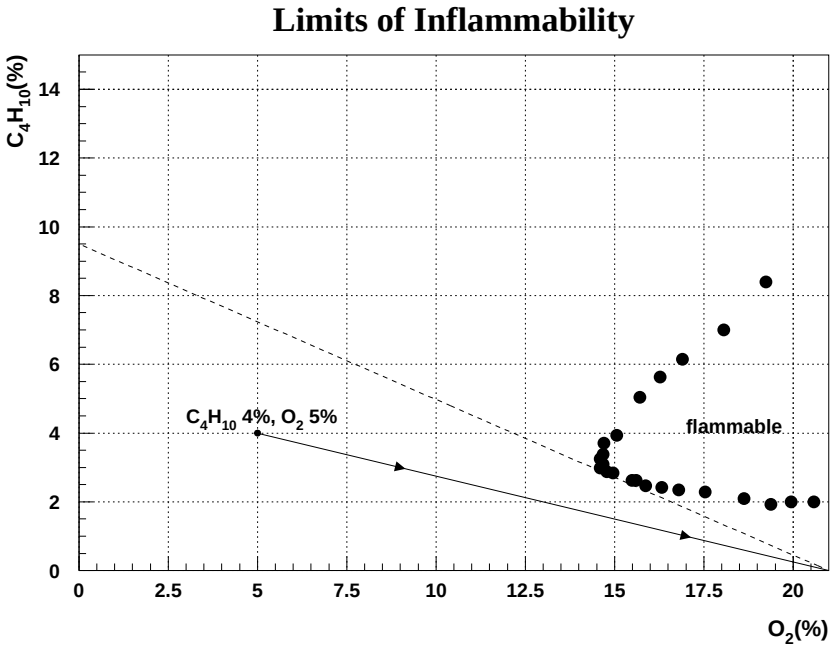

Figure 6.3: Limits of inflammability of butane and air when mixed with carbon dioxide. Dispersed in the air, a gas mixture that crosses the region surrounded by the points is classified as flammable. The dashed line represents the limits of inflammability. For example, the gas mixture with 4% C_4H_{10} and 5% O_2 follows the solid line and is considered to be nonflammable.

Table 6.1: Global warming potentials from IPCC(1994).

substance	Global Warming Potential (GWP)
CO_2	1
HFC134a	1300
SF_6	24900

Table 6.2: Global warming potentials for gas mixtures.

gas mixture	GWP
CO_2 100%	1
Ar 30%/C_4H_{10} 8%/HFC134a 62%	806
Ar 90%/C_4H_{10} 9%/SF_6 1%	249

Table 6.3: Characteristics of SF_6.

	HFC134a	SF_6
Molecular weight	102.0	146.1
Boiling point (^{o}C)	-26.3	-63.7
Inflammability	NO	NO

6.3 Experimental Setup

We have used 30 × 30 cm^2 large RPCs shown in Figure 5.2 and 5.3 again for the present test. The experimental setup is almost same as what described in Figure 5.4 and 5.5. The only difference is that we have used the amplifier with the gain of 4, since the pulse height of the signal when using SF_6 gas mixture is, as shown in below, found to be low particularly at lower HV compared with the minimal threshold of 30 mV.

6.4 Results

6.4.1 O_2 with CO_2 gas mixtures

The efficiencies for O_2 with CO_2 gas mixtures are summarized in Table 6.4. The data for the gas mixture with HFC134a is added in the table for reference. The highest value of 88% is obtained with the mixture of C_4H_{10} 8%/Ar 30%/CO_2 31%/O_2 31%. This value is, however, lower than 94% obtained with HFC134a mixture. Moreover, this gas mixture is considered to be flammable due to containing much oxygen. We have not obtained more than 80% efficiency with the nonflammable gas mixtures.

Note that these low efficiencies are not caused by the too strong quenching capability of O_2 but by its insufficient quenching capability since the signals have many after-pulses and the single count rates show considerably high values.

6.4.2 SF_6 gas mixtures

• Efficiency

The obtained efficiency curves as a function of HV for three SF_6 gas mixtures and HFC134a mixture for reference are shown in Figure 6.4. The efficiencies for three SF_6 gas mixtures reach about 92% at the plateau HVs[1], while the HFC134a gas mixture shows slightly higher efficiency of 94% at the plateau HV. The plateau HVs for the three SF_6 gas mixture are calculated as ±2.1 kV, ±2.2 kV and ±2.3 kV respectively, and the plateau HV for the HFC134a gas mixture is ±4.1 kV.

[1]The plateau HV has already been defined in Figure 5.8

Table 6.4: The efficiencies for various gas mixtures including O_2 and(or) CO_2.

gas fraction (%)				*efficiency*	*flammablity*
C_4H_{10}	Ar	CO_2	O_2	*(%)*	
8	30	31	31	88	Yes
		60	2	77	No
4	20	56	20	77	Yes
		66	10	66	No
		76	0	60	No
	10	86	0	60	No
0	20	40	40	10	No
	10	45	45	12	No
	4	48	48	12	No
	0	50	50	13	No
		10	90	14	No
C_4H_{10}	Ar	$HFC134a$			
8	30	62		93	No

The significant difference is found in the operating HV. We need to apply about ±4 kV to the RPC for the HFC134a gas mixture, on the other hand, the RPC with SF_6 gas mixture can be operated at about ±2 kV. By using SF_6 gas mixtures, we can reduce the HV by about 50%. This has been realized by the balance of Ar and SF_6 fractions. The SF_6 gas mixtures contains Ar as much as 90% which causes the discharges, and even a little fraction of SF_6 such as 2%, 1% and 0.5% is enough to quench the discharges.

For the three SF_6 gas mixtures, the plateau curve is shifted toward high HV with increasing the fraction of SF_6. With higher fraction of SF_6 which quenches the streamer due to its high electron affinity, we need to apply higher HV to operate the RPC.

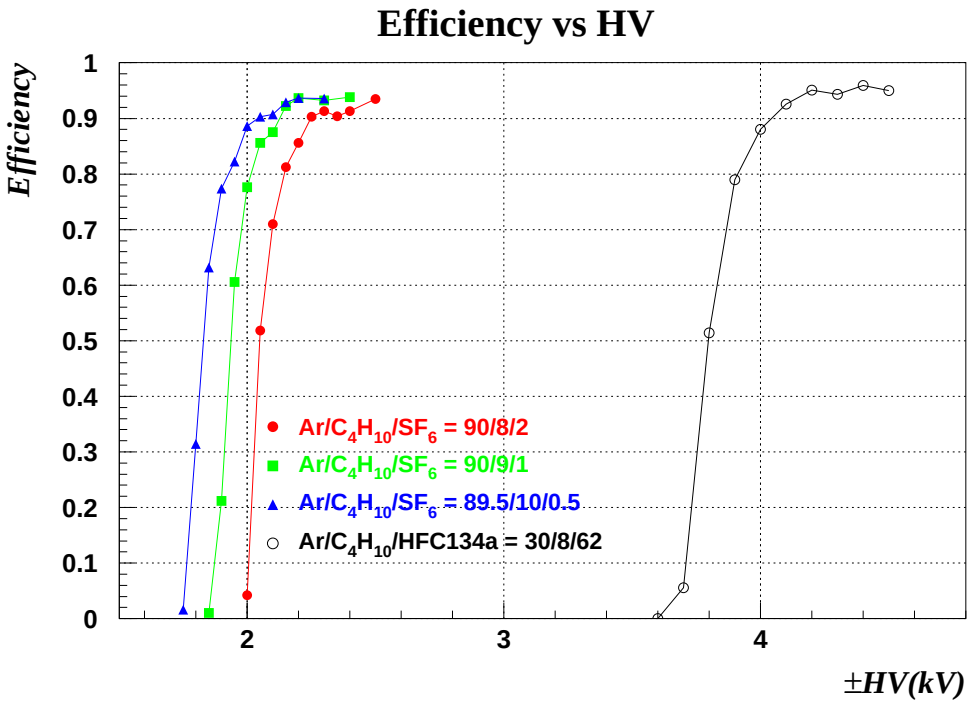

Figure 6.4: Efficiency curves for SF_6 gas mixtures and HFC134a mixture for reference.

• Dark current and Single count rate

Figure 6.5 shows the dark current versus HV for each gas mixture. The curve for the SF_6 gas mixtures are characterized by a "fast rise" especially above the plateau HV while the curve for the HFC134a mixture shows linear rise. Since the slopes of the curves indicate the inverse of the resistivity, it is implied that the resistivity of the SF_6 gas mixtures gets small with increasing HV.

At the plateau HV of each gas mixture, the dark current is about 0.45 μA/m^2.

Figure 6.6 shows the single count rate versus HV for each gas mixture. Note that these values have been measured by using a discriminator with 500 nsec wide output pulse in order not to count after-pulses. The curves are characterized by a plateau following a "fast rise". For the SF_6 gas mixtures, the curve have narrower plateau range than that for the HFC134a gas mixture, and even in the plateau, the single count rates are gradually increasing. This implies that in the the RPC with the SF_6 gas mixtures the noises due to spontaneous discharges increases with HV.

At the plateau HV of each gas mixture, the single count rate is about 0.045 Hz/cm^2.

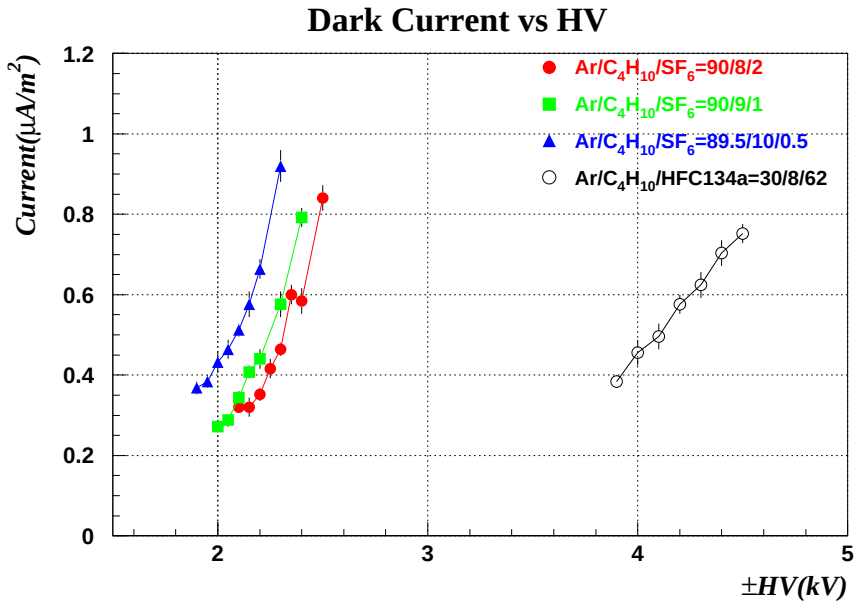

Figure 6.5: Dark current versus HV for SF_6 gas mixtures and HFC134a mixture for reference.

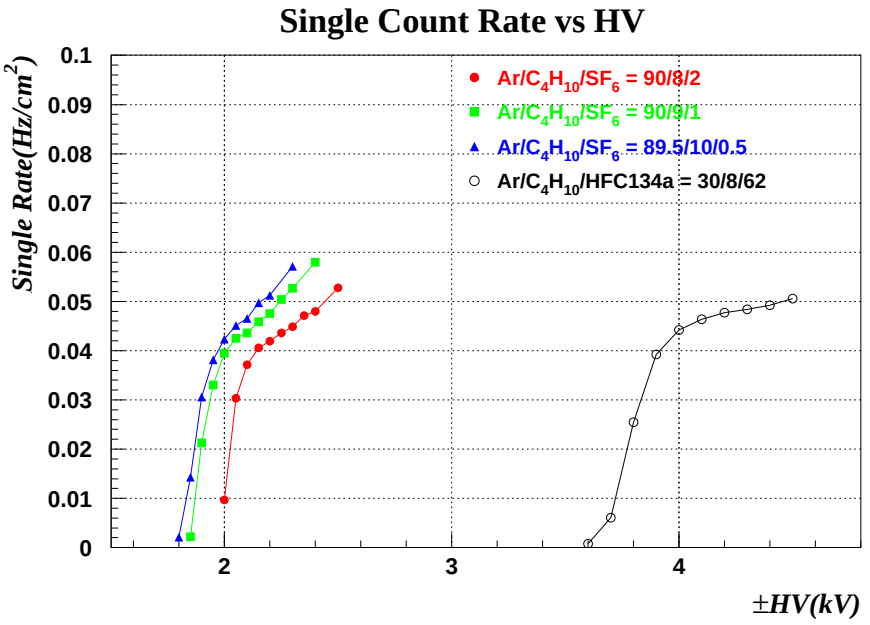

Figure 6.6: Single count rate versus HV for SF_6 gas mixtures and HFC134a mixture for reference.

• **Pulse shape and Charge**

Figure 6.7 shows the typical signal from the RPC at the plateau HV when using the gas mixture of Ar 90%/C_4H_{10} 9%/SF_6 1%. Other SF_6 gas mixtures show similar pulse shape to this figure. Typical of SF_6 gas mixtures are that the pulse hight is low such as 40 - 50 mV which is about half as high as that with HFC134a gas mixture shown in Figure 5.14 and that signals containing after-pulses appear frequently. The fraction of the signal containing after-pulses observed with an oscilloscope is about 60%. This fraction is considerably high compared with the fraction of 15% observed with HFC134a gas mixture. The sufficient quenching capability of SF_6 together with lower operating HV leads to lower gas multiplication and eventually lower pulse hight compared with the case for the HFC134a gas mixture. Higher fraction of the signal with after-pulses indicates that the SF_6 gas mixture makes more secondary discharges in spite of similar butane fraction. A possible explanation for the difference is that in the HFC134a gas mixture, HFC134a together with butane may absorb UV photons besides electron capture. Actually, it is known that many Freons absorb UV photons. Even if SF_6 is also capable of absorbing UV photons, since its fraction is rather small in the 1% range, secondary discharges would not be suppressed sufficiently.

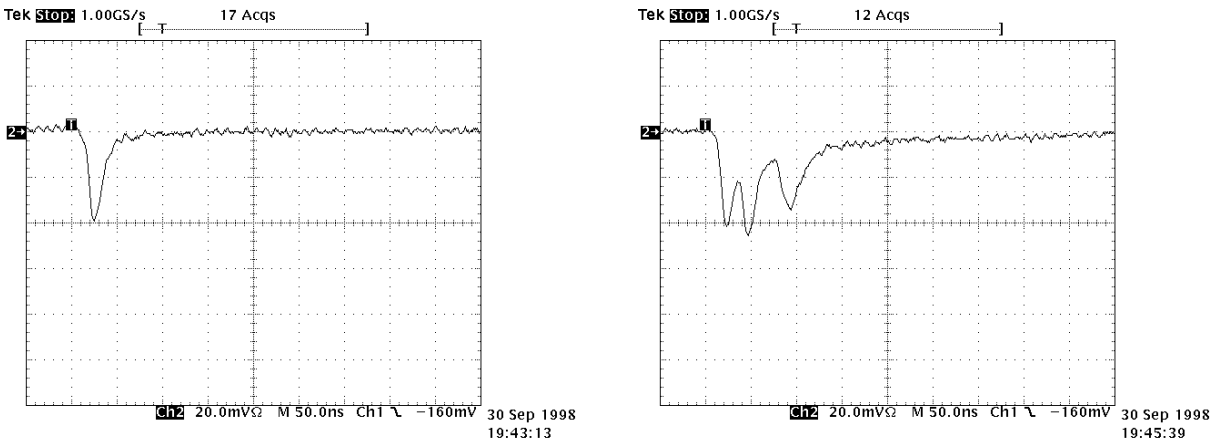

Figure 6.7: Typical signal from the RPC when using the gas mixture of Ar 90%/C_4H_{10} 9%/SF_6 1% at the plateau HV ±2.2 kV. The left figure shows typical single pulse signal, and the right shows the signal involving after-pulses. The fraction of the signal containing after-pulses was about 60%.

Figure 6.8 shows charge distributions at the plateau HVs. Comparing the charge distributions for the SF_6 gas mixtures with that for HFC134a gas mixture, it can be found that the distributions for the SF_6 gas mixtures have distinct second peaks while that for HFC134a has a major first peak and small second one. The first peak fractions in the SF_6 distributions are 40 - 50%, while that in the HFC134a distribution is 85%. These fractions are consistent with the after-pulses fractions observed with the oscilloscope. Also from the charge distributions, it can be verified that the SF_6 gas mixtures lead to more secondary discharges than the HFC134a. The central values of the first peaks in the SF_6 distributions vary from 35 to 50 pC with decreasing the SF_6 fraction. This is explained by the fact that lower fractions of SF_6 that is electro-negative gas lead to higher gas multiplication and more charges. In the HFC134a gas mixture, on the other hand, the central value of the first peak is 80 pC. The differences of the first peak charges correspond to the differences of the pulse hight.

Figure 6.9 and Figure 6.10 show the HV dependence of the charge distributions for Ar 90%/C_4H_{10} 9%/SF_6 1% and for Ar 30%/C_4H_10 8%/HFC134a 62% gas mixture, respectively. The clear difference between the two gas mixtures is seen especially at higher HV. While the distributions for the HFC134a gas mixture show almost same shape with major first peak and small second one, those for the SF_6 gas mixture show a rise of the second peaks with increasing HV. The fraction of the first peak in the SF_6 distribution decreases such as 40% at $\pm$ 2.20 kV (plateau HV) and 15% at $\pm$ 2.30 kV, and at $\pm$ 2.40 kV we can not find the first peak any longer. This indicates that for the SF_6 gas mixture the secondary discharges due to UV photons increase with HV, and this effect gets dominant especially at higher voltage than the plateau HV.

Figure 6.11 shows the mean charge versus HV for each gas mixture. Although the SF_6 gas mixtures make more secondary discharges, the mean charges, in general, show lower values due to much lower gas multiplication. The curves for the SF_6 gas mixtures are characterized by a "fast rise" compared with the HFC134a. This is because the secondary discharges increases with HV for the SF_6 gas mixtures as shown in Figure 6.9 in addition to a rise in the pulse hight with HV. The effect of increasing secondary discharges with HV can also explain the "fast rise" in the dark current for the SF_6 gas mixtures as shown in Figure 6.5.

The mean charges at the plateau HV are 50 - 60 pC for the SF_6 gas mixtures and 95 pC for the HFC134a gas mixture.

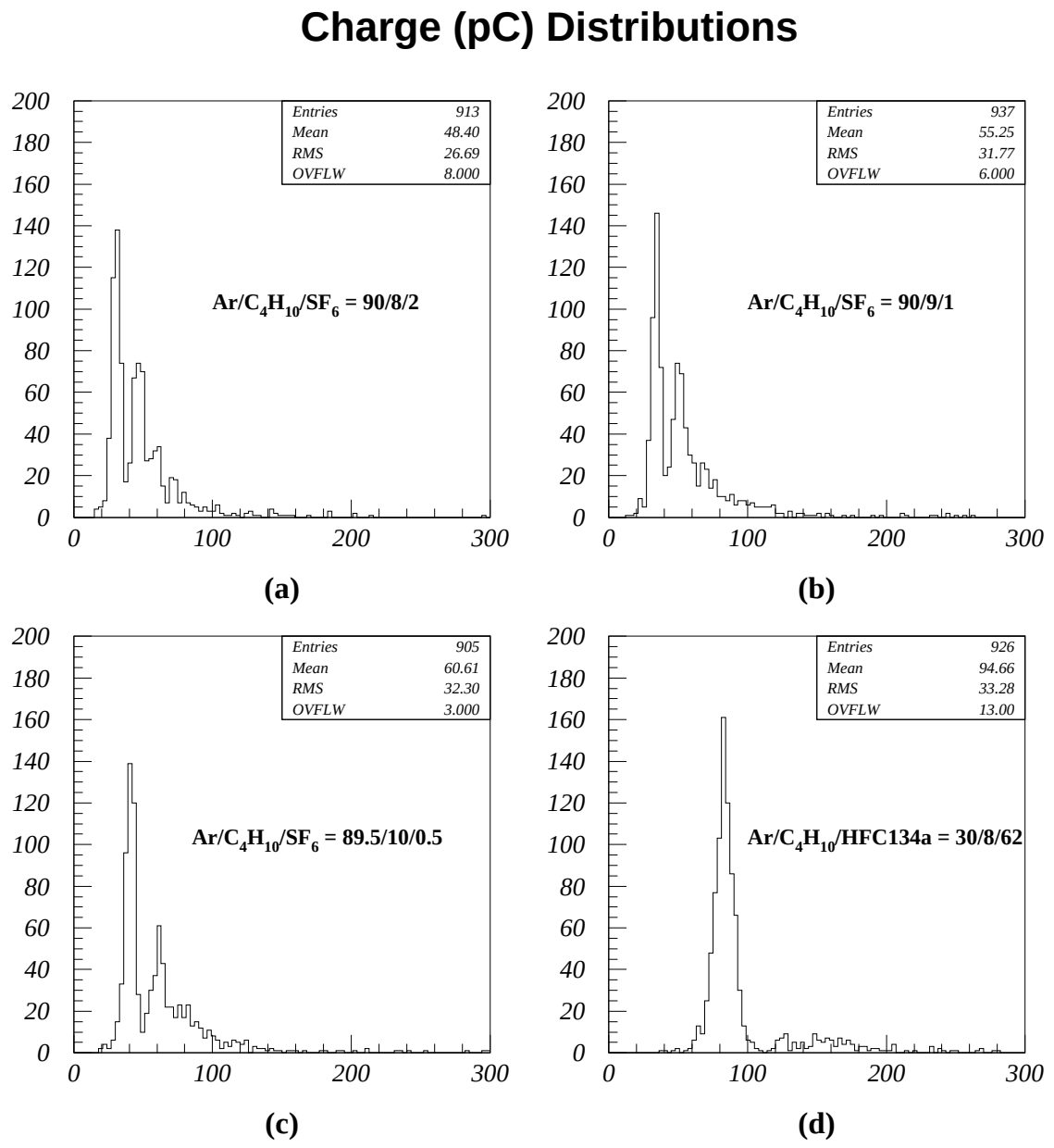

Figure 6.8: Charge distributions at the plateau HV; (a), (b), (c) for SF_6 gas mixtures and (d) for HFC134a mixture.

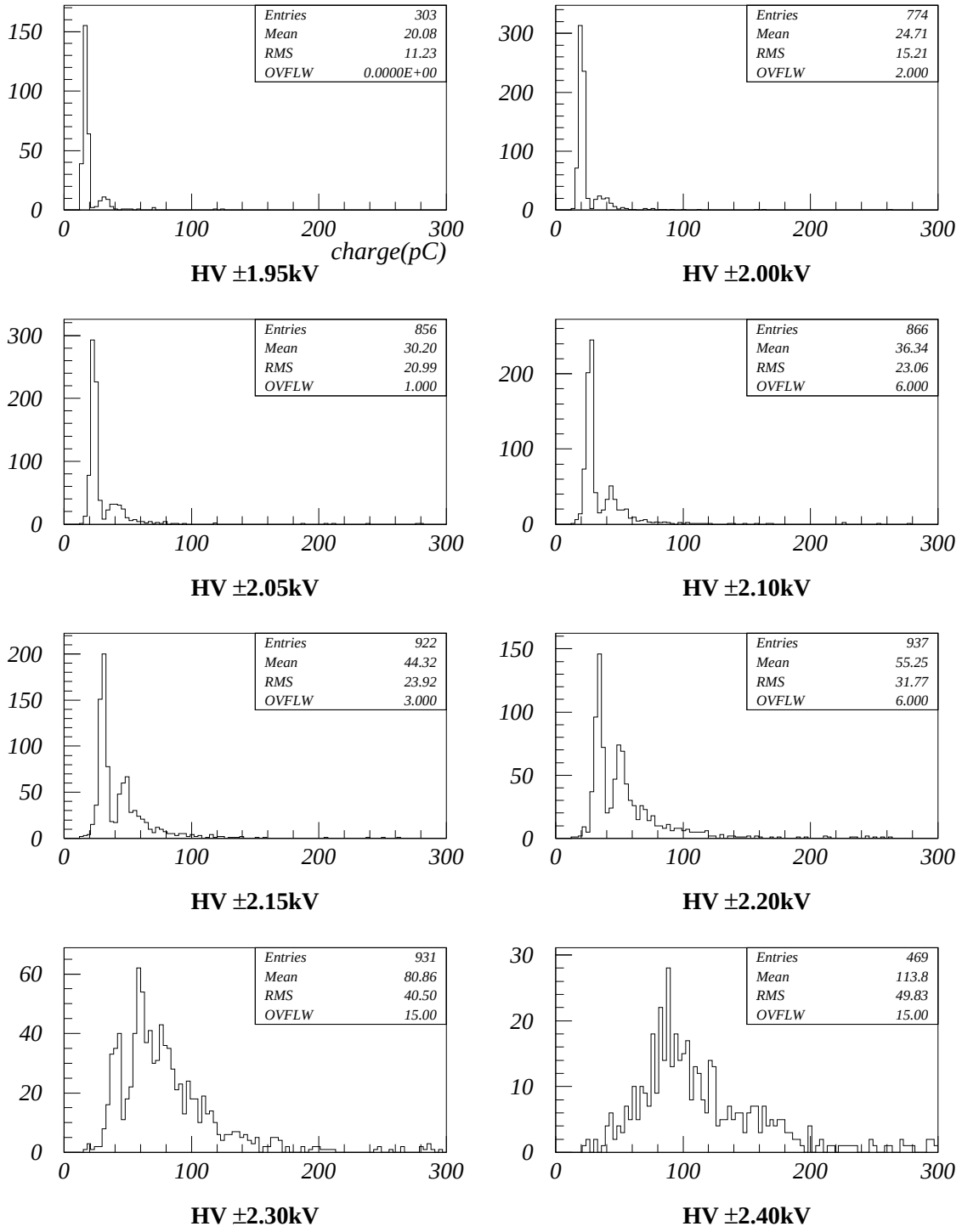

Figure 6.9: HV dependence of the charge distribution for Ar 90%/C_4H_{10} 9%/SF_6 1% gas mixture. The plateau HV is ± 2.20 kV.

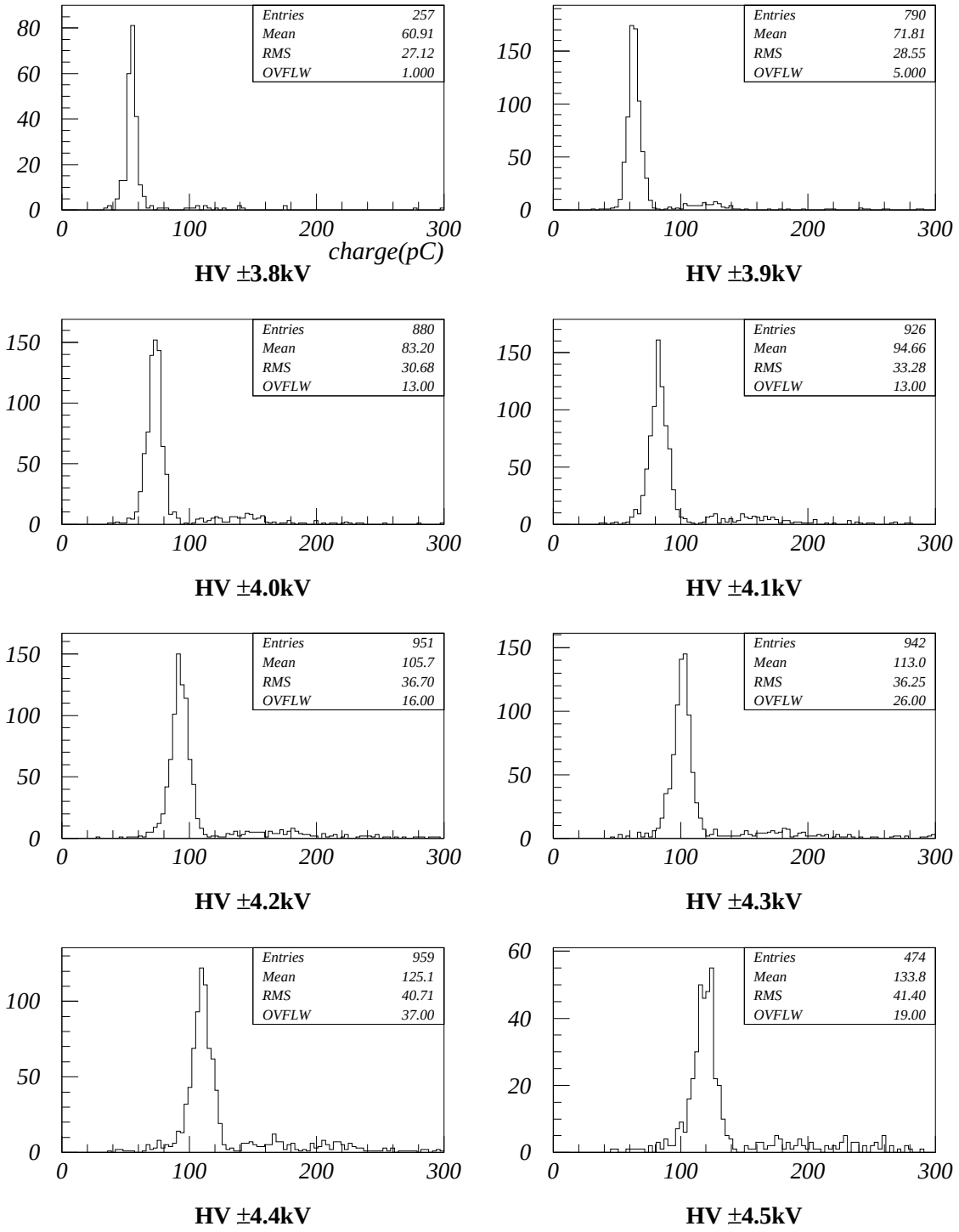

Figure 6.10: HV dependence of the charge distribution for Ar 30%/C_4H_{10} 8%/HFC134a 62% gas mixture. The plateau HV is ± 4.1 kV.

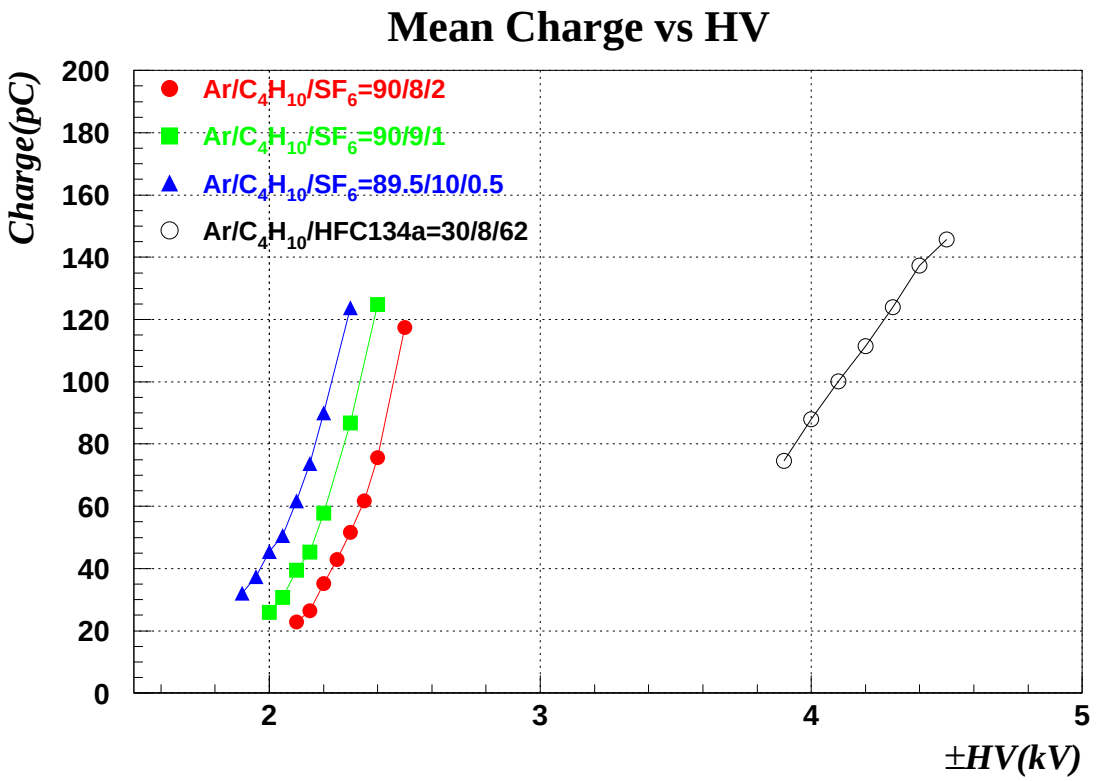

Figure 6.11: Mean charge versus HV for SF_6 gas mixtures and HFC134a mixture for reference.

• **Time resolution**

Figure 6.13 shows the distributions of time difference between hits in two RPCs at the plateau HV; (a), (b), (c) for SF_6 gas mixtures and (d) for HFC134a mixture. It can be found that the distributions for the SF_6 gas mixtures have slightly wider tails than the HFC134a mixture. Figure 6.12 shows the time resolutions derived from the standard deviation of a Gaussian fit of the distributions, as a function of HV. The time resolution improves with increasing HV for each gas mixture. For the HFC134a gas mixture the time resolution is saturated at high HVs, on the other hand, for the SF_6 gas mixtures they still improves at high HVs. However, the time resolutions for the SF_6 gas mixtures are slightly worse than that for the HFC134a mixture. At the plateau HVs, 3.5 nsec time resolutions are obtained for the SF_6 gas mixture while 3 nsec is obtained for the HFC134a mixture. Slightly worse time resolutions for the SF_6 gas mixture are considered due to lower operating HV.

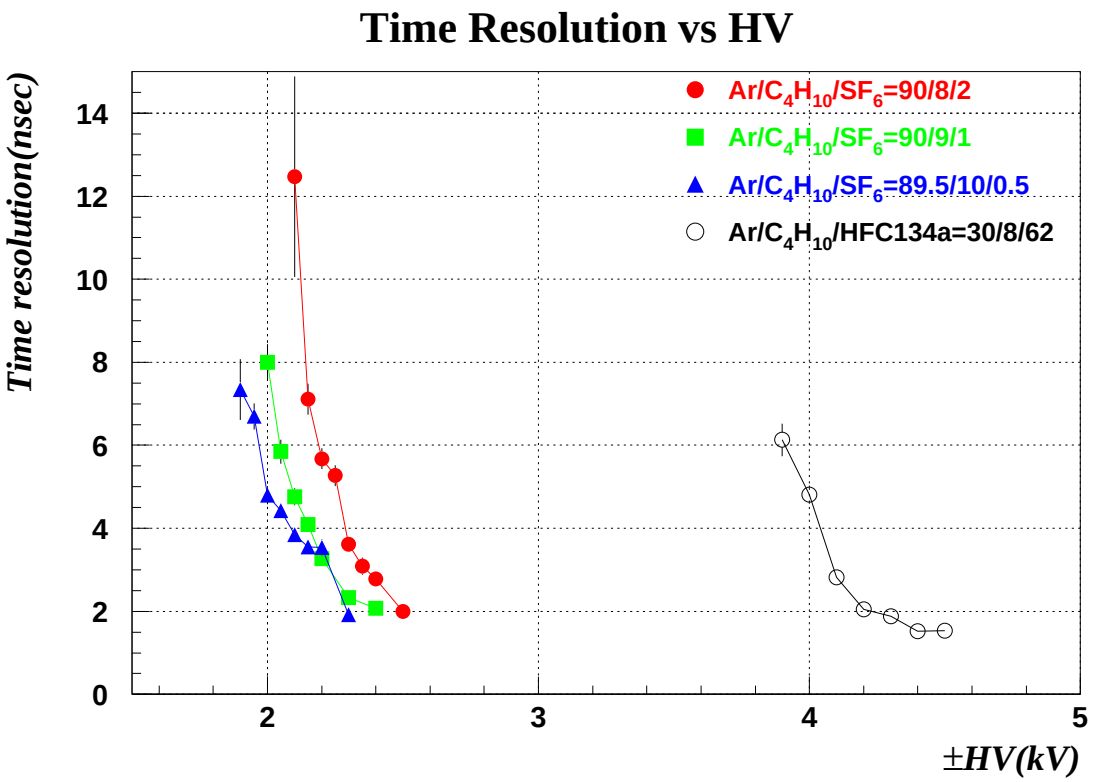

Figure 6.12: Time resolution versus HV for SF_6 gas mixtures and HFC134a mixture for reference.

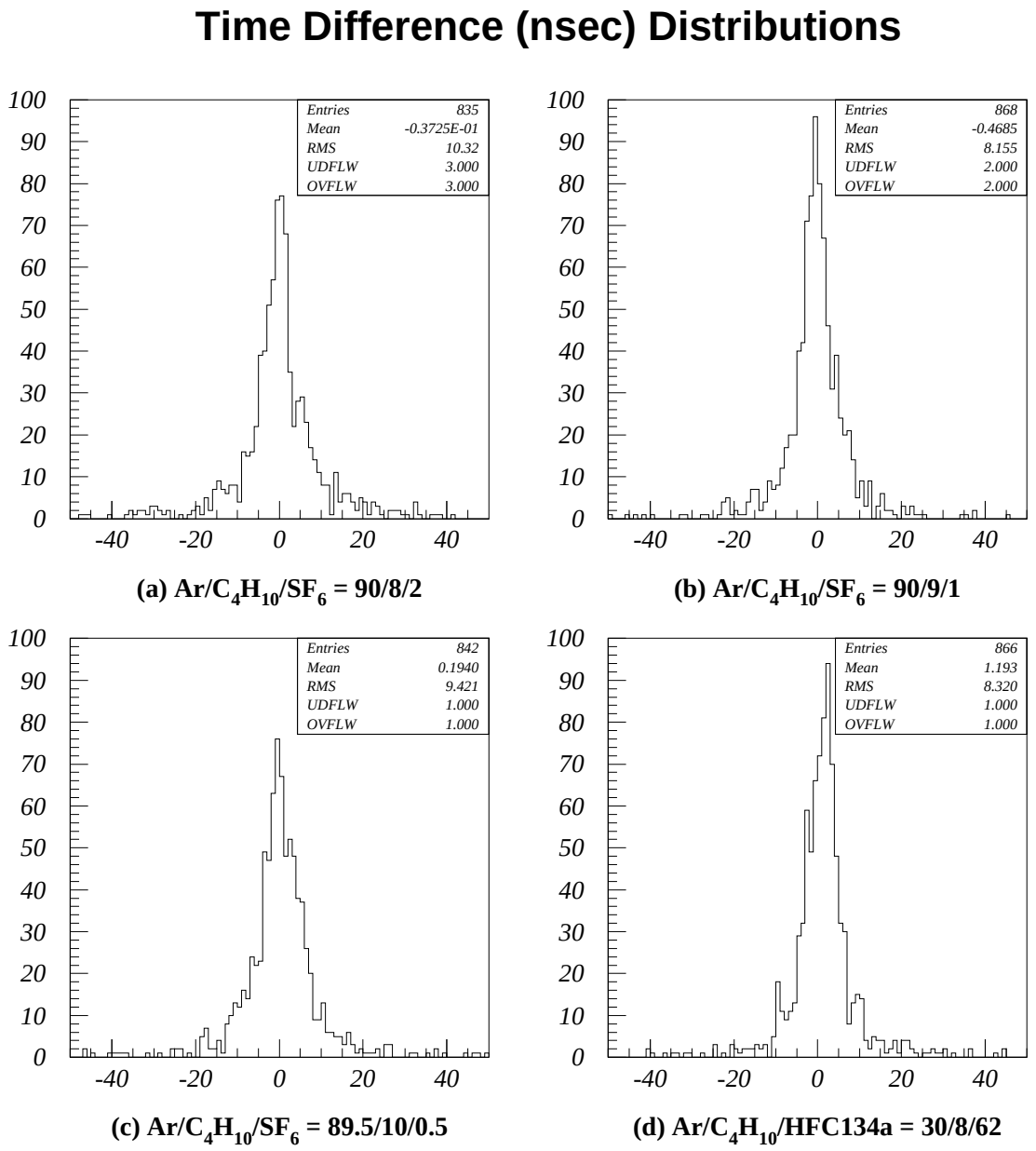

Figure 6.13: Distributions of time difference between hits in two RPCs at the plateau HV; (a), (b), (c) for SF_6 gas mixtures and (d) for HFC134a mixture.

• **Strip multiplicity and Charge spread**

Figure 6.14 shows the multiple hit distributions at the plateau HV for each gas mixture, which have been obtained by using strips with 3 mm wide and 2 mm in gap spacing for the signal pickup, thus one strip corresponds to 5 mm. Note that these values have been obtained with 30 mV threshold of a discriminator both for the HFC134a and for SF_6 gas mixtures. This figure shows that the mean values of the multiple hit for the SF_6 gas mixture are 2.2 - 2.5 while that for the HFC134a is 3.0. This indicates that the charge spread for the SF_6 gas mixture is smaller than that for the HFC134a. However, this is not the case. We have to take into account the difference of the pulse hight. Since the pulse heights for the SF_6 gas mixtures are lower than that for the HFC134a, with fixed threshold, the multiple hits for the SF_6 gas mixtures could get small. For the SF_6 gas mixtures, the mean values of the multiple hit become high with increasing the fraction of SF_6, which is consistent with the differences of the pulse heights among the SF_6 gas mixtures mentioned above.

In order to investigate an intrinsic charge spread for each gas mixture, we have used charge information induced on each strips which is independent of the threshold. Figure 6.15 shows the charge sum induced on each of 18 strips over all collected events. From a standard deviation of a Gaussian fit of this distribution $\sigma_{meas.}$, an intrinsic charge spread is derived. This distribution contains an error from 1cm wide "finger" scintillation counter illustrated in Figure 5.5. Since the scintillation has 1 cm width and is located apart from the strips, hit positions in the RPC are dispersed. The hit position is estimated by a charge weighted mean value of the strip position such as $(\sum_{i=1}^{18} n_i Q_i)/Q_{total}$, where n and Q denote a strip position and a charge, respectively. The distributions of the hit position for each gas mixture are shown in Figure 6.16. The standard deviation of a Gaussian fit of this distribution $\sigma_{hit\_pos.}$ gives the error due to 1cm wide scintillation counter. From $\sigma_{meas.}$ and $\sigma_{hit\_pos.}$, we have an intrinsic charge spread $\sigma_{intr.}$ by ${\sigma_{meas.}}^2 = {\sigma_{hit\_pos.}}^2 + {\sigma_{intr.}}^2$. The intrinsic charge spread obtained for each gas mixture is listed in Table 6.5. The charge spread for the SF_6 gas mixtures are 5.7 - 5.9 mm that are slightly larger than 5.2 mm obtained for the HFC134a mixture. This is also explained by the fact that the secondary discharges occur more for the SF_6 gas mixture, which is verified from the measurement of pulse shape and charge distribution. In the SF_6 gas mixture, UV photons can travel

without being absorbed and induce secondary discharges apart from the position of the primary one. As a result, the charge spread for the SF_6 gas mixtures become larger than that for the HFC134a mixture. This charge spread difference, however, is not so critical because spatial resolution of 5 cm is sufficient for our particular application as described in chapter 3.

Table 6.5: Charge spread.

gas mixture	$\sigma_{meas.}$	$\sigma_{hit\_pos.}$	$\sigma_{intr.}$
Ar 90%/C_4H_{10} 8%/SF_6 2%	1.58	1.05	1.18 (5.90 mm)
Ar 90%/C_4H_{10} 9%/SF_6 1%	1.56	1.08	1.13 (5.65 mm)
Ar 89.5%/C_4H_{10} 10%/SF_6 0.5%	1.58	1.07	1.17 (5.85 mm)
Ar 30%/C_4H_{10} 8%/HFC134a 62%	1.50	1.09	1.05 (5.15 mm)

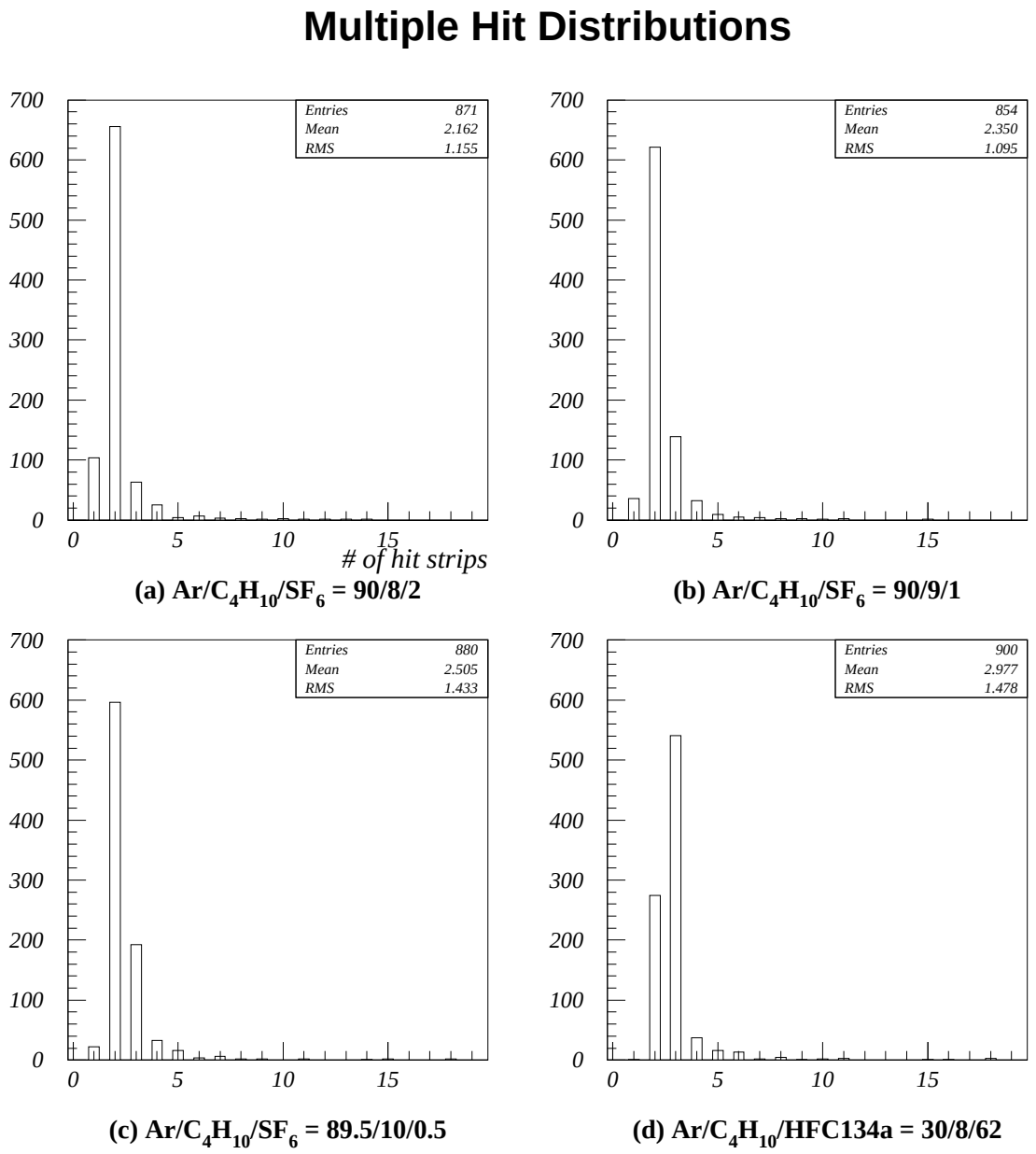

Figure 6.14: Multiple hit distributions at the plateau HV; (a), (b), (c) for SF_6 gas mixtures and (d) for HFC134a mixture.

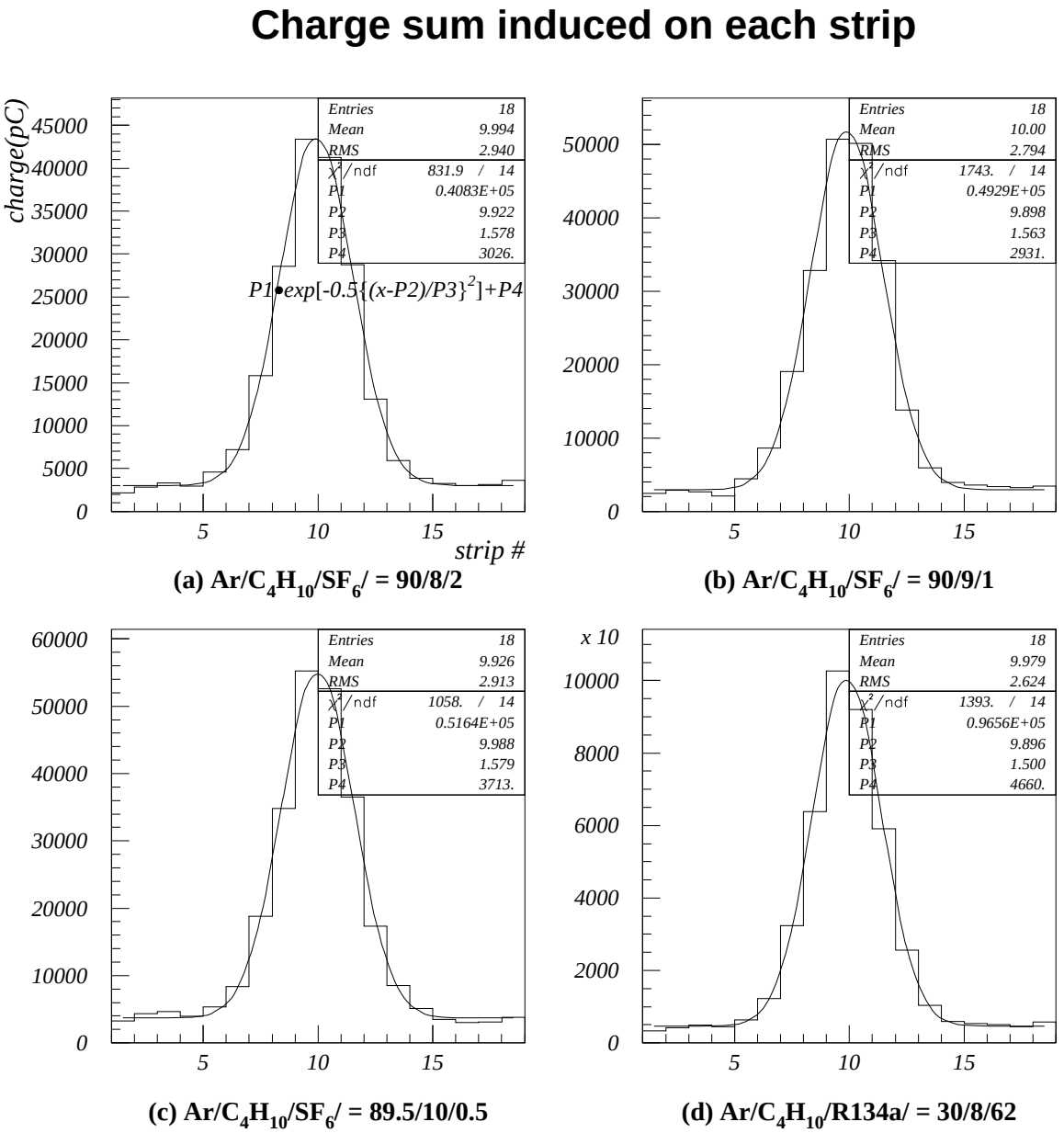

Figure 6.15: The sum of the charge induced on each strip at the plateau HV; (a), (b), (c) for SF_6 gas mixtures and (d) for HFC134a mixture.

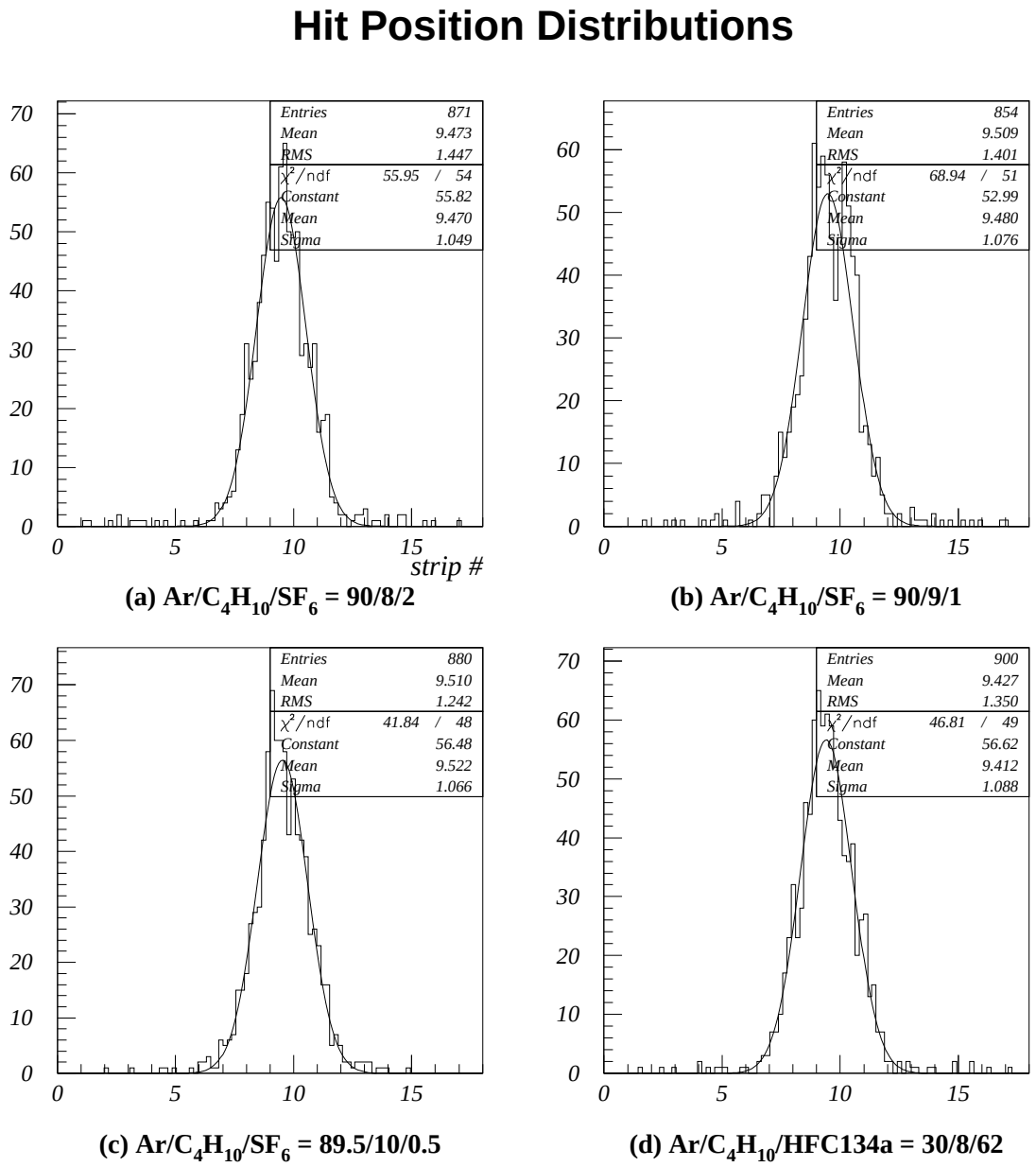

Figure 6.16: Hit position distributions at the plateau HV; (a), (b), (c) for SF_6 gas mixtures and (d) for HFC134a mixture.

6.5 Conclusions

We have tested O_2 and SF_6 as the alternative gas to HFC134a. We could not obtain more than 90% efficiency for O_2 gas mixtures.

The results obtained for the gas mixture of Ar 90%/C_4H_{10} 9%/SF_6 1% at the plateau HV are summarized in Table 6.6. The data obtained for the gas mixture of Ar 30%/C_4H_{10} 8%/HFC134a 62% are also listed in the table for comparison. The differences between the RPC performances for the two gas mixtures can be explained by the high capability of electron capture and the insufficient capability of absorbing UV photons of the SF_6 gas mixture. Since SF_6 has high electron affinity, even a little fraction of SF_6 such as 1% is enough to quench the discharges. This enables us to operate RPCs at much lower HV than the HFC134a case. And this lower operating HV causes slightly worse time resolution. The high quenching capability also reduces the efficiency slightly, and moreover, it lowers the signal pulse hight due to lower gas multiplication. On the other hand, the insufficient capability of absorbing UV photons of the SF_6 gas mixture causes more secondary discharges, which results in the signals containing more after-pulses and slightly wider charge spread. Although the signals for the SF_6 gas mixture contains more after-pulses, since the pulse hight is lower, the mean charge gets lower than the HFC134a case.

The RPC performance with the SF_6 gas mixture is also represented by "fast rise" especially after the plateau HV as shown in the plots of the dark current (Figure 6.5), the single count rate (Figure 6.6), and the charge (Figure 6.11).

Possibility as the gas for BELLE KLM detector

Now we discuss the possibility to use the SF_6 gas mixture as the gas for BELLE KLM detector.

The detection efficiency of 92% is enough because, combined the two RPC layers into a superlayer (see Figure 3.5), more than 99% efficiency is attainable. Due to the low pulse height, it may be necessary to use an amplifier or to lower the threshold. Even if we use an amplifier, the gain of 2 is sufficient so that complicated front end electronics is not necessary. Concerning the time resolution, it is desirable to have a few nsec time resolution for cosmic ray rejection, thus 3.5 nsec time resolution is sufficient. Since the

required spatial resolution for the KLM is 5 cm (see section 3.1), 5.7 mm spatial resolution is sufficient.

A question is whether the RPC with the SF_6 gas mixture can endure a longterm operation. Considering that a plateau range in general becomes narrow with a degradation of a detector, the SF_6 gas mixture with a narrow plateau range does not seem to be suitable for a longterm operation. However, far lower operation HV must be a great advantage.

In any case, the longterm stability for the SF_6 gas mixture has to be verified before used as the gas for BELLE KLM.

Table 6.6: Comparison of the RPC performance between using SF_6 and using HFC134a gas mixture at the plateau HV.

gas	Ar 90%/C_4H_{10} 9%/SF_6 1%	Ar 30%/C_4H_{10} 8%/HFC134a 62%
GWP[a]	249	806
efficiency	92%	94%
plateau HV	± 2.2 kV	± 4.1 kV
signal		
pulse height	40 mV	100 mV
after-pulse	60%	10%
mean charge	60 pC	100 pC
dark current	0.45 μA/m^2	0.5 μA/m^2
single count rate	0.047 Hz/cm^2	0.047 Hz/cm^2
time resolution	3.5 nsec	3.0 nsec
spatial resolution (charge spread)	5.7 mm	5.2 mm

[a]A unit is the GWP of 100% CO_2 gas mixture.

Chapter 7

Summary

We employ the glass RPCs for the KLM detector at BELLE experiment. The RPC is a gaseous detector and a selection of nonflammable gas mixture is an important issue for safety or for avoiding complicated procedures that are required for flammable gases. It is not better to use Freon which we have been using for the RPC, since it has a high global warming potential. Then we have performed a study of nonflammable and freonless gas mixture for the glass RPCs.

We have tested RPCs with nonflammable gas mixtures containing less butane (less than 12%) that is expected to prevent the secondary discharges by absorbing ultraviolet photons, and compared their performances with those for flammable ones.

We have obtained following results:

- More than 90% efficiency was obtained for each gas mixture
- For the dark current, the single count rate and the time resolution, there were no significant differences for each gas mixture
- Nonflammable gas mixture is likely to make slightly more secondary discharges
- No significant differences were found for the charge spread

A nonflammable gas mixture indeed makes slightly more secondary discharges compared with a flammable one, however, the secondary discharges do not occur apart from the position of the primary discharge, and thus there are no significant differences for

the charge spread. In addition to these comparable results, considering the advantages in using nonflammable gas mixture:

- To be nonflammable is good thing in itself for safety or for avoiding complicated procedures required for a flammable gas mixture

we conclude that nonflammable gas mixture is useful enough, and now use the nonflammable gas mixture of argon/butane/HFC134a = 32%/8%/60% for the RPCs for the KLM.

We also have tested two kinds of gas mixtures without containing HFC134a from the point of view of global warming. One is an oxygen (O_2) gas mixtures which do not have an influence on global warming, and the other is a sulfur hexafluoride (SF_6) gas mixture with a few percent SF_6 concentration so as to have less global warming potential (GWP) than the HFC134a gas mixture.

We have obtained following results (the results for the SF_6 gas mixture are summarized in Table 6.6):

- More than 90% efficiency was not obtained for the O_2 gas mixtures

- More than 90% efficiency was obtained for the SF_6 gas mixtures (argon/butane/SF_6 = 90/8/2, 90/9/1, and 89.5/10/0.5)
- The dark current, the single count rate, the time resolution, and the spatial resolution for the the SF_6 gas mixtures were comparable to the HFC134a gas mixture (argon/butane/HFC134a = 32/8/60)
- The RPC with the SF_6 gas mixtures can operate at about ± 2.2 kV which is about half of the HFC134a case (± 4.1 kV)
- The signal for the SF_6 gas mixtures is characterized by low pulse height and many after-pulses compared with the HFC134a case.
- The RPC performance with the SF_6 gas mixture is characterized by a "fast rise"of the dark current, the single count rate, and the charge after the plateau HV.

When using SF_6 gas mixture, we can operate RPC at much lower high voltage (HV) with comparable performances to the HFC134a gas mixture. However, the "fast rise" might affect an operation stability of the detector. Although much lower operation HV is indeed a great advantage, it would not be better to use SF_6 gas mixture without being verified the longterm stability. We need to test the longterm stability of the SF_6 gas mixture.

Bibliography

[1] T.D.Lee and C.N.Yang, Phys.Rev. **104** (1956) 254.

[2] C.S.Wu, E.Ambler, R.W.Hayward, D.D.Hoppes and R.P.Hudson, "Experimantal test of parity conservation", Phys.Rev. **105** (1957) 1413.

[3] J.H.Christenson, J.W.Cronin, V.L.Fitch and R.Turlay, "Evidence for the 2π decay of the K_2^0 meson", Phys.Rev.Lett. **13** (1964) 138.

[4] Particle Data Group, "Review of Particle Physics", Eur.Phys.J. **C 3**(1998) 1.

[5] Super-Kamiokande Collaboration, Phys.Rev.Lett. **81** (1998) 1562.

[6] M.Kobayashi and T.Maskawa, Prog.Theor.Phys. **42** (1973) 652.

[7] L.Wolfenstein, Phys.Rev.Lett. **51** (1983) 1945.

[8] T.E.Browder, K.Honscheid, UH 511-816-95, OHSTPY-HEP-E-95-010 (1995).

[9] A.B.Carter and A.I.Sanda, Phys.Rev.Lett. **45** (1980) 952; Phys.Rev.D **23** (1981) 1567.
I.I.Bigi and A.I.Sanda, Nucl.Phys. **B193** (1981) 85; Nucl.Phys. **B281** (1987) 41.

[10] M.Gronau and D.London, Phys.Rev.Lett. **65** (1990) 3381;
H.J.Lipkin, Y.Nir, H.R.Quinn and A.E.Snyder, Phys.Rev. **D44** (1991) 1454.

[11] A.B.Carter and A.I.Sanda, Phys.Rev. **23** (1981) 1567;
M.Gronau and D.London, Phys.Lett. **253B** (1991) 483;
I.Dunietz, CERN-TH-6161/91 (1991);
M.Gronau and D.Wyler, TECHNION-PH-91-14 (1991).

[12] KEKB B-Factory Design Report, KEK Report 95-7, August 1995.

[13] BELLE Collaboration, BELLE Technical Design Report, KEK Report 95-1, April 1995.

[14] BELLE Collaboration, BELLE Progress Report, KEK Progress Report 96-1, March 1996.
BELLE Collaboration, BELLE Progress Report, KEK Progress Report 97-1, March 1997.

[15] BELLE SVD group, Technical Design Report of BELLE SVD, March 1998.

[16] V.M.Aulchnko. *et al.*, "Study of characteristics of the BELLE CsI calorimeter prototype with a BINP tagged photon beam", Nucl.Instr.Meth.**A410** (1998) 179-194.

[17] K.Neichi *et al.* "The Readout-strip width in KLM detector", KEK BELLE Note #109.

[18] M.Yamaga, Master's Thesis, Tohoku University (1998).

[19] K.Abe *et al.* "Cosmic-ray Test of the Installed Endcap RPC Modules in BELLE Detector", TOHOKU-HEP-NOTE-99-01, January, 1999.

[20] R.Santonico *et al.*, Nucl. Instr. and Meth. **A187** (1981) 377.
R.Cardarelli *et al.*, Nucl. Instr. and Meth. **263** (1988) 20.

[21] J.W.Keuffel, Rev. Sci. Instr. **20** (1949) 202.

[22] V.V.Parkhomchuck *et al.*, Nucl. Instr. and Meth. **93** (1971) 269.
Yu.N.Pestov, Nucl. Instr. and Meth. **196** (1982) 45.

[23] M.Abbrescia *et al.*, Nucl. Instr. and Meth. **A336** (1993) 322.

[24] L.Antoniazzi *et al.*, Nucl. Instr. and Meth. **A315** (1992) 92.

[25] O.Adriani *et al.*, Nucl. Instr. and Meth. **A300** (1991) 493.

[26] F.Sauli, "Principles of Operation of Multiwire Proportional and Drift Chambers", CERN Report 77-09 (1977).

[27] R.Santonico, "RPC: Status and Perspectives", International Workshop on RPCs and related detectors, 1993.

[28] I.Crotty *et al.*, Nucl. Instr. and Meth. **A337** (1994) 370.
H.Czyrkowski *et al.*, Nucl. Instr. and Meth. **A419** (1998) 490.

[29] M.Ichinose, Master's Thesis, Tohoku University (1997).

[30] Y.Hoshi *et al.* "Nonflammable gas mixture for RPC", KEK BELLE Note #185.

[31] M.Sanpei *et al.* "Performance of Resistive Plate Counter with Non-Ozone Depletion Freon", IEEE Trans.Nucl.Sci. Vol.44, No.3 (1997) 752.

[32] B. Lewis and G. Elbe, "Combustion, Flames and Explosions of Gases", Cambridge University Press (1938).

[33] M.Ishikawa, Master's Thesis, Tohoku University (1996).

[34] M.Abbrescia *et al.*, "Resistive Plate Chamber performances at cosmic-ray fluxes", Nucl.Instr.and Meth. **A 359** (1995) 603.

[35] I.S.Buchel'nikova, Soviet Phys. JETP **35(8)** (1959) 783.